Co-translational processing and membrane insertion of proteins in bacteria

Dissertation

for the award of the degree

“Doctor rerum naturalium”

of the Georg-August-Universität Göttingen

within the doctoral program

GGNB Biomolecules: Structure – Function – Dynamics

of the Georg-August University School of Science (GAUSS)

submitted by

Lena A. K. Bögeholz

from Bielefeld, Germany

Göttingen 2022

Thesis Committee

Prof. Dr. Marina Rodnina
Department of Physical Biochemistry
Max Planck Institute for Multidisciplinary Sciences, Göttingen Germany

Prof. Dr. Kai Tittmann
Department of Molecular Enzymology
Georg-August-University Göttingen, Göttingen Germany

Dr. Alexander Stein
Membrane Protein Biochemistry
Max Planck Institute for Multidisciplinary Sciences, Göttingen Germany

Members of the Examination Board

Referee: Prof. Dr. Marina Rodnina
Department of Physical Biochemistry
Max Planck Institute for Multidisciplinary Sciences, Göttingen Germany

2nd Referee: Prof. Dr. Kai Tittmann
Department of Molecular Enzymology
Georg-August-University Göttingen, Göttingen Germany

Further members of the Examination Board

Dr. Alexander Stein
Membrane Protein Biochemistry
Max Planck Institute for Multidisciplinary Sciences, Göttingen Germany

Prof. Dr. Wolfgang Wintermeyer
Ribosome Dynamics
Max Planck Institute for Multidisciplinary Sciences, Göttingen Germany

Dr. Alex Faesen
Biochemistry of Signal Dynamics
Max Planck Institute for Multidisciplinary Sciences, Göttingen Germany

Prof. Dr. Hauke Hillen
Department of Cellular Biochemistry
University Medical Center Göttingen, Göttingen Germany

Date of oral examination: September 13th, 2022.

Affidavit

I hereby declare that the presented dissertation entitled “Co-translational processing and membrane insertion of proteins in bacteria” has been written independently and with no other sources and aids than quoted.

Göttingen, 29.07.2020

Lena Bögeholz

Related publications:

Bögeholz, L. A. K., Mercier, E., Wintermeyer, W., and Rodnina, M. V. (2021). Kinetic control of nascent protein biogenesis by peptide deformylase. Sci. Rep. *11*, 24457.

Mercier, E., Wang, X., **Bögeholz, L. A. K.**, Wintermeyer, W., and Rodnina, M. V. (2022). Cotranslational Biogenesis of Membrane Proteins in Bacteria. Front. Mol. Biosci. *9*, 871121.

Zaghouani, M., **Bögeholz, L. A. K.**, Mercier, E., Wintermeyer, W., and Roche, S. P. (2019). Total synthesis of (+/-)-fumimycin and analogues for biological evaluation as peptide deformylase inhibitors. Tetrahedron. *75*, 3216-3230.

Table of contents

Abstract

Protein biogenesis entails the synthesis of polypeptides on the ribosome, their co- and post-translational maturation, folding, and, in the case of membrane proteins, insertion into the lipid bilayer. Bacterial proteins are synthesized with a formyl group on the N-terminus and the first processing step of the nascent chain is the removal of this formyl group by peptide deformylase (PDF). The majority of new proteins undergoes deformylation which is essential in bacteria and a requirement for the subsequent processing step. Here, we analyzed the kinetic mechanism of deformylation using ribosome nascent chain complexes (RNCs) and actively translating ribosomes as substrates. Binding and dissociation of PDF and RNC occur rapidly, allowing for efficient scanning of formylated substrates in the cell. Rapid hydrolysis of the formyl group stops scanning and is followed by the rate-limiting conformational rearrangement of the nascent chain. Therefore, release of the RNC by PDF is slow, which limits further N-terminal processing and may affect folding of nascent proteins. PDF is a promising drug target for antimicrobials, which prompted us to test whether deformylation can be prevented by novel analogues of the natural PDF inhibitor fumimycin, however, the analogues had only small effects.

During the biogenesis of inner membrane proteins, deformylation is inhibited by the signal recognition particle which ensures that the transmembrane helices (TMs) of the nascent membrane protein are co-translationally inserted into the lipid bilayer where the protein begins to fold. Insertion occurs with the help of the SecYEG translocon in bacteria but how TMs move into the membrane is not well understood. To monitor the co-translational insertion of TM1 and TM2 of the model protein EmrD, we performed real-time FRET experiments with fluorescence labels on the nascent chain and the translocon. We show that TM1 and TM2 are in close proximity to each other while partitioning into the membrane and that the two TMS remain close to the translocon afterwards. While the N-terminus resides in a relatively stable position, TM2 is more dynamic and undergoes conformational rearrangements that indicate the onset of protein folding before EmrD has been fully synthesized.

1 Introduction

1.1 Protein synthesis

Proteins are biological macromolecules that fulfil a variety of functions in a cell. They can be found in all cellular compartments: in solution, associated to or embedded in membranes. It is crucial for most cells to synthesize new proteins from amino acids to sustain viability or react to changes in the environment. The correct amino acid sequence for each protein is encoded in the DNA, which is transcribed into messenger RNA (mRNA) to be used as a template for protein synthesis. In a process called translation, the ribosome decodes the mRNA and produces a new protein. During this process, codons are read by transfer RNAs (tRNAs), which recognize the codon triplets and carry the encoded amino acid to the ribosome. Each time the new amino acid is incorporated into the nascent peptide chain, the ribosome moves by one codon until the whole protein is synthesized.

1.1.1 The ribosome

The ribosome is a large ribonucleoprotein complex that is responsible for the synthesis of new proteins and that is universally conserved in all domains of life. Eukaryotic and bacterial ribosomes share a conserved structural core that conveys the main functionality, but the two types of ribosomes contain additional proteins and rRNA extensions (Melnikov et al., 2012). The bacterial 70S ribosome (Figure 1A) is formed by the small 30S subunit consisting of 21 proteins and the 16S ribosomal RNA (rRNA) while the large 50S subunit comprises 31 proteins and the 23S and 5S rRNAs. The small ribosomal subunit binds the mRNA that threads through a 30S tunnel to the decoding center at the interface between the two ribosomal subunits (Culver, 2001; Demeshkina et al., 2013). The interface between the ribosomal subunits forms the three binding sites for tRNAs: aminoacyl-tRNA (aa-tRNA) is accommodated in the A site when it enters the ribosome; the P site harbors the peptidyl-tRNA that carries the nascent peptide chain; and the E site provides the exit for tRNAs from the ribosome. Parts of the rRNA of the large ribosomal subunit form the peptidyl transferase center (PTC) which assists the formation of the peptide bond when a new amino acid is added to the nascent chain by transferring the polypeptide from the P-site tRNA to the aa-tRNA in the A site (Beringer and Rodnina, 2007). The PTC leads the nascent peptide into the roughly 100 Å long peptide exit tunnel, which guides the new protein out of the ribosome and has a width between 10 and 20 Å (Figure 1B) (Liutkute et al., 2020b). At about 30 Å distance from the PTC, the universal ribosomal proteins uL4 and uL22 form a constriction site with a diameter of about 8 Å (Dao Duc et al., 2019). The tunnel ends in the so-called vestibule which is a wider region formed by proteins uL23 and uL24. About

30 to 40 amino acids, depending on secondary structural elements, are required to span the entire peptide exit tunnel (Liutkute et al., 2020b).

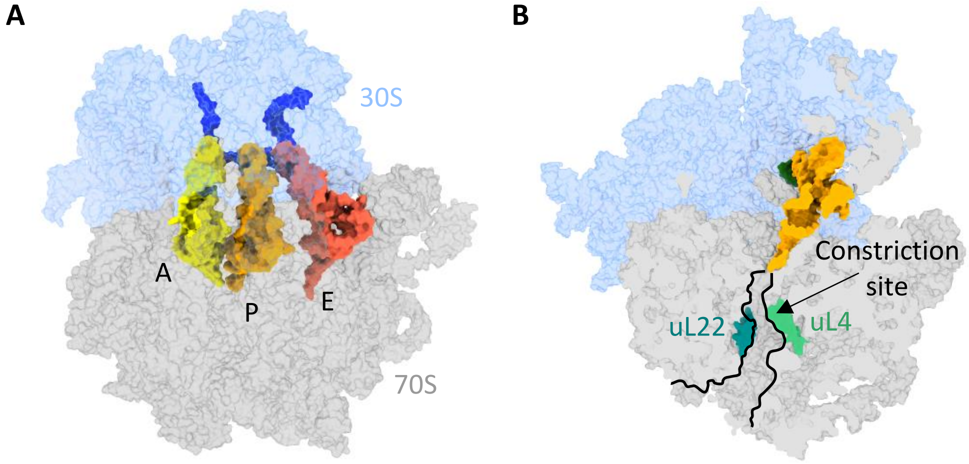

Figure 1. The ribosome.

(**A**) Structure of the 70S ribosome from *Thermus thermophilus* (PDB: 4V6F). tRNAs in the A site (yellow, truncated), P site (orange) and E site (red) are bound to mRNA (dark blue) and located at the interface between the 50S (gray) and 30S subunit (light blue).

(**B**) The peptide exit tunnel is outlined (black) on a 70S ribosome from *E. coli* (PDB: 7OT5). Ribosomal proteins uL22 (dark green) and uL4 (light green) form the constriction site.

1.1.2 Translation

During translation initiation, the ribosome has to be positioned correctly at the start codon of the open reading frame on the mRNA to ensure productive protein synthesis in the following elongation. The most common start codon is AUG, but alternatively, two other codons GUG and UUG can be used (Gualerzi and Pon, 2015). In bacteria, many mRNAs carry a Shine-Dalgarno (SD) sequence in their 5’ untranslated region at a distance of 5-13 bases from the start codon. The SD sequence is complementary to the anti-SD sequence on the 30S subunit and by base-pairing of the SD and anti-SD sequences, the mRNA is positioned on the 30S subunit so that the start codon resides in the P site. Some mRNAs do not carry an SD sequence or do not possess a 5’ untranslated region; the mechanism of initiation on these mRNAs is poorly understood (Milon and Rodnina, 2012; Rodnina, 2018). In bacteria, the start codon is decoded by the initiator formyl-Met-tRNA (fMet-tRNA^{fMet}) that displays the anticodon complementary to the AUG codon. As a result, the first amino acid in every bacterial protein is fMet. Even though the elongator methionine tRNA (tRNA^{Met}), that is used to decode internal methionine codons, displays the same anticodon, other regions of the two tRNAs render them distinguishable. Both tRNAs are aminoacylated with methionine by methionyl-tRNA synthetase but only Met-tRNA^{fMet} is formylated by methionyl-tRNA transformylase (Figure 2). During formylation, a characteristic mismatch in the tRNA^{fMet} acceptor stem allows to bend the 3' arm of the tRNA so that the CCA end can reach the active site of the enzyme (Schmitt et al., 1998) and a formyl group from the formyl donor N^{10}-formyltetrahydrofolate is transferred to the alpha-amino group of methionine to form fMet-tRNA^{fMet} (Gualerzi and Pon, 2015; Laursen et al., 2005). In *Escherichia coli*, the transformylase is not essential, however, a deletion of the corresponding gene leads to a severe reduction of the growth rate which likely origins from a reduced efficiency in translation initiation (Guillon et al., 1992). The formyl group facilitates the interaction with initiation factor 2 (IF2) while hindering binding to the elongation factor Tu (EF-Tu), thereby ensuring selective use of fMet-tRNA^{fMet} during initiation (Gualerzi and Pon, 2015; Schmitt et al., 1996). Another feature of tRNA^{fMet} that distinguishes it from tRNA^{Met} is its more rigid anticodon stem, allowing for efficient accommodation in the P site during initiation.

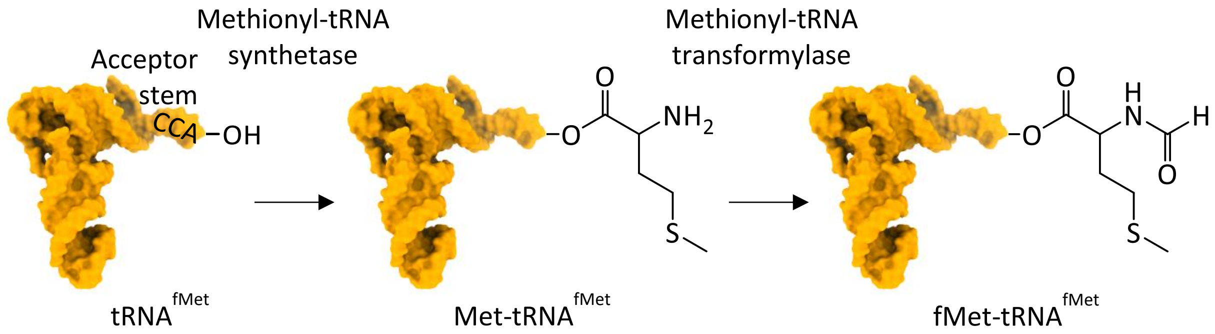

Figure 2. Two step formation of fMet-tRNA^{fMet} (PDB: 2FMT).

Three initiation factors IF1, IF2 and IF3 are required for bacterial translation initiation: IF1 acts as an enhancer for IF2 and IF3; the GTPase IF2 recruits fMet-tRNA^{fMet} to the 30S subunit; and IF3 ensures the selection of fMet-tRNA^{fMet} and suitable mRNAs and prevents premature association of the two ribosomal subunits (Rodnina, 2018). First, the 30S preinitiation complex is formed from the 30S subunit, IF1, GTP-bound IF2, IF3 and fMet-tRNA^{fMet} (Figure 3). The order in which the different factors associate with the small ribosomal subunit is not strictly regulated, however, a kinetically preferred route was determined from the association kinetics: IF2 and IF3 bind first and are then stabilized by IF1 which is followed by the recruitment of fMet-tRNA^{fMet} (Milon et al., 2012). Binding of mRNA occurs independently and depends rather on mRNA concentration and its intrinsic properties (Milon and Rodnina, 2012). With mRNA and initiator tRNA present, the anticodon loop of fMet-tRNA$^{\text{fMet}}$ recognizes the start codon, which leads to the formation of a stable 30S initiation complex. Next, the 50S subunit is recruited by interactions with IF2 and the initiator tRNA which induces GTP hydrolysis in IF2 leading to the accommodation of fMet-tRNA$^{\text{fMet}}$ in the P site (Rodnina, 2018). Finally, the initiation factors dissociate, completing the assembly of the 70S initiation complex (IC) that is ready for translation elongation.

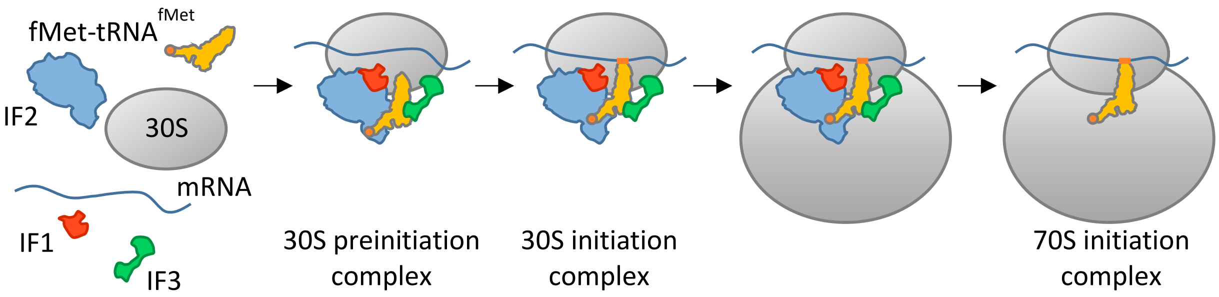

Figure 3. Initiation. Translation is initiated by the recruitment if IF3, IF2, and IF1 to the 30S subunit. This is followed by the recognition of the start codon and the association of the 50S subunit. After dissociation of the factors, the 70S IC can start translation.

In the process of elongation, amino acids are covalently attached to the growing polypeptide chain according to the sequence encoded in the mRNA (Figure 4). The first step of elongation is decoding, during which the codon in the A site is recognized by the matching (cognate) aa-tRNA (Rodnina, 2018). As there are 20 proteinogenic amino acids that are each carried by one or multiple isoacceptor tRNAs (Berg and Brandl, 2021), the ribosome has to discriminate against incorrect tRNAs. Elongator aa-tRNAs are delivered to the A site in a ternary complex with the GTPase EF-Tu and GTP and upon cognate base pairing of codon and anticodon, the decoding center in the 30S subunit undergoes conformational changes that trigger the GTPase activity of EF-Tu. As a consequence, aa-tRNA is released from EF-Tu–GDP and positions itself in the A site, while EF-Tu–GDP dissociates (Rodnina et al., 2017). To bind another aa-tRNA, EF-Tu has to exchange GDP for a new GTP molecule which is catalyzed by the elongation factor EF-Ts (Wieden et al., 2002). The next step in elongation is peptide bond formation where the alpha amino group of the A-site aa-tRNA nucleophilically attacks the ester bond of the P-site tRNA (Rodnina, 2018). Compared to the formation of a peptide bond in solution, the ribosome increases the reaction rate by a factor of 10^7 by lowering the entropy of activation (Sievers et al., 2004). As a result, the peptide chain is elongated by one amino acid and is now bound to the A-site tRNA, whereas the deacylated P-site tRNA displays a free hydroxyl group. Next, during translocation, the ribosome moves one codon forward on the mRNA with the help of the GTPase EF-G (Rodnina, 2018). GTP-bound EF-G engages the pre-translocation complex and unlocks the tRNA-mRNA module from the 30S subunit after GTP hydrolysis (Carbone et al., 2021; Petrychenko et al., 2021; Rodnina, 2018). Conformational changes in the 30S subunit allow the tRNAs to move to their post-translocation positions in the E and P sites; EF-G acts as a “ratchet” and ensures the forward directionality of translocation. Then, EF-G and the E-site tRNA dissociate, leaving the ribosome with the peptidyl-tRNA in the P site and empty A and E sites (Belardinelli et al., 2016; Rodnina, 2018). In a repetitive cycle of decoding, peptide bond formation and translocation, one amino acid after the other is added to the growing nascent chain, which moves through the peptide exit tunnel, until the whole protein is synthesized.

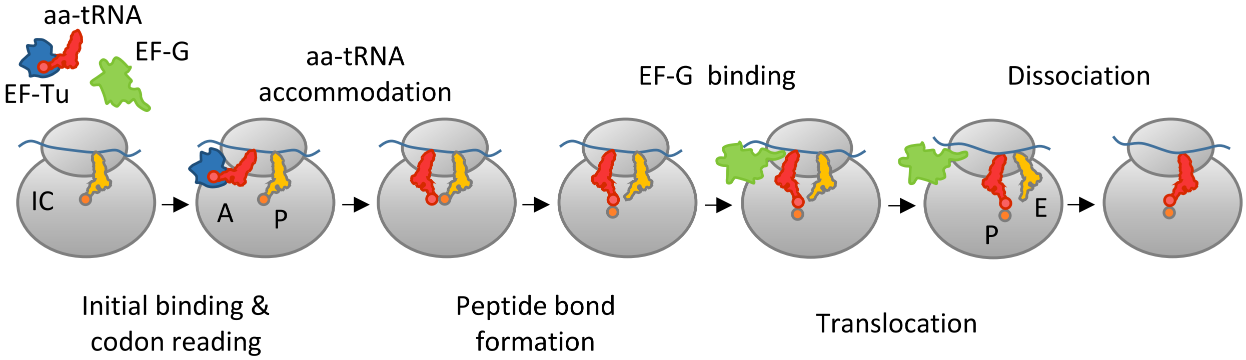

Figure 4. Elongation. aa-tRNA is delivered to the ribosome in complex with EF-Tu. After codon recognition and dissociation of EF-Tu, the peptide bond is formed between aa-tRNA in the A site and peptidyl-tRNA in the P site. EF-G promotes translocation of tRNAs to the P and E sites, followed by dissociation of the deacylated tRNA.

In the mRNA sequence, one of three stop codons signals the end of an open reading frame and initiates termination by recruiting release factor RF1 or RF2 that recognize the stop codon by forming specific interactions between the nucleotides of the stop codon and amino acids in RF1/2. In the presence of either release factor, the PTC catalyzes hydrolysis of the peptidyl-tRNA ester bond which results in release of the fully synthesized protein through the peptide exit tunnel. Dissociation of RF1 or RF2 proceeds with the help of the GTPase RF3. After termination, the mRNA and tRNA remain bound to the ribosome (Rodnina, 2018; Youngman et al., 2008). These are released by the ribosome recycling factor RRF and EF-G, which promote subunit splitting at the cost of GTP hydrolysis by EF-G (Gao et al., 2005). While the mRNA dissociates spontaneously, IF3 induces the dissociation of the tRNA from the 30S subunit (Peske et al., 2005; Rodnina, 2018).

1.2 Early protein maturation in bacteria

Newly synthesized proteins require assistance to achieve their correctly folded and modified, native state. The first proteins to interact with the nascent chain and fulfill this purpose are ribosome-associated protein biogenesis factors (RPBs) (Giglione et al., 2015; Koubek et al., 2021; Kramer et al., 2009). Because various kinds of polypeptides are being translated on the ribosome, RPBs engage in a number of different functions. In bacteria, peptide deformylase (PDF) and methionine aminopeptidase (MAP) are responsible for N-terminal processing, trigger factor (TF) is a chaperone and the signal recognition particle (SRP) targets inner membrane proteins and secretory proteins to the inner membrane. All RPBs can bind to the ribosome at the peptide exit tunnel, which allows them to scan translating and non-translating ribosomes for nascent chain substrates and act co-translationally (Bornemann et al., 2014; Holtkamp et al., 2012; Sandikci et al., 2013). Thus, the ribosome provides a platform where the timing and action of the different RPBs is coordinated.

1.2.1 Interplay between RPBs

Even though all RPBs interact with a large variety of different proteins, each RPB recognizes a subset of client proteins that are determined by cues in the nascent chain. Because RPBs act co-translationally, these signals are often located close to the N-terminus or in the N-terminal part of the nascent polypeptide (Figure 5). PDF, for example, interacts directly with the N-terminus as it catalyzes the removal of the formyl group from the N-terminal methionine. Most proteins in *E. coli* undergo deformylation, except for secretory proteins and membrane proteins that recruit SRP preventing the hydrolysis of the amide bond (Bienvenut et al., 2015; Ranjan et al., 2017). Deformylation is also the first step in N-terminal processing and a requirement for the subsequent cleavage of the initial methionine by MAP (Solbiati et al., 1999) which occurs on about 50% of all proteins depending on the nature of the second amino acid (Frottin et al., 2006; Giglione et al., 2015; Xiao et al., 2010; Yang et al., 2019). N-terminal processing produces diverse N-terminal amino acids, which modulates the half-life time of the new protein according to the N-degron pathway (Tobias et al., 1991). Another RPB, the protein-RNA complex SRP, targets inner-membrane proteins and secretory proteins to the membrane and specifically recognizes the signal peptide which is a hydrophobic α-helix near the N-terminus of a nascent chain (Kuhn et al., 2017; Mercier et al., 2022; Pool, 2005; Saraogi and Shan, 2014). As these client proteins are inserted into the membrane co-translationally, it is crucial that they are rapidly targeted to the membrane. TF acts as a chaperone mainly for cytosolic and outer-membrane proteins and interacts with short stretches enriched in basic and aromatic amino acids (Deckert et al., 2021; Koubek et al., 2021; Oh et al., 2011). In contrast to inner-membrane proteins, most outer-membrane proteins are translocated across the inner membrane post-translationally and in an unfolded state which is why they require chaperones (Oswald et al., 2021; Steinberg et al., 2018).

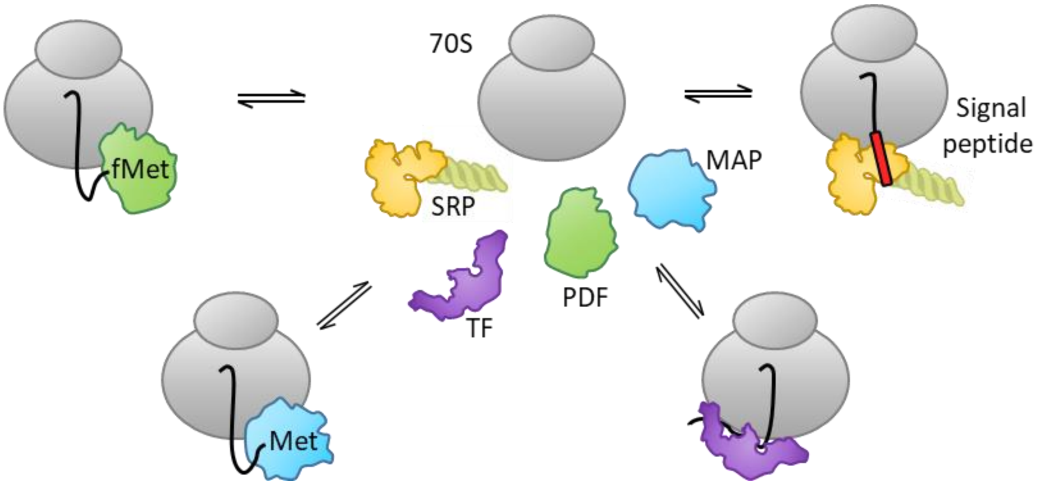

Figure 5. RPBs. PDF (green), MAP (blue), TF (purple) and SRP (yellow) interact with ribosomes displaying nascent chains substrates with their respective cues.

The ribosome provides a binding platform for the factors close to the emerging nascent chain and improves the organization between RPBs by mutual exclusion as factors that react to similar cues on the nascent chain show competitive binding. PDF and MAP can bind to the ribosome close to the peptide exit tunnel at the ribosomal protein uL22 (Figure 6) (Bhakta et al., 2019) and because their binding sites overlap, simultaneous binding of the two proteins at their primary binding site on the ribosome is precluded. MAP, however, interacts with the ribosome via positively charged amino acids which allow the peptidase to evade to a secondary binding site at uL23 when PDF is present (Bhakta et al., 2019; Sandikci et al., 2013). Both enzymes rapidly bind to and dissociate from the ribosome while scanning for their substrates and the competition for the ribosomal binding site enhances the selectivity of PDF and MAP to their respective substrates (Sandikci et al., 2013). TF binds with its N-terminal ribosome binding domain to a different site at uL23, (Kramer et al., 2002; Kristensen and Gajhede, 2003), which allows TF to arch over the polypeptide exit tunnel and accommodate nascent proteins (Ferbitz et al., 2004). In the cell, TF is in 2-3 fold excess over ribosomes (Lill et al., 1988) and as the dissociation constant (K_d) is around 0.1 µM

(Bornemann et al., 2014; Raine et al., 2006), nearly all ribosomes likely have one TF bound. TF dissociates rapidly from non-translating ribosomes, allowing the chaperone to scan for suitable substrates. TF and PDF can bind to the ribosome at the same time leading to a conformational change in TF (Bhakta et al., 2019; Bornemann et al., 2014). TF and MAP can also bind simultaneously (Bornemann et al., 2014), however, concurrent binding of all three RPBs is only observed at very high MAP concentrations and may impair TF function (Akbar et al., 2021; Bhakta et al., 2019). SRP and TF both interact with hydrophobic stretches and both bind to uL23 (Gu et al., 2003), displaying partially competitive binding to the ribosome and the nascent chain (Bornemann et al., 2014; Buskiewicz et al., 2004; Eisner et al., 2006; Ullers et al., 2006).

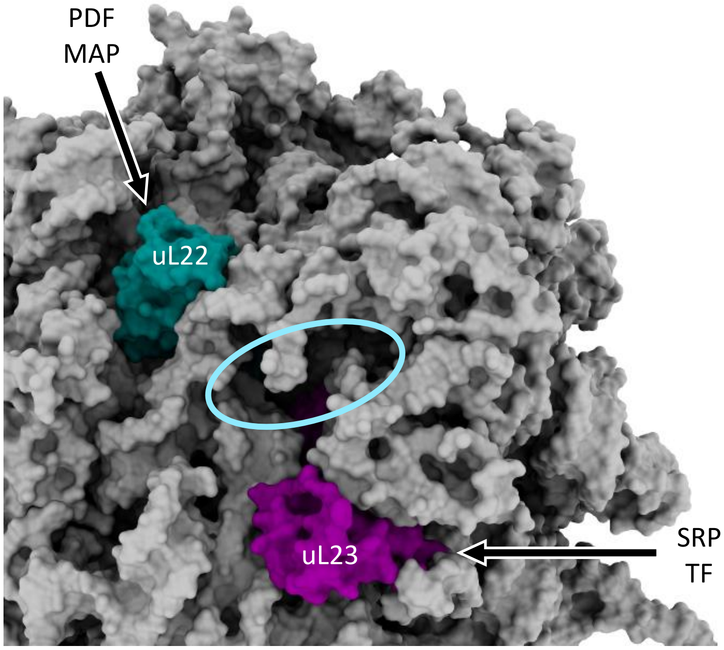

Figure 6. RPB binding sites on the ribosome. PDF and MAP bind the 50S subunit at uL22 (dark green) while SRP and TF interact with uL23 (purple). All binding sites are in close proximity to the peptide exit tunnel (light blue circle) (PDB: 4V5B).

Furthermore, the timing of RPB binding to ribosome nascent chain complexes (RNCs) is coordinated, as each RPB favors nascent chains of specific lengths (Figure 7). SRP is the first RPB to sense the nascent chain at a length of about 25 aa while it is still inside the exit tunnel (Bornemann et al., 2008; Denks et al., 2017). SRP remains bound to the ribosome in a stand-by mode allowing it to immediately bind to a signal peptide emerging from the peptide exit tunnel and prevent deformylation (Hainzl et al., 2011; Halic et al., 2006; Holtkamp et al., 2012; Mercier et al., 2017; Ranjan et al., 2017; Schaffitzel et al., 2006). In the absence of a signal peptide recruiting SRP, PDF can deformylate a nascent chain as soon as the N-terminus becomes accessible around a peptide length of 40-50 aa (Ball and Kaesberg, 1973; Giglione et al., 2015; Housman et al., 1972). With stalled RNCs, however, maximal PDF activity is achieved when the chain length is about 70 aa (Ranjan et al., 2017; Yang et al., 2019). Methionine removal by MAP does not show a preference for a specific nascent chain length but it can only act after the nascent chain is deformylated (Yang et al., 2019). Even though TF is bound to most ribosomes in the cell, including translating ribosomes with short nascent chains (Bornemann et al., 2014), a stable engagement of TF starts at a nascent chain length of 100 aa for most substrates (Oh et al., 2011). Therefore, nascent chains of cytosolic proteins are first modified by PDF, followed by MAP and then bound by TF.

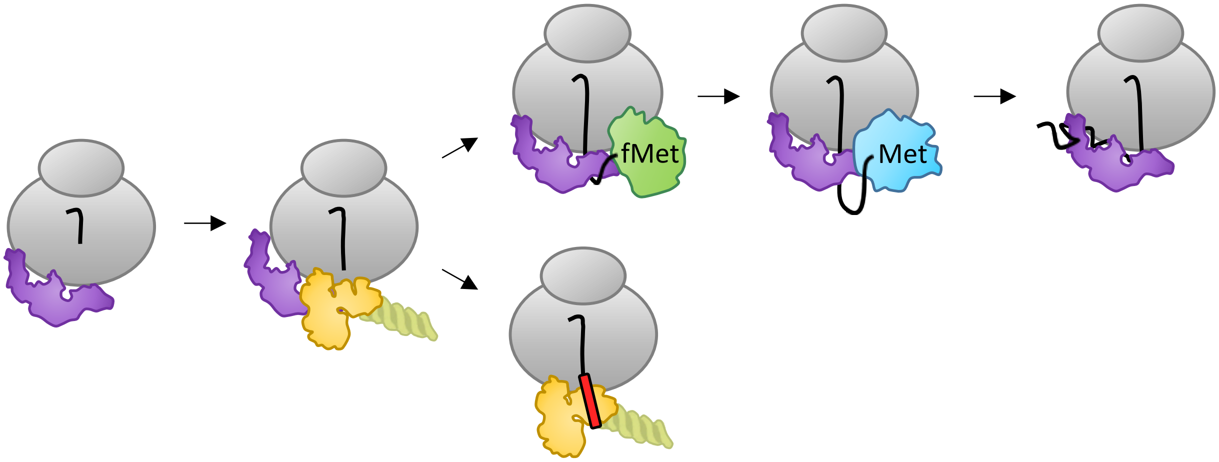

Figure 7. RPBs interact with nascent chains of different lengths. TF (purple) and SRP (yellow) bind translating ribosomes with short nascent chains. If the nascent chain contains a signal peptide (red), it will be targeted to the membrane by SRP. Otherwise, TF remains loosely bound to the ribosome and the nascent chain undergoes N-terminal processing by PDF (green) and MAP (blue) before TF binds more tightly.

As TF and SRP both interact with hydrophobic stretches on a nascent protein, the selection of client proteins by SRP is facilitated by interactions with the SRP receptor FtsY. Binding of SRP–TF–RNC complexes, that carry a nascent chain displaying a signal peptide, to FtsY displaces TF from the complex (Buskiewicz et al., 2004). On the other hand, TF slows down the recruitment of FtsY for suboptimal SRP substrates and reduces the affinity of SRP towards longer substrates, suggesting that if a protein has not been targeted to the membrane within a certain time, it will remain in the cytosol until it has been fully synthesized (Ariosa et al., 2015). Thus, interplay between TF, SRP and FtsY leads to efficient selection of nascent chains for different pathways.

1.2.2 Deformylation

PDF removes the N-terminal formyl group from nascent chains soon after the N-terminus emerges from the peptide exit tunnel. This process is essential for bacterial viability except when formylation of Met-tRNA^{fMet} is impaired (Mazel et al., 1994). While the necessity for formylation and deformylation most likely lies in the process of initiation, it has been suggested that fMet acts as a degradation signal to control for protein quality (Piatkov et al., 2015). PDF is a small α+β protein that binds to the ribosome at uL22 via its C-terminal helix (Figure 8) (Akbar et al., 2021; Bhakta et al., 2019; Bingel-Erlenmeyer et al., 2008; Chan et al., 1997). Two lobes of PDF fold around the active site containing a metal cofactor, Fe(II), which is coordinated by cysteine and two histidine residues (Chan et al., 1997; Meinnel et al., 1995; Rajagopalan et al., 1997b). The histidines are part of a HEXXH motif that is typically found in zinc metallopeptidases, whereas the cysteine belongs to the conserved EGCLS motif (Meinnel and Blanquet, 1995; Meinnel et al., 1995; Meinnel et al., 1997).

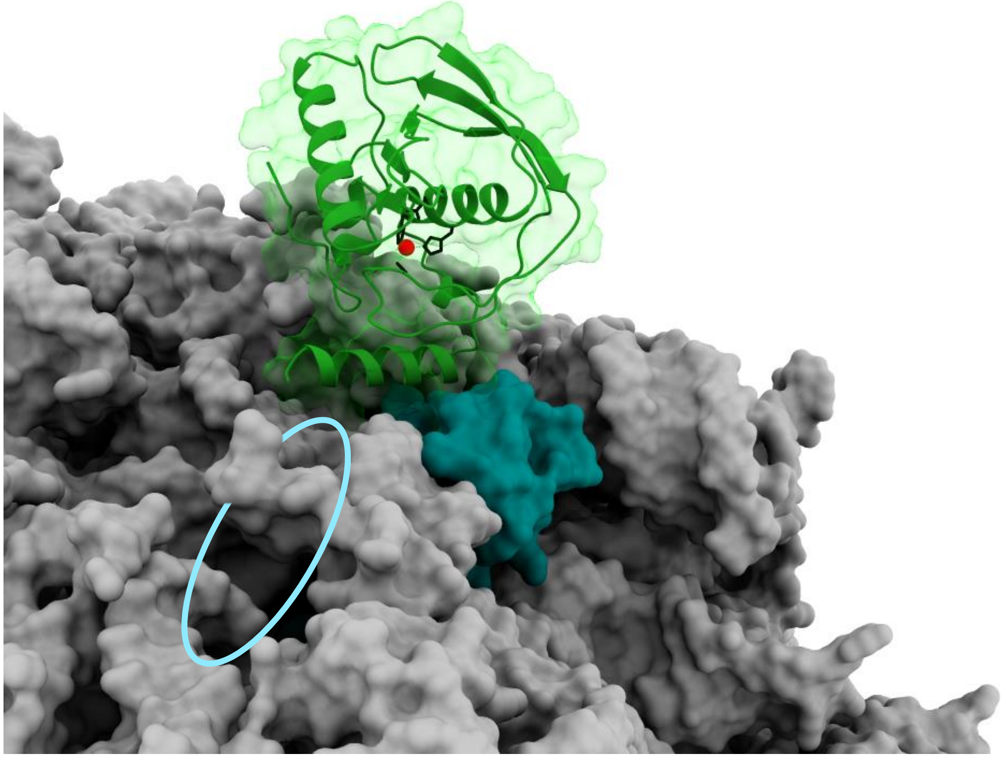

Figure 8. PDF bound to the ribosome. An Fe(II) ion (red) is coordinated in the active site of PDF (black). PDF (green) interacts with uL22 (dark green) in close proximity to the peptide exit tunnel (light blue circle) (PDB: 1DFF & 4V5B).

For *in vitro* studies, Fe(II) is commonly replaced with a less oxidation-sensitive metal ion such as Co(II), which does not significantly alter the enzyme's structure or activity (Jain et al., 2005; Rajagopalan et al., 2000). The metal ion coordinates a water molecule which is deprotonated by a glutamate in the active site and can execute a nucleophilic attack of the aldehyde carbon of the formyl group (Figure 9) (Rajagopalan et al., 2000; Xiao and Zhang, 2007). Thus, the enzyme catalyzes the hydrolytic cleavage of the formyl group from the N-terminal fMet of the nascent peptide, yielding a primary amine on the N-terminus and formic acid as reaction products. PDF accepts a large variety of different peptides but strongly prefers formylated over acetylated substrates (Hu et al., 1999; Meinnel and Blanquet, 1995; Ragusa et al., 1998; Rajagopalan et al., 2000). For efficient deformylation, a methionine is required as first amino acid which is positioned in a hydrophobic binding pocket of PDF called S1' cavity (Becker et al., 1998; Hu et al., 1999; Meinnel and Blanquet, 1995; Ragusa et al., 1999). The following three amino acids interact with PDF mainly via the peptide backbone so that any N-terminus can be deformylated, however, a preferred sequence is fMXZ where X is any amino acid apart from aspartate and glutamate and Z is lysine, arginine, phenylalanine or tyrosine (Becker et al., 1998; Hu et al., 1999; Ragusa et al., 1999; Rajagopalan et al., 1997a). Additionally, secondary structural elements like α-helices can slow down deformylation when they are close to the N-terminus (Ranjan et al., 2017).

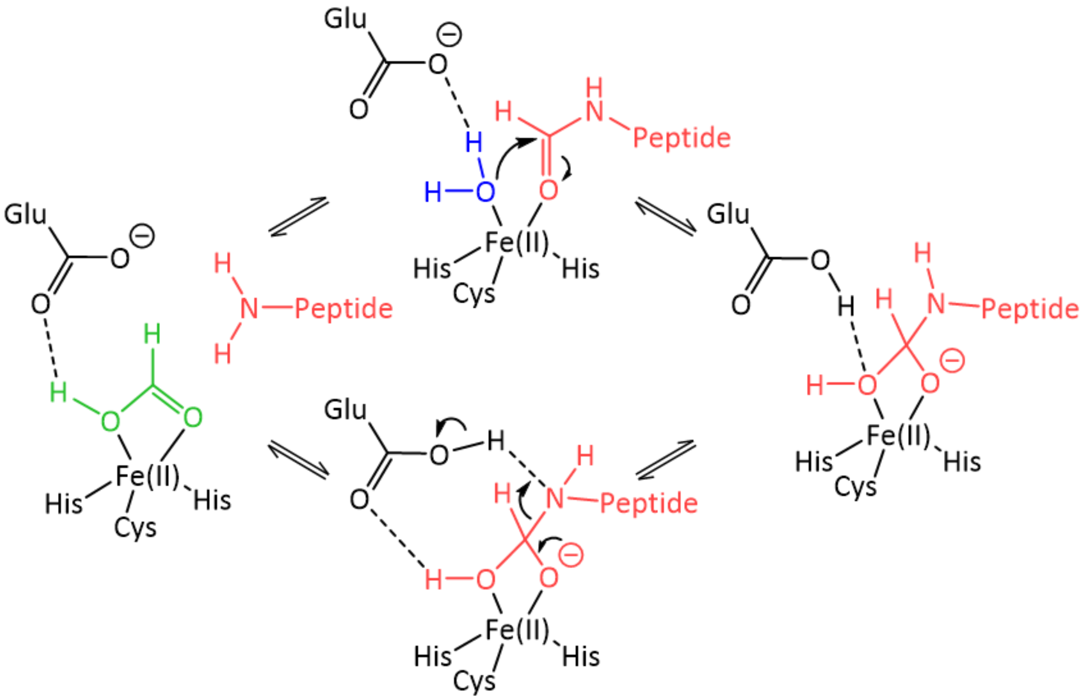

Figure 9. Catalytic mechanism of deformylation. A nucleophilic attack of a water molecule (blue) targeting the formylated peptide (red) is facilitated by a glutamate side chain. The reaction products are a peptide with a free amino group (red) and formic acid (green).

Recent kinetic measurements of MAP activity, which depend on the preceding action of PDF, suggest that the rate of nascent peptide deformylation is in the range of 1 s^{-1}, which is slow compared to the rate of protein synthesis (in the range of 10 s^{-1}) and limiting for the subsequent MAP reaction (Yang et al., 2019). The low deformylation rate on the ribosome is particularly surprising given that the nascent peptide directly faces PDF upon emergence from the exit tunnel, which should contribute to a pre-orientation effect favorable for catalysis (Figure 8) (Bingel-Erlenmeyer et al., 2008). Furthermore, kinetic studies of PDF-catalyzed deformylation using formylated peptides that mimic the N-terminus of nascent proteins, such as the chromogenic model substrate formyl-methionyl-leucyl-*p*-nitroaniline (fML-pNA) (Rajagopalan et al., 2000; Wei and Pei, 1997), revealed deformylation rates of 20-40 s^{-1} and up to 1,000 s^{-1} depending on the amino acid composition (Guo et al., 1999; Hu et al., 1999; Ragusa et al., 1998; Ragusa et al., 1999; Rajagopalan et al., 2000; Wei and Pei, 1997). As direct measurement of PDF-catalyzed nascent chain deformylation on the ribosome has not yet been reported, the kinetic mechanism of deformylation on the ribosome is not known, and the reasons underlying the slow reaction remain elusive.

1.2.3 PDF as drug target

Antibiotic resistance is a global health crisis of increasing urgency (Nikaido, 2009; Ventola, 2015). While bacteria like methicillin-resistant *Staphylococcus aureus*, multidrug-resistant *Mycobacterium tuberculosis* or *Neisseria gonorrhoeae* acquire resistances against more drugs, only a limited number of new antibiotics has been approved. Most antibiotics target one of three biological pathways in bacteria: DNA or RNA synthesis, protein synthesis or assembly of the cell wall (Kohanski et al., 2010). Because bacteria can use small modifications to existing resistance strategies to develop resistance against new antibiotics, it would be beneficial to inhibit a different pathway; in this respect, deformylation is a promising target to prevent rapid development of resistance against new antibiotic drugs.

Deformylation by PDF is essential and conserved in bacteria, which are important criteria for a new antibacterial target (Guilloteau et al., 2002). Additionally, PDF was long believed to be absent in vertebrates, as eukaryotic translation is initiated using a non-formylated methionine. Sequence analyses, however, identified PDF-like proteins in many eukaryotic species including humans (Giglione et al., 2000; Pei, 2001) which contain an N-terminal extension that targets them to the mitochondria (Lee et al., 2004; Nguyen et al., 2003; Serero et al., 2003). Even though 12 of the 13 proteins in bovine mitochondria are not deformylated (Walker et al., 2009), mitochondrial PDF is active *in vitro* but shows a drastically reduced activity compared to *Ec*PDF (Lee et al., 2003; Nguyen et al., 2003; Serero et al., 2003). Inhibition of *Hs*PDF decreases the number of active, mitochondrially-encoded proteins which reduces oxidative phosphorylation in mitochondria and may induce apoptosis so that PDF inhibitors could potentially also be used in anticancer treatment (Escobar-Alvarez et al., 2010; Lee et al., 2004; Randhawa et al., 2013; Sheth et al., 2014). In general, there are five classes of PDFs which are mainly determined by sequence similarities (Figure 10A) (Giglione et al., 2004). Type 1A is found in plants and animals and contains longer loops compared to type 1B that is found in plants and gram-negative bacteria. The C-termini of type 1B PDFs, which includes *Ec*PDF, are folded as α-helices while C-termini of type 2 PDFs, which can be found in gram-positive bacteria, are part of a β-sheet (Figure 10B). PDFs in archaea are supposedly non-active and form type 3. The active site and overall fold of active PDFs are well conserved (Baldwin et al., 2002; Escobar-Alvarez et al., 2009), however, the sequence identity between *Ec*PDf and *Hs*PDF amounts to only 30 % which results in actinonin, a natural PDF inhibitor, having a 100-fold lower IC_{50} with *Ec*PDF compared to *Hs*PDF (Nguyen et al., 2003; Serero et al., 2003). The peptide-like compound actinonin is a competitive inhibitor that binds to the active site metal with its hydroxamate moiety and to the S1' cavity with an n-butyl group (Figures 10C, D) (Chen et al., 2000; Clements et al., 2001). Therefore, it should be possible to develop inhibitors that specifically inhibit bacterial PDFs (Pei, 2001).

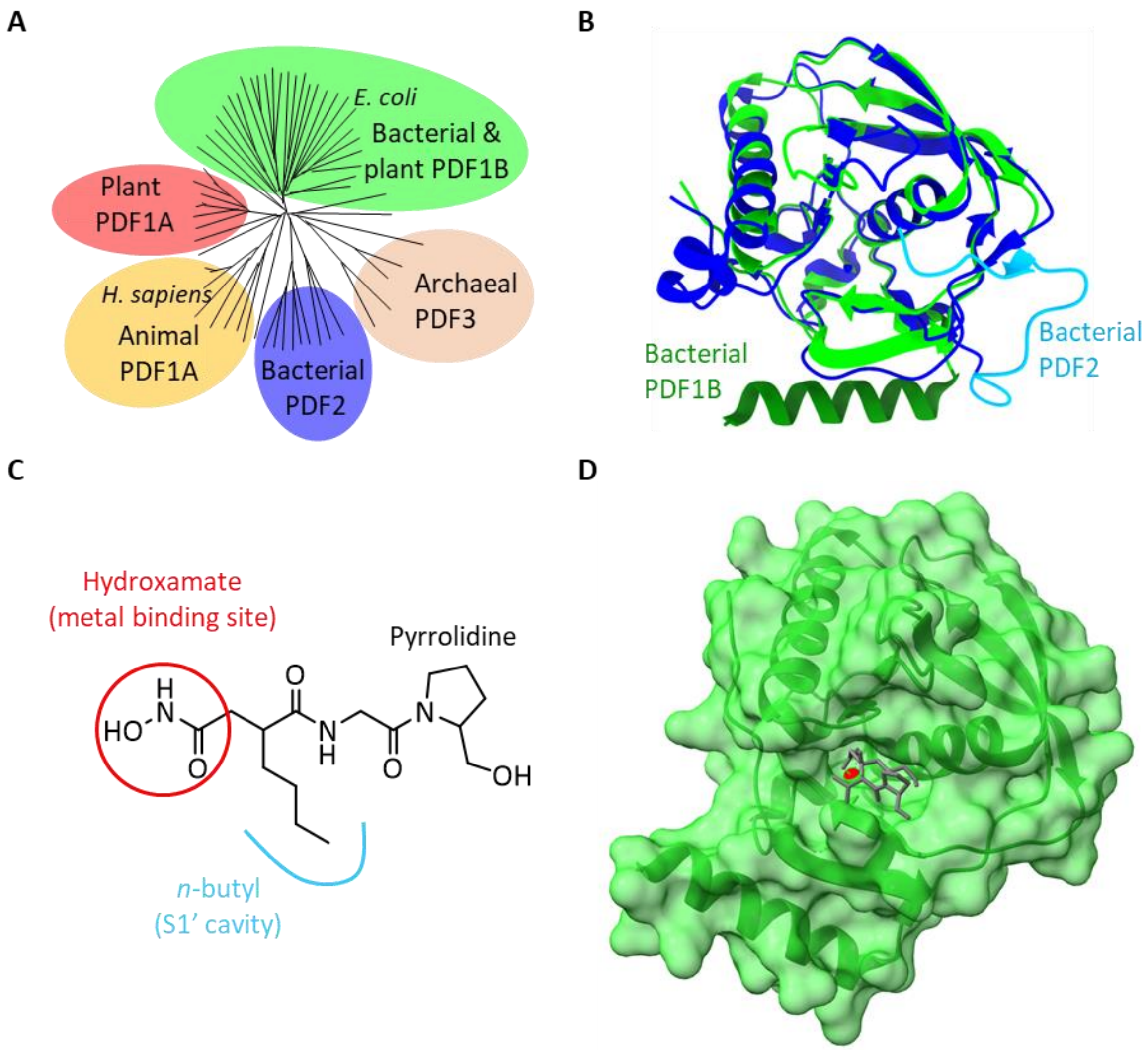

Figure 10. PDF inhibition.

(**A**) Phylogenetic diagram of PDF (adapted with permission from Springer Nature (Giglione et al., 2004)).

(**B**) Comparison of *Ec*PDF (Type 1B, green, PDB: 1G2A) and *Sa*PDF (Type 2, blue, PDB: 1Q1Y). The two PDFs mainly differ in the C-terminal helix of EcPDF (dark green) and the C-terminal β-sheet of SaPDF (light blue).

(**C**) Structure of the PDF inhibitor actinonin. The metal binding site (red) and S1' cavity binding side chain (blue) are indicated.

(**D**) *Ec*PDF (green) with actinonin (gray) bound to the metal cofactor (red) (PDB: 1G2A).

1.4 Biogenesis of membrane proteins

Membrane proteins, which represent about 30% of all proteins and are involved in key metabolic pathways as well as signal transduction and transport processes, are selected for different biogenesis pathways with the help of RPBs. Outer membrane proteins are typically β-barrels that are recognized by TF for post-translational insertion into the lipid bilayer. In contrast, inner membrane proteins consist of α-helical bundles and are bound by SRP that targets them to the membrane co-translationally. Inner membrane proteins are inserted into the lipid bilayer via the translocon and start to fold into their native structure while their synthesis continues on the ribosome.

1.4.1 Targeting

In nascent membrane proteins, usually the first α-helical transmembrane helix (TM) is recognized by SRP which is then also called a signal anchor sequence (SA) (Schibich et al., 2016). SRP binds the nascent chain with high affinity depending on the hydrophobicity of the SA (Bornemann et al., 2008; Mercier et al., 2017; Zhang et al., 2010). Because the dissociation rate of the cognate ribosome-SRP complex is very low, SRP remains bound to the nascent chain until the complex reaches the membrane and prevents the hydrophobic SA from aggregation (Holtkamp et al., 2012; Mercier et al., 2017; Noriega et al., 2014; Saraogi et al., 2014). For efficient membrane targeting, FtsY is activated by binding to the translocon (Draycheva et al., 2016) and binding of SRP to FtsY brings the RNC in close proximity of the translocon. After a conformational rearrangement of SRP and FtsY to vacate space at the peptide exit tunnel, the SA is released from SRP and can insert into the translocon (Draycheva et al., 2018; Jomaa et al., 2016; Jomaa et al., 2017).

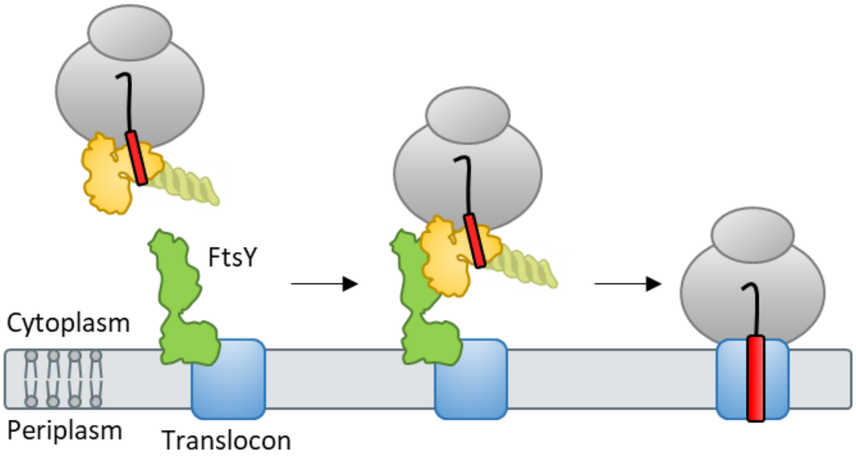

Figure 11. Targeting. An inner-membrane protein (red) is targeted to the translocon (blue) with the help of SRP (yellow) and FtsY (green).

The translocon is a ubiquitous membrane protein complex which is formed by SecYEG in bacteria and Sec61αβγ in eukaryotes and is responsible for the co-translational insertion of membrane proteins into the lipid bilayer. With 10 TMs, SecY is the main protein forming the protein-conducting channel while SecE and SecG bind at the periphery (Figure 12A) (Breyton et al., 2002; Van den Berg et al., 2004). In its inactive state, the channel is closed by a plug domain that can open to allow the translocation of secretory proteins into the periplasm (Van den Berg et al., 2004; Zimmer et al., 2008). In the presence of a TM, the two halves of the translocon open and the lateral gate helices TM2b and TM7 move apart so that the membrane protein can partition into the lipid bilayer (Figure 12B) (Egea and Stroud, 2010; Ge et al., 2014; Hizlan et al., 2012; Park et al., 2014). In general, the lateral gate is highly dynamic and can sample different states between open and closed conformations (Mercier et al., 2021). The cytoplasmic side of the translocon binds to the ribosome at the peptide exit tunnel (Bischoff et al., 2014; Frauenfeld et al., 2011; Park et al., 2014), and two cytoplasmic loops of SecY enter the exit tunnel, substantially reducing the size of the vestibule and the exit tunnel remains narrow with a range of 5-10 Å (Figure 12C,D) (Frauenfeld et al., 2011). Together, the ribosome and the translocon form a continuous channel through which the nascent chain is guided towards the membrane. However, there is a gap at the interface between the two complexes that potentially allows space for cytoplasmic loops of the nascent protein (Park et al., 2014). Apart from this gap, the nascent membrane protein is shielded from the aqueous environment over a distance of 140 Å from the PTC (Mercier et al., 2022).

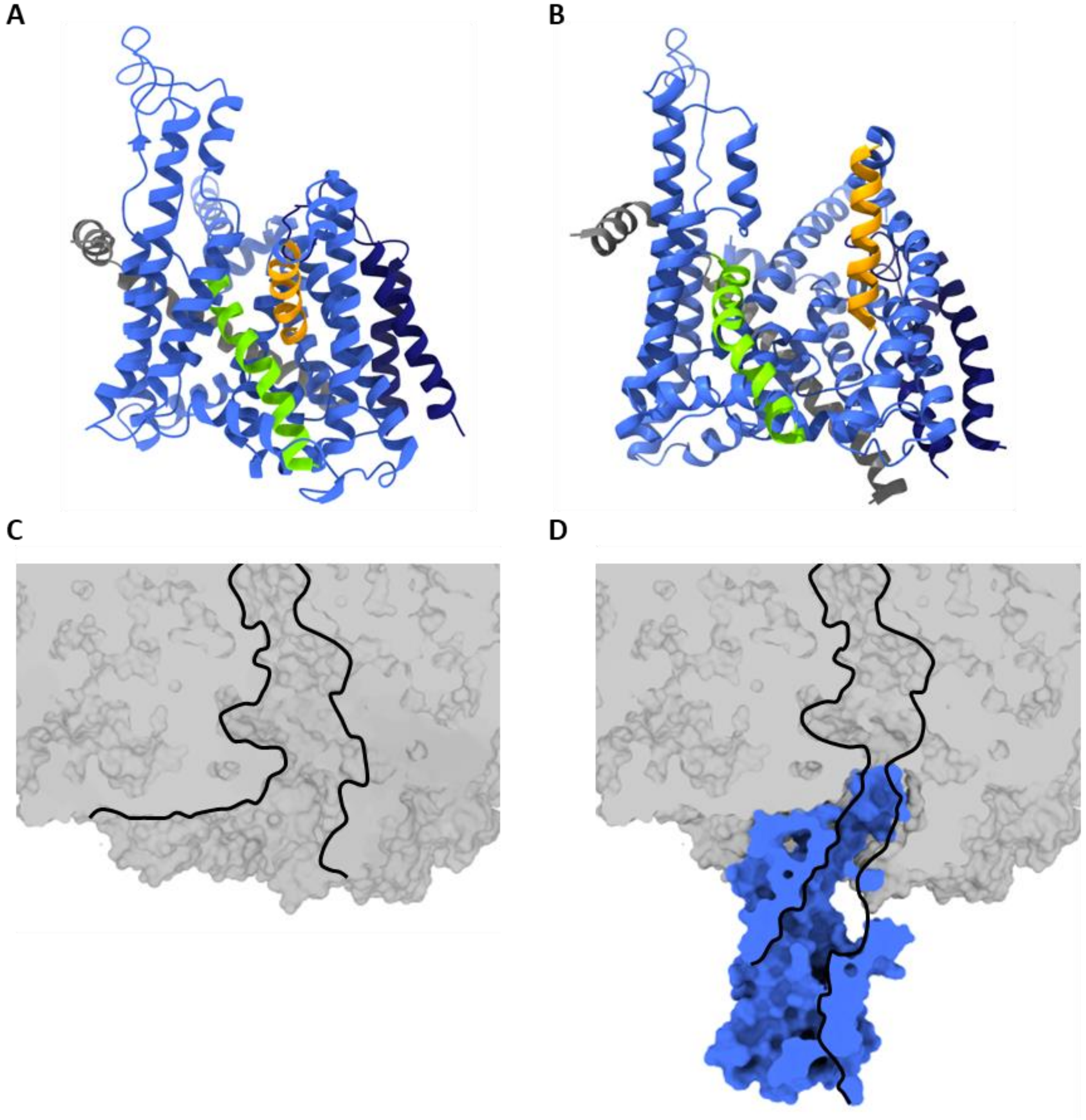

Figure 12. The translocon.

(**A**) Structure of the closed conformation of the translocon. SecY (blue) forms the main channel with the lateral gate helices TM2B (orange) and TM7 (green). SecE (gray) and SecG (dark blue) are bound on the side (PDB: 3J45).

(**B**) Open state of the translocon (PDB: 3J46).

(**C**) Lower peptide exit tunnel and vestibule (black) at the ribosome (gray) (PDB: 4V6M).

(**D**) When the translocon (blue) is bound to the ribosome, a continuous channel is formed (PDB: 4V6M).

1.4.2 Co-translational protein folding

Classically, protein folding was studied through spontaneous refolding of denatured proteins. However, proteins start to fold co-translationally inside the peptide exit tunnel soon after the nascent chain passed the constriction site (Cassaignau et al., 2020; Koubek et al., 2021; Liutkute et al., 2020b; Waudby et al., 2019). Therefore, folding is directional starting from the N-terminus and begins before the whole protein or domain is synthesized. Due to the limited size and defined environment inside the peptide exit tunnel, the ribosome can reshape the folding energy landscape compared to the folding of a full-length protein in the membrane which may allow the nascent chain to evade kinetic traps. Additionally, the ribosome can destabilize folding until, for example, the synthesis of a domain is completed (Bitran et al., 2020; Deckert et al., 2021; Kaiser et al., 2011; Kudva et al., 2018; Liutkute et al., 2020a; Nilsson et al., 2017). In the case of membrane proteins, the translocon acts as an extension of the ribosome exit tunnel and may convey a similar function. TMs are retained at the translocon where they start interacting with each other, suggesting that the translocon could act like a chaperone for membrane proteins (Bischoff et al., 2014; Frauenfeld et al., 2011; Hou et al., 2012; Park et al., 2014; Sadlish et al., 2005).

Figure 13. Three state membrane protein folding model. TMs are inserted into the membrane, then assemble into bundles and finally, incorporate cofactors or multimerize.

Inside the exit tunnel, TMs can compact and form α-helices (Robinson et al., 2012; Woolhead et al., 2004) that seem to be favored by the ribosome because even the β-barrel protein CspA was shown to assume a helical conformation within the tunnel (Agirrezabala et al., 2022). Furthermore, small domains of cytosolic proteins can fold inside the vestibule of the exit tunnel (Holtkamp et al., 2015; Mercier and Rodnina, 2018; Nilsson et al., 2015). Folding of membrane proteins into their native structure, however, has been proposed to occur according to a three stage model in the lipid bilayer (Figure 13) (Engelman et al., 2003). First, the TMs are inserted into the membrane, next they start folding into helical bundles and finally the structure is further stabilized by the folding of loops, binding of cofactors or multimerization. Inside the lipid bilayer, interactions between TMs are often conveyed by knobs-into-holes packing which is characterized by a GxxxG sequence motif (Cymer et al., 2015; Senes et al., 2004). The packing permits the TMs to form close contacts and formation of extensive van der Waals interactions. Hydrogen bonding between polar amino acids Asn, Asp, Gln and Glu can further stabilize TM binding (Gratkowski et al., 2001; Senes et al., 2004; Zhou et al., 2001) as well as the formation of serine zippers (Adamian and Liang, 2002). Recently, the stabilization of a membrane protein by TM-TM interactions was also shown co-translationally (Nicolaus et al., 2021).

1.4.3 Insertion into the membrane

Membrane proteins can insert into the membrane in two different orientations. If the N-terminus reaches into the cytosol, it is an N-in protein while the N-terminus of an N-out protein points towards the opposite side of the membrane. The topology is mainly determined by positively charged amino acids which are retained inside the cytosol according to the positive inside rule (von Heijne, 1989, 1992). In the case of an N-out protein, the N-terminus is negatively charged or neutral and can insert into the translocon head-on (Mercier et al., 2020). A TM with an N-in topology, however, has to invert for the positively charged N-terminus to remain in the cytosol. It is not clear how exactly a TM inverts but the positively charged amino acids are most likely retained by interactions with negative charges on the ribosome (Mercier et al., 2020) or the lipid bilayer (Dowhan et al., 2019), as well as the membrane potential (Cao et al., 1995). Two different mechanisms were proposed to explain how inversion and insertion might occur at the translocon (Figure 14). In the sliding model, TMs first sample the bilayer-water interface until the whole TM is located outside the peptide exit tunnel (Cymer et al., 2015). Then, the TM inserts into the translocon with the periplasmic end leading the way, but only the periplasmic loop enters the translocon channel. The hydrophobic TM slides through the open lateral gate while remaining in contact with the lipids (Martoglio et al., 1995). Energetically, the translocon resembles the bilayer interface so that there is no barrier for insertion (Marx and Fleming, 2021). In the translocon-insertion model, the N-terminus inverts early on inside the ribosome and the nascent chain assumes a looped conformation (Kim and Skach, 2012; Mercier et al., 2022; Mercier et al., 2020). As soon as the nascent chain is long enough, the inverted TM enters the translocon pore from where it can partition into the lipid bilayer.

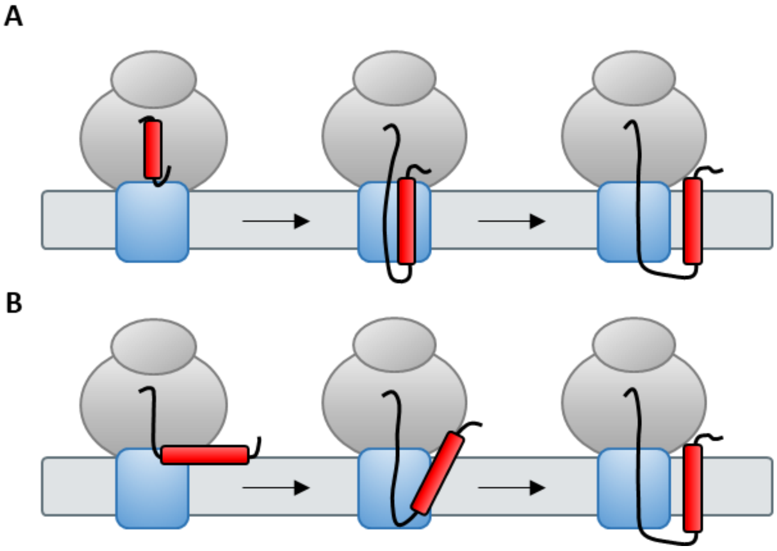

Figure 14. Insertion of N-in TM.

(**A**) Translocon-insertion model. N-terminus and TM invert inside the ribosome, insert into the translocon and partition into the membrane.

(**B**) Sliding model. The TM first samples the membrane interface before it slides along the lateral gate into the lipid bilayer.

Insertion of TMs into the membrane can occur in one of three different fashions (Skach, 2009). Either TMs enter the lipid bilayer sequentially, one after the other or they form a helix-turn-helix conformation and insert pairwise (Figure 15). Another option is the formation of larger TM bundles which is less likely due to the limited size inside the translocon. Even in a dimer, one TM is most likely positioned at the lateral gate due to size restrictions as suggested by structural studies (Frauenfeld et al., 2011; Park et al., 2014). Even though the insertion and topogenesis of TM1 was recently probed co-translationally (Mercier et al., 2020), it is not known how internal TMs are inserted, whether they follow the translocon-insertion or the sliding model and if TMs enter the lipids in a sequential or pairwise manner.

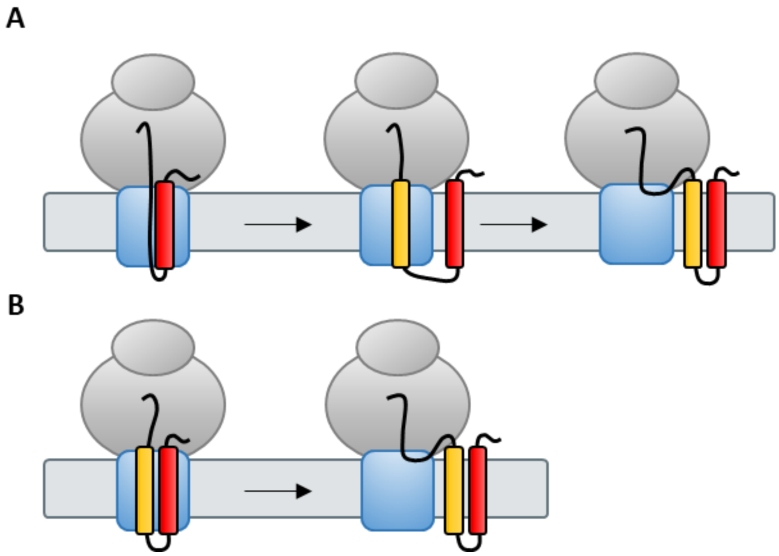

Figure 15. Membrane insertion.

(**A**) Sequential insertion. TM1 and TM2 enter the lipid bilayer individually.
(**B**) Pairwise insertion. TM1 and TM2 form a dimer before they insert into the membrane.

1.4.4 EmrD

For bacteria, one way to achieve antibiotic resistance is the expression of multidrug resistance transporters that export a large variety of substrates from the cytoplasm (Nikaido, 2009; Putman et al., 2000). The inner-membrane protein EmrD is such a transporter and part of the major facilitator superfamily (MFS) which is the largest family of secondary antiporters (Law et al., 2008; Pao et al., 1998). In contrast to primary transporters or pumps that employ ATP hydrolysis, EmrD uses the electrochemical gradient over the membrane as energy source for translocation (Paulsen et al., 1996). Substrates of EmrD are amphipathic substances from the cytosol like detergents or uncouplers of oxidative phosphorylation

(Naroditskaya et al., 1993; Nishino and Yamaguchi, 2001) and molecular dynamics simulations indicate that EmrD can also export substrates from the cytoplasmic leaflet of the inner membrane (Baker et al., 2012). Exported compounds are bound in a mostly hydrophobic internal cavity that is formed between the two halves of the 12 TM protein and transportation against the proton gradient is facilitated by a rocker-switch model where EmrD provides alternating access to either side of the membrane (Law et al., 2008; Yin et al., 2006). Structurally, EmrD is an N-in protein with an 8 amino acid-long N-terminal loop reaching into the cytoplasm. TMs 1-6 as well as TMs 7-12 form 6 helix bundles that are symmetric to a 2-fold axis and are connected by a long loop (Figure 16) (Yin et al., 2006). Interestingly, TM4 is positioned between TM1 and TM2 in the natively folded structure, which raises the questions whether this motif is formed co-translationally and whether the translocon is required to act as a chaperone during folding.

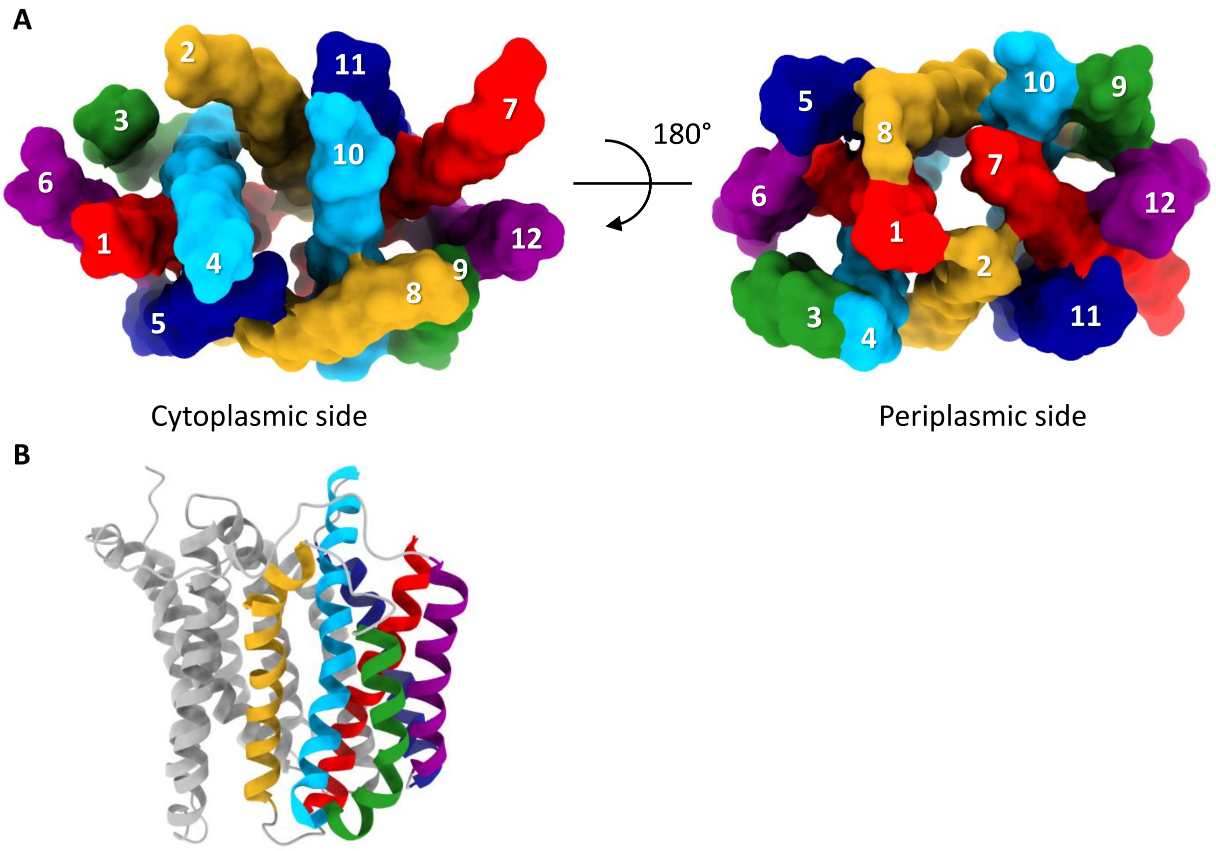

Figure 16. EmrD.

(**A**) Cytoplasmic and periplasmic view of EmrD as surface representations of the helix backbones. Numbers correspond to the order of TMs in the sequence (PDB: 2GFP).

(**B**) Side view of EmrD with TM1-6 colored as in (**A**) (PDB: 2GFP).

1.5 Scope of thesis

During the biogenesis of proteins in bacteria, interactions of RPBs with RNCs coordinate nascent chain processing, folding and targeting. While a nascent protein is synthesized on the ribosome, PDF deformylates the N-terminus soon after it emerges from the peptide exit tunnel, but the reaction is slow compared to the rate of translation, even though PDF acts rapidly on formylated peptides. By studying the kinetic mechanism of deformylation using RNCs, we set out to determine the rate-limiting step in deformylation on the ribosome to understand why deformylation of RNCs is slow and how this influences the interplay with other RPBs like MAP. We further performed co-translational deformylation experiments to analyze how ongoing protein synthesis impacts deformylation and determined the inhibitory effect of the PDF inhibitor fumimycin and its analogues to resolve whether they are candidates for antibiotic drugs.

Membrane proteins are targeted to the lipid bilayer by SRP which allows them to bypass the slow step of deformylation so that they are efficiently inserted into the membrane via the translocon. TMs of a polytopic membrane protein are inserted into the translocon pore first and then partition into the lipids through the lateral gate region, but the relation between consecutive TMs during co-translational insertion and folding has not been understood yet. Using the multidrug resistance transporter EmrD as a model system, we performed co-translational Förster resonance energy transfer (FRET) experiments to determine whether TMs are inserted into the membrane simultaneously or sequentially, when protein folding starts and whether the translocon assists in folding.

2 Results

2.1 Kinetic control of nascent protein biogenesis by peptide deformylase

2.1.1 Rate-limiting step occurs after rapid deformylation

In order to tease apart the kinetic mechanism of deformylation on the ribosome and identify the rate-limiting step, we first confirmed the presence of a slow step which was indicated by previous studies (Yang et al., 2019). For this purpose, we determined the rate of nascent-chain deformylation at conditions of multiple turnover for PDF. As deformylation occurs co-translationally *in vivo*, RNCs were used to mimic a nascent protein during its synthesis on the ribosome as opposed to earlier kinetic studies of PDF which were mainly performed on peptide substrates. We prepared RNCs carrying 75 aa-long nascent chains, which is an optimal length for deformylation on the ribosome (Ranjan et al., 2017; Yang et al., 2019) and which were labeled with f[^{35}S]Met on the N-terminus. After incubation of RNCs with PDF and subsequent proteinase K (PK) digestion, f[^{35}S]Met and [^{35}S]Met were separated by thin-layer chromatography (TLC) and visualized by phosphoimaging (Figure 17A). Oxidized material fMet(ox) and Met(ox) revealed different deformylation kinetics and was dismissed. We measured time courses of deformylation (Figure 17B) and determined Michaelis-Menten constants k_{cat} and K_M from the concentration-dependent initial velocities of four RNC substrates carrying different nascent peptides, proOmpA, RNaseH, TolB and DnaK (Figure 17C; Table 1). Previous studies indicated that these substrates are efficiently deformylated albeit at different rates, making them suitable substrates to study (Ranjan et al., 2017). We also examined the Michaelis-Menten kinetics of PDF acting on the dipeptide substrate fML-pNA for comparison (Table 1). For different RNCs, the K_M values are similar within a factor of two, whereas k_{cat} values vary about six-fold, between 0.04 s^{-1} and 0.26 s^{-1}. For all RNCs, k_{cat} values are at least 60 times lower than for model substrates (Table 1 and (Guo et al., 1999; Rajagopalan et al., 2000; Wei and Pei, 1997)). The variations in k_{cat} observed for different RNCs can be explained by the effect of the N-terminal amino acid sequence or structure on deformylation velocity (Hu et al., 1999; Ranjan et al., 2017). The K_M values for the RNCs are about 100-fold lower than those for fML-pNA (Table 1), which in the simplest model, reflects stabilization of the PDF-nascent-chain complex by binding of PDF to the ribosome. The k_{cat}/K_M values are in the same order of magnitude for RNCs and fML-pNA, and similar to the value obtained with a different RNC substrate (Yang et al., 2019), indicating a similar catalytic efficiency on and off the ribosome, despite largely different k_{cat} and K_M values. The smaller k_{cat} values for RNCs compared to fML-pNA point towards a rate-limiting step in the mechanism of deformylation that is specific to RNCs.

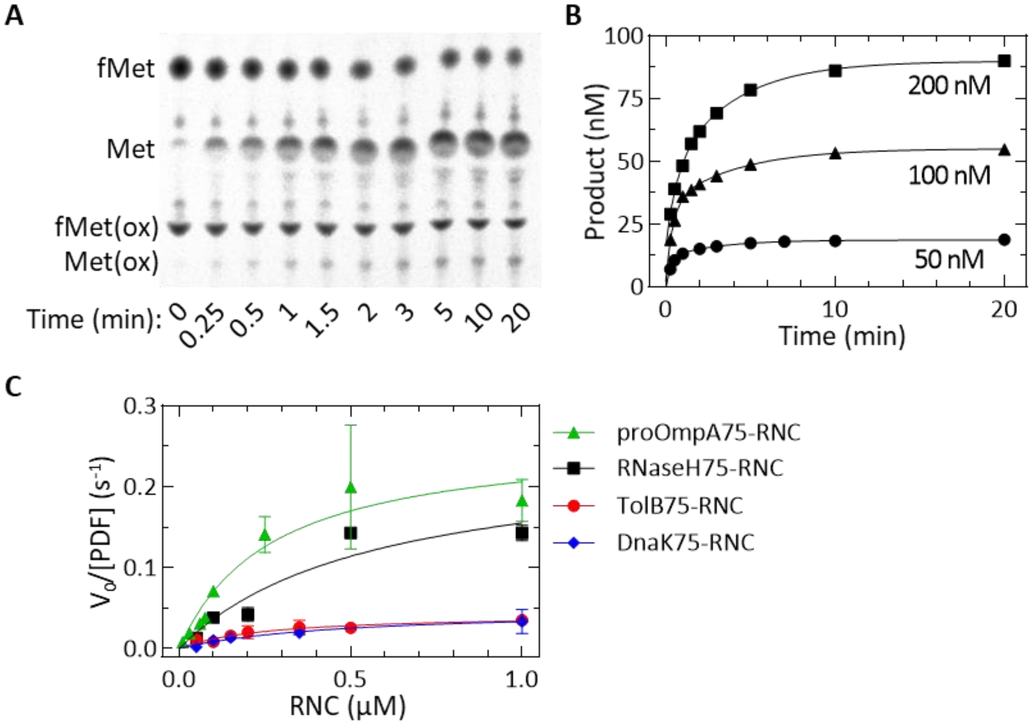

Figure 17. RNC deformylation at multiple turnover conditions.

(**A**) Time course of RNaseH75-RNC (100 nM) deformylation by PDF (10 nM) at 37°C monitored by TLC. fMet and Met as well as the oxidized species fMet(ox) and Met(ox) were detected.

(**B**) Deformylation time courses of increasing concentrations of RNaseH75-RNC by PDF (10 nM).

(**C**) Michaelis-Menten plot. Initial velocities (V_o) are normalized by the concentration of PDF (10 nM for RNaseH75-RNC, TolB75-RNC, DnaK75-RNC; 1 nM for proOmpA75-RNC). Michaelis-Menten fits (lines) yield the parameters summarized in Table 1. Error margins indicate standard errors determined from linear fitting of individual time courses.

Table 1. Michaelis-Menten parameters of deformylation by PDF. Errors represent standard errors of the fit (Figure 1C) using the Michaelis-Menten equation. Deformylation of the formylated peptide fML-pNA was monitored photometrically (Methods).

Substrate	K_M (µM)	k_{cat} (s^{-1})	k_{cat}/K_M ($\mu M^{-1}s^{-1}$)
RNaseH75-RNC	0.6 ± 0.5	0.24 ± 0.09	0.4
proOmpA75-RNC	0.3 ± 0.1	0.26 ± 0.04	0.9
TolB75-RNC	0.25 ± 0.08	0.04 ± 0.01	0.2
DnaK75-RNC	0.5 ± 0.2	0.05 ± 0.01	0.1
fML-pNA	24 ± 6	16 ± 2	0.7

To help identify the slow step, the rate of deformylation was measured at conditions where the reaction is not limited by enzyme turnover. To ensure that the binding of PDF to the ribosome is rapid compared to the chemistry step and that the substrate is converted to product in a single round, a large excess of PDF over RNC was used (Figure 18A). The reaction started upon rapid mixing of RNC and PDF in a quench-flow apparatus and, after the indicated incubation times, samples were quenched and analyzed by TLC to determine the product:substrate ratio. Reaction end-level values quantified in parallel experiments indicated that 90 ± 2% of DnaK75-RNC and 78 ± 4% of TolB75-RNC was converted to product (Figure 18B). Time courses were fitted with single-exponential functions to obtain deformylation rates of 33 ± 8 s^{-1} for DnaK75-RNC and 60 ± 20 s^{-1} for TolB75-RNC (Figure 18A) which are not significantly different and were therefore averaged (k_{app} = 50 ± 20 s^{-1}). These rates are comparable to the k_{cat} measured with the model dipeptide off the ribosome (Guo et al., 1999; Rajagopalan et al., 2000; Wei and Pei, 1997) and 1,000-fold higher than the k_{cat} values of the reaction on the ribosome measured at multiple-turnover conditions (Table 1). Thus, the chemistry step of the PDF-catalyzed deformylation is intrinsically rapid, and the rate-limiting step of the reaction on the ribosome must take place after hydrolysis.

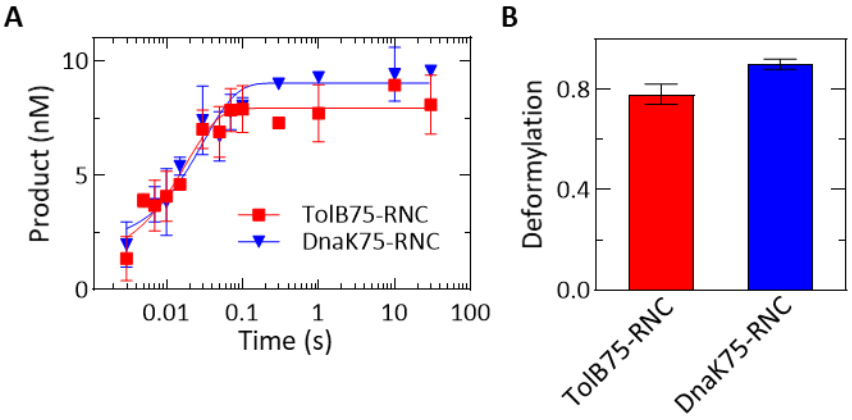

Figure 18. Pre-steady-state kinetics of RNC deformylation.

(**A**) DnaK75-RNC or TolB75-RNC (10 nM final concentration) were rapidly mixed with a saturating concentration of PDF (25 µM at 37°C and quenched at indicated times. Time courses were evaluated by fitting to a single-exponential function and error margins represent the standard deviation of three independent experiments.

(**B**) End level of deformylation of TolB75-RNC and DnaK75-RNC (10 nM) after incubation with PDF (25 µM) for 10 min at 37°C. Error margins represent the standard deviation of four independent experiments.

2.1.2 Rapid association and dissociation of the PDF-RNC complex

In the turnover reaction, product dissociation can be rate-limiting. To test whether this could explain the slow turnover of PDF, we incubated TolB75-RNC with PDF to deformylate the nascent chain and then measured dissociation of the PDF-RNC complex via changes in the fluorescence of Bodipy (Bpy) attached to the C-terminus of PDF. Upon mixing the labeled PDF(C-term)-RNC complex with an excess of unlabeled PDF in the stopped-flow apparatus, the fluorescence intensity decreases rapidly, indicating fast dissociation of PDF(C-term) from the complex. The rate constant of dissociation obtained by single-exponential fitting of this trace is 27 ± 3 s^{-1} at 10°C (Figure 19A). Following previous studies (Sandikci et al., 2013) we used lower reaction temperatures for these dissociation experiments because no signal change was observed at 37°C. Assuming the typical temperature dependence of enzymatic reactions, the dissociation is expected to be faster at 37°C. Since dissociation of PDF from deformylated RNCs is rapid, it cannot explain the slow PDF turnover observed under multiple-turnover conditions. PDF was found to dissociate from vacant ribosomes at a rate of 33 ± 3 s^{-1}, which is not significantly different from the rate observed with deformylated RNCs (Figure 19A). This suggests that here we monitor a step in which PDF dissociates from its contact site on the ribosome, rather than the release of PDF from the nascent chain.

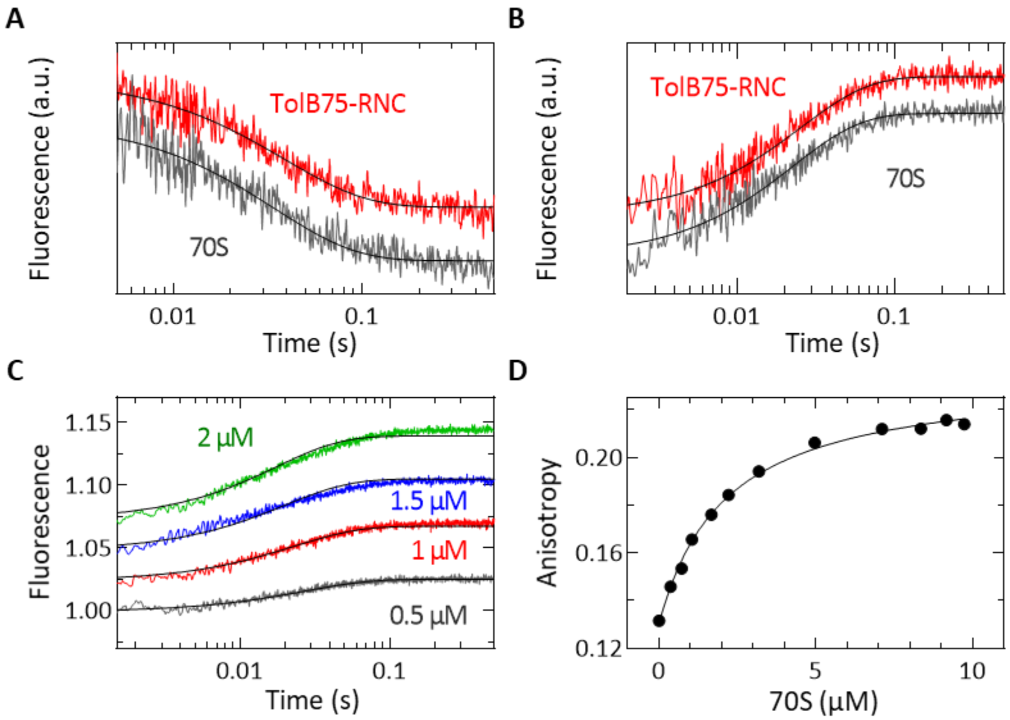

Figure 19. Interaction of PDF with TolB75-RNC and vacant 70S ribosomes. In panels (A, B), time courses are shifted on the Y-axis for clarity.

(**A**) Dissociation experiments. Dissociation of 70S–PDF(C-term) or RNC–PDF(C-term) (150 nM) upon addition of excess unlabeled PDF (15 µM) were measured at 10°C. Eight technical replicates were averaged for each trace and smooth lines represent single-exponential fits.

(**B**) Association time courses. Binding was monitored upon rapid mixing of PDF(C-term) (300 nM) with 70S ribosomes or TolB75-RNC (420 nM) at 10°C. Six technical replicates were averaged and evaluated by single-exponential fitting (smooth lines).

(**C**) Binding of PDF(C-term) (100 nM) to 70S ribosomes (0.5-2 µM) monitored by fluorescence intensity changes at 10°C. Each time course represents an average of seven technical replicates. Smooth lines result from global fitting to a one-step binding model (Table 2).

(**D**) Binding of PDF to 70S ribosomes monitored by fluorescence anisotropy of PDF(C-term) (200 nM). A hyperbolic function was fitted to the data.

In order to determine the kinetic mechanism in addition to identifying the slow step, we monitored PDF binding to formylated TolB75-RNC using fluorescence-based stopped-flow experiments (Figure 19B). Binding was rapid (40 ± 3 s^{-1}) and indistinguishable from binding to vacant 70S ribosomes (44 ± 2 s^{-1}) (Figure 19B) at 10°C, again indicating that association of PDF with the RNC is dominated by interactions with the ribosome, rather than with the nascent chain. This allowed us to use vacant 70S ribosomes to determine rate constants for PDF binding and dissociation, which are likely representative for PDF recruitment to the RNCs as well as RNC titrations in a comparable concentration range are not feasible. The use of 70S ribosomes also simplifies the kinetic mechanism, since there is no nascent chain present to be deformylated, and the system reaches equilibrium after PDF binding.

To determine rate constants of ribosome-PDF complex formation, PDF(C-term) was rapidly mixed with 70S ribosomes at increasing concentrations in the stopped-flow apparatus at 10°C. The Bpy fluorescence changes accompanying complex formation (Figure 19C) were globally fitted using the KinTek Explorer software (Johnson et al., 2009a, b) according to a one-step binding model. This fitting yielded a binding rate constant k_1 of 14 ± 2 $\mu M^{-1}s^{-1}$ and a reverse rate constant k_{-1} of 29 ± 2 s^{-1}; the latter is the same as determined in chase experiments (Figure 19A). The K_d for this interaction was determined independently by equilibrium titration while monitoring changes in fluorescence anisotropy of PDF(C-term) upon addition of 70S ribosomes (Figure 19D). The measured K_d of 2.1 ± 0.2 µM is in agreement with the value determined from kinetic constants ($K_d = k_{-1}/k_1 = 2.1 \pm 0.4$ µM) and with values reported in previous studies: 1.5 µM (25°C) (Bornemann et al., 2014), 1.8 ± 0.9 µM (12°C) (Bingel-Erlenmeyer et al., 2008) or 2.6 µM (10°C) (Sandikci et al., 2013). To facilitate comparison with deformylation rates, rate constants k_1 and k_{-1} measured at 10°C were extrapolated to 37°C using a previously established method (Rudorf et al., 2014), which allows calculation of rate constants using a correction factor obtained from temperature dependence of a key step on the pathway. As a reference reaction, we used single-round deformylation with a rate of 24 ± 3 s^{-1} at 10°C compared to 60 ± 20 s^{-1} at 37°C (Figure 20). From these values, the extrapolated rate constants were 40 ± 20 $\mu M^{-1}s^{-1}$ for binding and 70 ± 30 s^{-1} for dissociation (Table 2), which are 100-fold larger than the reported k_{cat} values and, therefore, not rate-limiting.

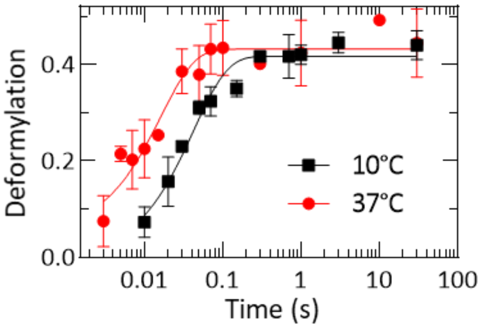

Figure 20. Temperature dependence of single-turnover deformylation kinetics. TolB75-RNC (10 nM) was mixed with PDF (25 µM) at 10°C and 37°C. Single-exponential fitting yields k_{TolB75} (10°C) = (24 ± 3) s^{-1} and k_{TolB75} (37°C) = (60 ± 20) s^{-1}. Error margins represent the standard deviation of three independent experiments.

Table 2. Kinetic parameters of PDF binding to 70S ribosomes. Rates measured at 10°C were extrapolated to 37°C and $K_{d,kinetic}$ values were calculated from rate constants (Methods). $K_{d,anisotropy}$ was measured by 70S ribosomes titration at 10°C (Figure 19D).

	10 °C	37 °C
k_1 ($\mu M^{-1}s^{-1}$)	14 ± 2	40 ± 20
k_{-1} (s^{-1})	29 ± 2	70 ± 30
$K_{d,kinetic}$ (µM)	2.1 ± 0.4	2 ± 1
$K_{d,anisotropy}$ (µM)	2.1 ± 0.2	n.d.

2.1.3 Reversibility of deformylation

We noted that in all of our deformylation experiments, the end levels were consistently around 50% in multiple-turnover experiments, regardless of the RNC concentration (Figures 17B and 21A) and in agreement with previous studies (Ranjan et al., 2017; Yang et al., 2019). The 50% end level was not due to loss of enzyme activity, because addition of new RNC to a multiple-turnover deformylation reaction that had already reached a plateau resulted in the appearance of more deformylated product (Figure 21B). Also, the RNCs are more than 50% functional, as indicated by the end levels of reactions at high PDF concentrations, which reached 80-90% for different RNCs (Figure 21C). One possibility to explain the 50% reaction endpoint is that hydrolysis is reversible, and thus the end level is defined by the equilibrium between forward deformylation and backward reformylation. To test this hypothesis directly, we added product to a completed deformylation reaction, which would drive a reversible reaction in the opposite direction, causing reformylation. We achieved this by addition of formate to generate small amounts of formic acid, a product of deformylation, while maintaining a constant pH, in accordance with the Henderson-Hasselbalch equation. While high formic acid concentrations are unlikely to emerge *in vivo*, this approach allowed us to implement a standard approach for investigation of reversibility in steady-state enzyme kinetics. The internal equilibrium of reversible deformylation would be an inherent property of the enzyme, reducing the net k_{cat} value by extending the delay prior to PDF turnover. The test was carried out under multiple-turnover conditions, where deformylation of TolB75-RNC was performed until the end level was reached (Figure 21D, “No addition”) and then formate, a deformylation product, was added. This caused the expected reduction of deformylated product, indicating that deformylated RNC was partly reformylated, as expected for a reversible reaction. In the presence of actinonin, a competitive PDF inhibitor (Chen et al., 2000), the effect of formate is reduced substantially, indicating that reformylation is catalyzed by PDF. The observed residual reformylation can be explained by the slow binding kinetics of actinonin so that PDF can rapidly reformylate a limited number of RNCs before it is inhibited when actinonin and formate are added at the same time (Van Aller et al., 2005). In the case of actinonin being incubated with PDF before addition of RNCs (Figure 21E), PDF is efficiently inhibited. The high concentration of 2 mM actinonin was chosen to ensure complete inhibition of PDF even though the IC_{50} value at the experimental conditions was 1.9 ± 0.4 µM (Figure 21F). Compared to the reported K_i value of dipeptide inhibition in the low nM range (Chen et al., 2000), this is a relatively high value, but it is only 2-fold higher than the used enzyme concentration of 1 µM. Additionally, RNCs showed a much lower K_M value compared to dipeptides which increases the expected K_i. For comparison, the addition of buffer or acetate did not lead to a decrease of the deformylated product (Figure 21D). Thus, peptide deformylation by PDF on the ribosome is reversible.

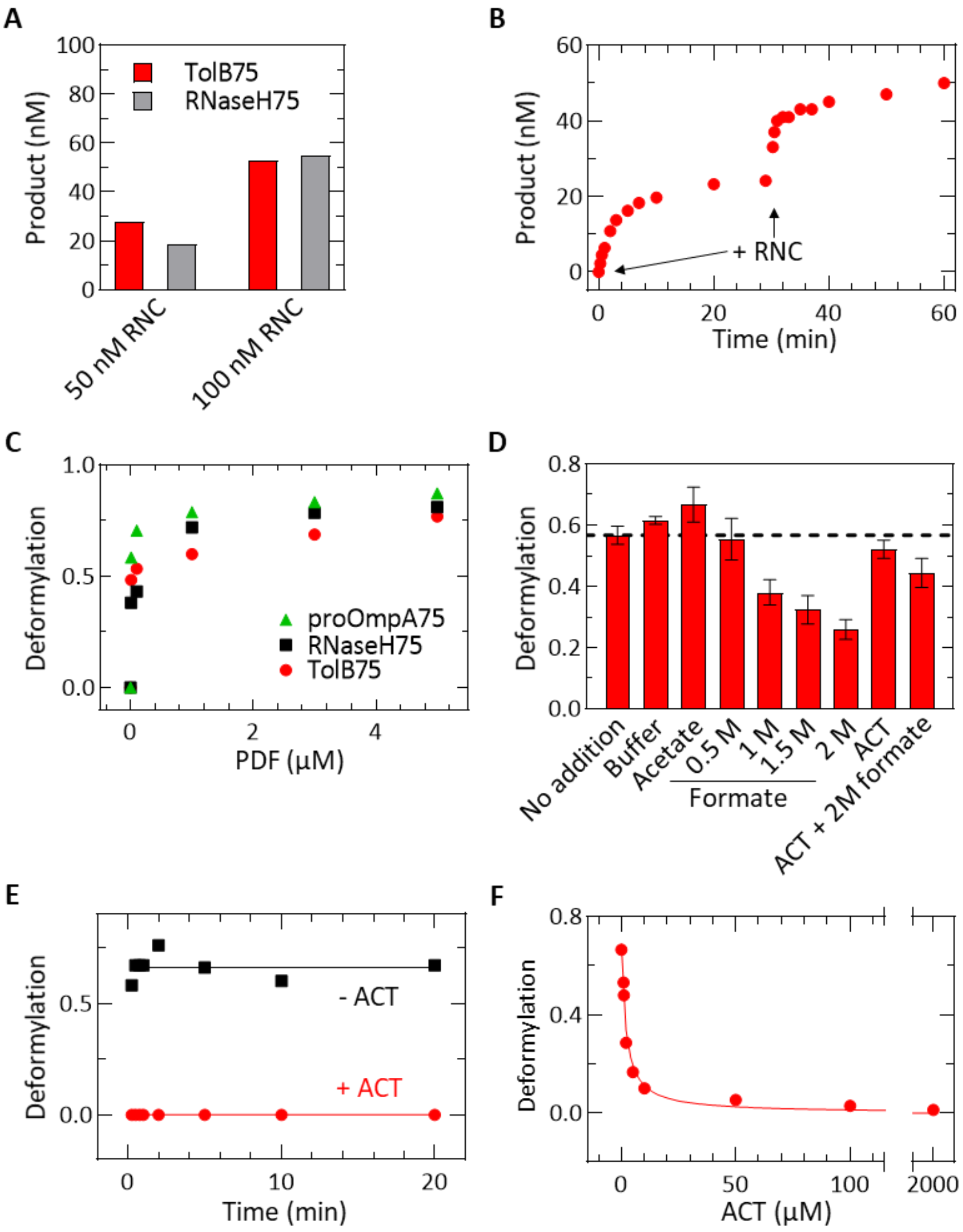

Figure 21. Reversal of deformylation. Legend continued on p. 35.

Figure 21. Continued from p. 34.

(**A**) End level of deformylation at different RNC concentrations. TolB75-RNC and RNaseH75-RNC were incubated with PDF (10 nM) for 20 min at 37°C.

(**B**) PDF activity. Substrate (50 nM TolB75-RNC) was added to PDF (10 nM) at the start of the reaction, and again after 30 min (arrows).

(**C**) RNC reactivity. End levels of deformylation time courses for proOmpA75-RNC, RNaseH75-RNC and TolB75-RNC (50 nM each) after 30 min at different PDF concentrations.

(**D**) Reversibility. After incubation of TolB75-RNC (50 nM) with PDF (1 µM) for 10 min ('No addition'), additions were made as indicated. The PDF inhibitor actinonin (ACT; 2 mM) was included where indicated. Deformylation levels measured after 30 min further incubation are depicted. Error margins represent the standard deviation of three independent experiments.

(**E**) Inhibition by ACT. TolB75-RNC (50 nM) was reacted with PDF (1 µM) without and with ACT (2 mM).

(**F**) ACT titration. Increasing concentrations of ACT were added to a reaction of TolB75-RNC (50 nM) and PDF (1 µM). The reaction was quenched after 1 min.

2.1.4 Kinetic mechanism of deformylation

Next, we used the combined data to describe a minimal kinetic mechanism of RNC deformylation by PDF and explain the slow multiple-turnover behavior (Figure 22). In the simplest model, PDF binding to and dissociation from the ribosome can be described as a rapid one-step process (Figure 19). The following chemistry step is reversible (Figure 21) and much faster than the slow turnover of PDF measured at multiple-turnover conditions (Figures 17 and 18), indicating the existence of an additional slow step after deformylation but prior to dissociation of PDF, which is also rapid (Figure 19A). Finally, reversible formate dissociation from PDF is considered as a separate reaction, as proposed by mechanistic studies on model peptides (Becker et al., 1998). We note that this minimal model does not take into account a potential step at which the nascent peptide is recruited to PDF before deformylation. This step must be fast, because the following deformylation step is rapid and not rate-limiting, but it may contribute to the stabilization of PDF on RNC, which is not captured in our model.

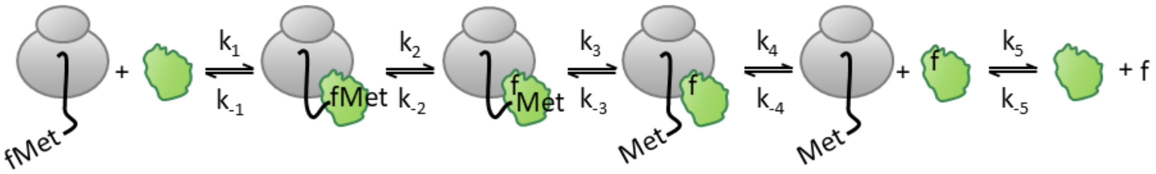

Figure 22. Minimal kinetic model of deformylation. Binding of formylated RNC (gray) and PDF (green) is followed by deformylation. After a slow conformational rearrangement, PDF dissociates from the deformylated RNC and finally, formic acid dissociates from the enzyme. All reactions are reversible with forward and reverse rate constants as indicated. f represents the formyl group.

We further estimated the rate constants of individual steps based on the available kinetic information (Table 3). To describe the kinetics of enzyme binding and dissociation, we used the values for rate constants k_1 and k_{-1} determined from binding and dissociation experiments carried out at 10°C (Figure 19), and extrapolated them to 37°C (Table 2). Since PDF binding and dissociation were indistinguishable for ribosomes and RNCs, we apply the same values of k_1 and k_{-1} for all RNCs and, furthermore, we infer the same rate constants for PDF interaction with ribosomes after deformylation (i.e. $k_4 = k_{-1}$, $k_{-4} = k_1$). The forward and reverse rate constants of deformylation, k_2 and k_{-2}, were determined from the apparent rates and end levels of deformylation at single turnover conditions, where one can assume that the following reactions do not contribute significantly (Methods). To estimate deformylation rate constants for the four different RNCs, we used the average apparent rate of deformylation of about 50 s^{-1} for all constructs, and took into account the slightly different end levels for each RNC. For TolB75 and DnaK75, these values were taken from Figure 18B, while end levels for RNaseH75-RNC (80%) and proOmpA75-RNC (88%) were determined in PDF titration experiments (Figure 21C). The resulting forward rate constants k_2 were statistically indistinguishable for the four substrates, on average 40 s^{-1} and calculation of the reverse rate constants k_{-2} yielded values of 5-11 s^{-1} depending on the RNC (Table 3). These values provide reasonable estimates for deformylation rate constants based on the single-turnover reaction alone and with the implicit assumption that the following step is slow compared to single-round deformylation. This assumption is clearly supported by comparison of the single- and multiple-round turnover rates. Values of k_2 and k_{-2} were therefore fixed in the subsequent global fitting. In order to test the robustness of the fit, we also fitted the k_{-2} values together with all other free parameters and found that the values did not change, but rather increased the uncertainty of the fit due to interdependence between rate constants.

The remaining rate constants (k_3, k_{-3}, k_5, k_{-5}) could not be determined analytically. To provide values for these rate constants and assess the feasibility of the proposed kinetic mechanism, we carried out global fitting using the model in Figure 22, multiple-turnover and single-turnover experiments for all substrates, and formate-driven formylation of TolB75-RNC, all performed at 37°C. Initial fits with all undetermined parameters free to change were poorly defined due to the completely reversible reaction and high interdependence of rate constants in the fit. In particular, global fitting indicated that formate dissociation from PDF must be fast, although the value could not be determined with precision. As this is clearly not a ribosome-dependent rate-limiting step, we fixed the respective rate constant to 200 s^{-1} in subsequent fitting. Reverse rates k_{-5} were then linked (i.e. considered to be identical) for different substrates, because formate binding to PDF is not expected to differ in the presence of different RNCs. With these constraints, we obtained good quality fits for all data sets (Figure 23) and defined values for all rate constants, although the high interdependence between rate constants k_3, k_{-3} and k_{-5} resulted in rather large error margins (Table 3).

The fitting provides estimates for the rate-limiting step of PDF turnover, which has a low forward rate (k_3) and is readily reversible (k_{-3}). This step is about five-fold faster for RNaseH75 than it is for TolB75 and DnaK75 (Table 3), which reflects the trend observed in k_{cat} values measured for these substrates (Table 1). The values for k_3 are 2-5 times larger than the respective k_{cat} values due to the reversibility of the deformylation step, with the large values of k_{-3} decreasing the net rate in the direction of deformylated RNCs. Overall, the results of global fitting are consistent with the minimal kinetic model and the presence of a rate-limiting rearrangement after deformylation.

Table 3. Overview of rate constants obtained by global fitting. Errors represent standard errors from global fit analysis or error margins determined from experiments (†).

	TolB75	DnaK75	RNaseH75	proOmpA75
k_1 ($\mu M^{-1}s^{-1}$) †	40 ± 20			
k_{-1} (s^{-1}) †	70 ± 30			
k_2 (s^{-1}) †	40 ± 5			
k_{-2} (s^{-1}) †	11 ± 4	5 ± 2	10 ± 3	6 ± 2
k_3 (s^{-1})	0.15 ± 0.04	0.09 ± 0.02	0.5 ± 0.06	ND
k_{-3} (s^{-1})	50 ± 20	22 ± 8	40 ± 10	ND
k_4 (s^{-1}) †	70 ± 30			
k_{-4} ($\mu M^{-1}s^{-1}$) †	40 ± 20			
k_5 (s^{-1})†	200			
k_{-5} ($\mu M^{-1}s^{-1}$)*	200 ± 20			

† Value fixed for fitting.
*Value shared between all RNCs.

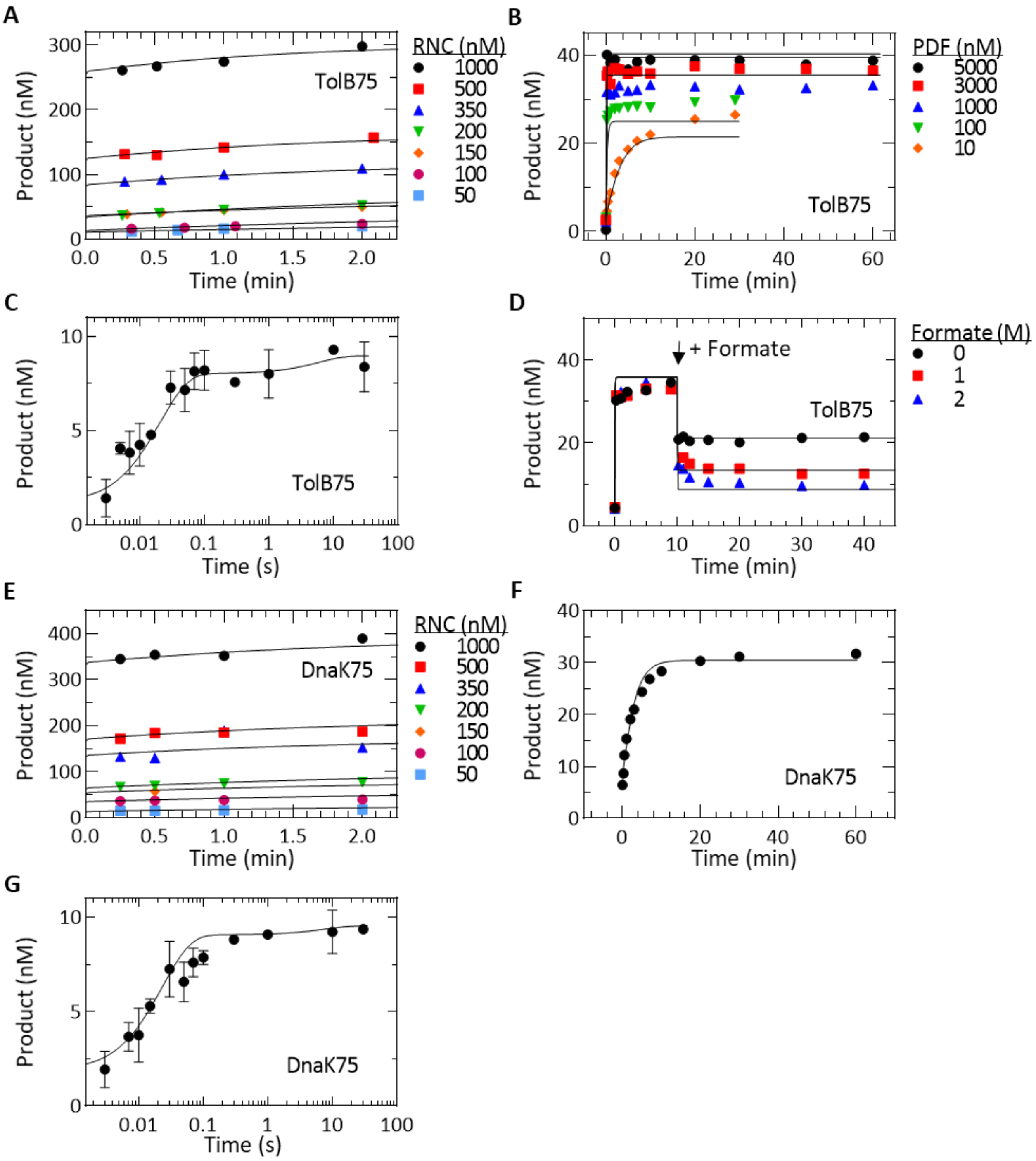

Figure 23. Global fit. All deformylation data of TolB75-RNC, DnaK75-RNC, RNaseH75-RNC and proOmpA75-RNC were used for global fitting in KinTek Explorer (Methods). Figure is continued on p. 39.

TolB75-RNC: (**A**) Multiple-turnover kinetics; (**B**) PDF titration; (**C**) Single-turnover kinetics; (**D**) Deformylation with addition of formate.

DnaK75-RNC: (**E**) Multiple-turnover kinetics; (**F**) Extended time course with PDF (10 nM) and RNC (50 nM); (**G**) Single-turnover kinetics. Error margins in (**C**,**G**) are standard deviations of independent experiments (TolB75: n=3; DnaK75: n = 4).

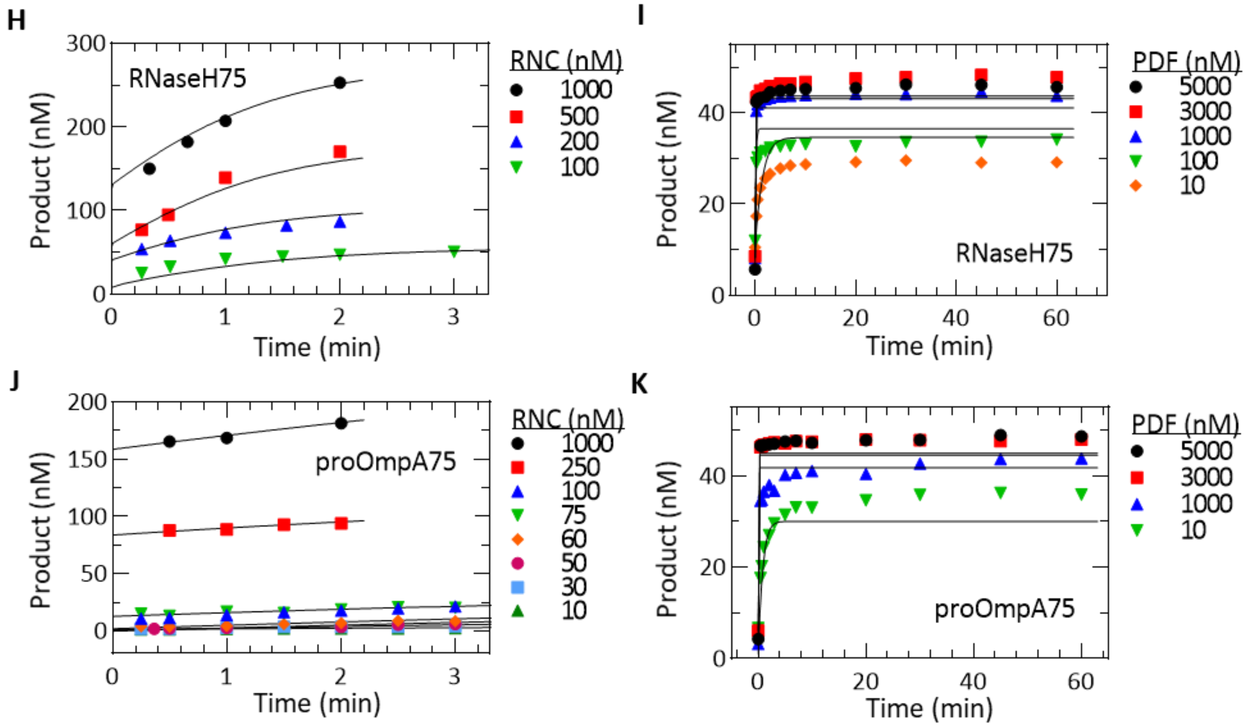

Figure 23. Continued from p. 38.
RNaseH75-RNC: (**H**) Multiple-turnover kinetics; (**I**) PDF titration.
proOmpA75-RNC: (**J**) Multiple-turnover kinetics; (**K**) PDF titration.
Solid lines depict the simulated concentrations based on the global fitting results (Figure 22, Table 3).

2.1.5 The nascent chain is deformylated upon emergence from the ribosome

Since deformylation in the cell occurs co-translationally, we also examined whether active translation influences deformylation kinetics. We translated TolB mRNA encoding 50, 75, or 100 N-terminal amino acids in the presence of PDF (Figure 24A) and followed nascent chain deformylation concomitantly with protein synthesis after confirming that the addition of PDF does not alter translation kinetics (Figure 24B). At cellular PDF concentration (2 µM (Ragusa et al., 1998)), co-translational deformylation is extremely rapid on about 40% of RNCs (green triangles in Figure 24C), which are deformylated as soon as they reach the expected length of 50 aa (black triangles in Figure 24A, C). The end level of this rapid deformylation reaction is independent of the final nascent chain length, suggesting that the action of PDF in this phase is only limited by the emergence of the nascent chain from the exit tunnel. An additional 25% of RNCs are deformylated more slowly, and the rate of deformylation is somewhat lower for TolB50- than for TolB75- and TolB100-RNC, consistent with previous studies that indicated a length-dependent deformylation for purified RNCs at multiple-turnover conditions (Ranjan et al., 2017; Yang et al., 2019). While rapidly deformylated RNCs result from single-round PDF action, it is likely that the slower phase of deformylation is determined by PDF turnover, as observed on purified RNCs. By analogy with RNCs, the rate-limiting step of the multiple-turnover reaction is likely a rearrangement of the PDF-RNC complex after deformylation but before PDF release.

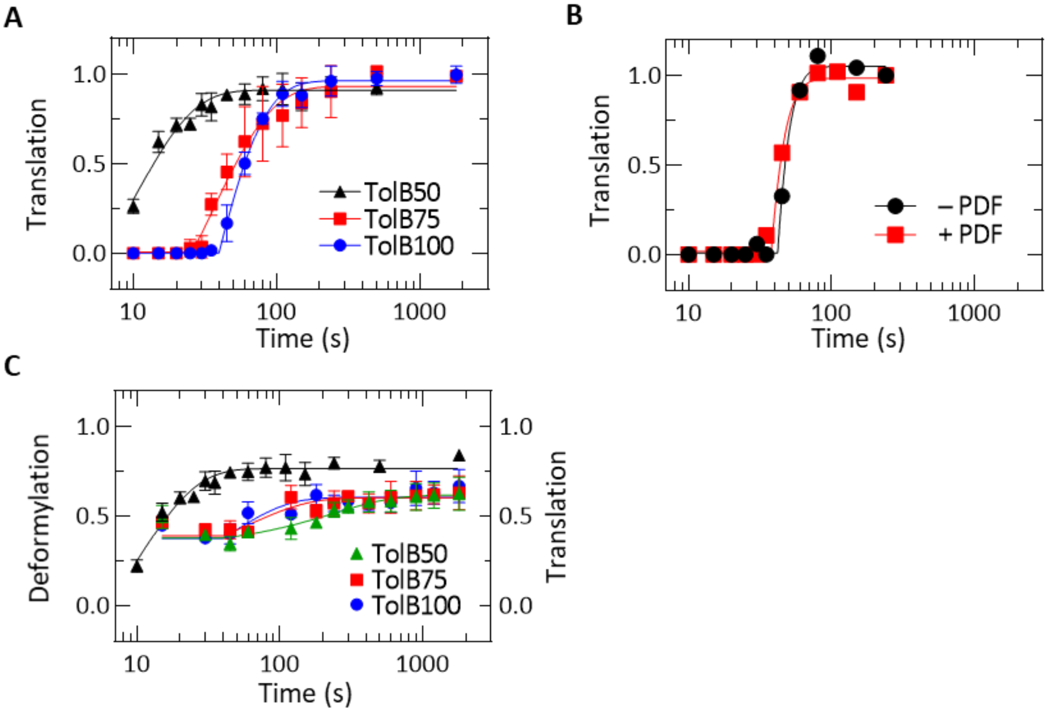

Figure 24. Co-translational deformylation of RNCs.

(**A**) Translation time courses of TolB50, 75 and 100.

(**B**) Influence of PDF on translation. Translation of TolB100 initiation complex (25 nM) in the presence or absence of PDF (2 µM).

(**C**) Co-translational deformylation. Translation of TolB mRNA constructs of increasing length (50, 75, and 100 codons) was started with initiation complex (50 nM) by adding the components of the translation system and PDF (2 µM). Deformylation (colored symbols) is plotted on the left Y-axis, and translation of TolB50 mRNA (black triangles) on the right Y-axis. Co-translational deformylation time courses were described by a delay-exponential function with one exponential term and the rates of the multiple turnover phase were 0.004 ± 0.002 s^{-1} (TolB50), 0.017 ± 0.01 s^{-1} (TolB75), and 0.024 ± 0.014 s^{-1} (TolB100). Error bars represent the standard deviation of three independent experiments.

2.2 Biological evaluation of fumimycin and analogues as peptide deformylase inhibitors

Fumimycin (1) was shown to be a moderate inhibitor of *Staphylococcus aureus* PDF (*Sa*PDF) (Kwon et al., 2007). To test its inhibitory properties on *Escherichia coli* PDF (*Ec*PDF), the dipeptide deformylation assay with fML-pNA as substrate was applied and as reference, the rate of deformylation was measured in the absence of any inhibitor. Then fumimycin was added to the reaction in a concentration of 4 µM (Figure 25A) which is the IC_{50} value determined for inhibition of *Sa*PDF (Kwon et al., 2007). A reduction in the initial velocity of 17% was observed which indicates that the inhibition of *Ec*PDF is less efficient than the inhibition of *Sa*PDF. Furthermore, synthetic fumimycin analogues (Figure 25B) (Zaghouani et al., 2019) were added to the deformylation assay for biological evaluation as PDF inhibitors (Figure 25A) and the well-established PDF inhibitor actinonin (2) was included in the assay for comparison. Overall, neither fumimycin nor any of the analogues shows a large inhibitory effect, only actinonin demonstrates strong inhibition. The smaller differences, however, provide some insights in their biological activity. The allylic side chain of the styrene moiety appears to be important for the stabilization of the compounds in the S1' cavity as it is present in most of the more strongly inhibiting analogues. Fumimycin contains two potential metal binding sites, the carboxyl group and the catechol moiety, while other inhibitors like actinonin possess a hydroxamate that creates a potent metal binding site (Apfel et al., 2000; Chen et al., 2000). Therefore, fumimycin analogues with hydroxamate, carboxylate or catechol groups were tested. Three of the six most active compounds contain a catechol moiety (1, 1o, 1k) whereas most hydroxamate derivatives do not show a significant reduction of PDF activity. This indicates that either binding of the hydroxamate to the metal ion is sterically not favored or that catechol binding is stabilized by additional interactions. In the absence of a catechol group, however, the hydroxamate (1n) appears to facilitate PDF inhibition slightly better than the carboxylate (1h).

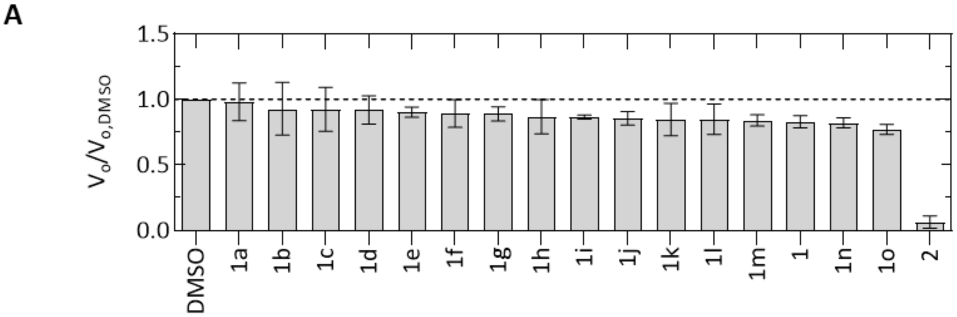

	1a	1b	1c	1d	1e	1f	1g	1h	1i	1j	1k	1l	1m	1	1n	1o
Hydroxamate	+	+	+	+	-	-	-	-	+	-	-	-	-	-	+	-
Carboxylate	-	-	-	-	-	-	-	+	-	-	-	-	-	+	-	-
Catechol	-	-	-	-	-	-	+	-	-	-	+	-	-	+	-	+
Allyl	-	-	-	-	+	-	+	+	-	+	+	+	+	+	+	-

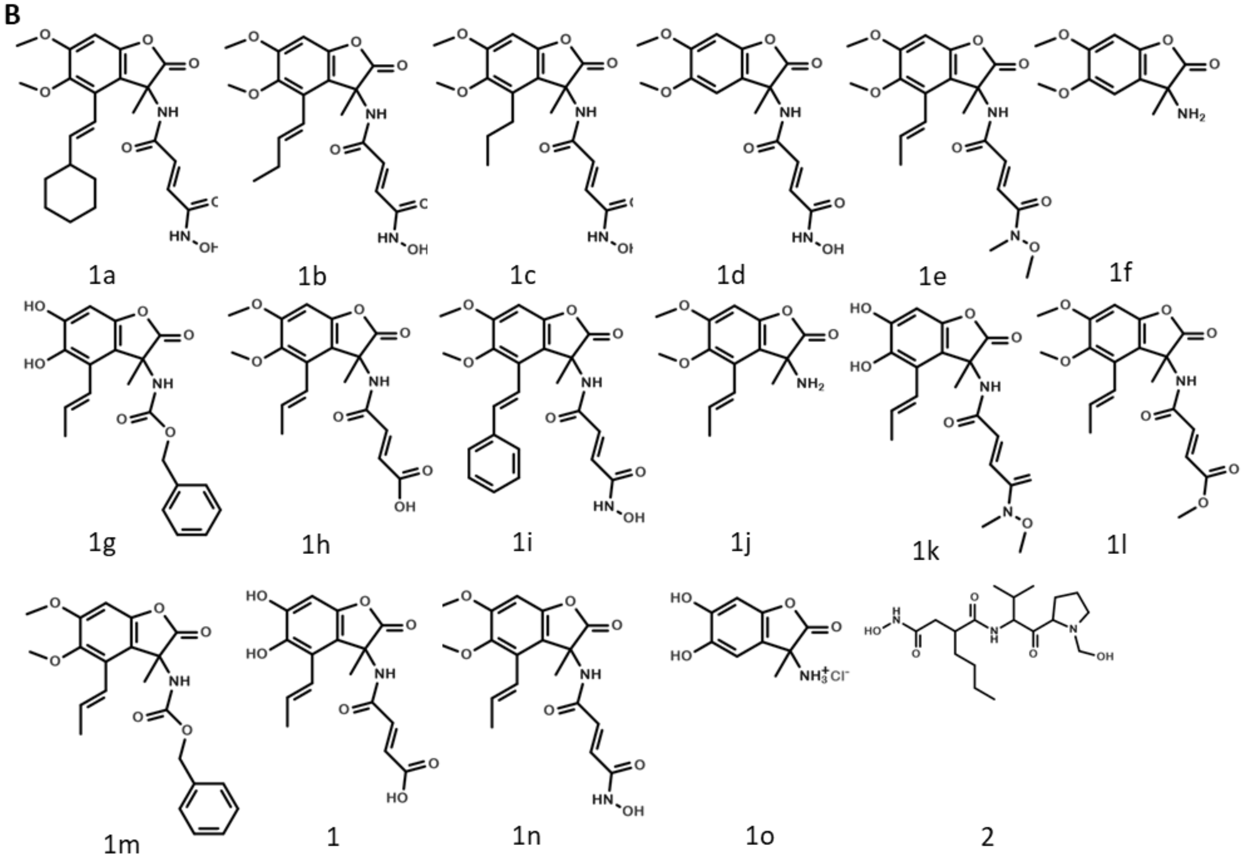

Figure 25. PDF inhibition by fumimycin analogues.

(**A**) PDF inhibitor screen. fML-pNA was deformylated by PDF in the presence of potential PDF inhibitors. The initial velocity of deformylation, V_0, was standardized relative to the initial velocity of the DMSO-only control. Error bars represent standard deviation (n = 3).

(**B**) Chemical structures of fumimycin (1) and its analogues (1a-1o), as well as actinonin (2).

2.3 Co-translational folding of the membrane protein EmrD

To analyze folding of the N-terminal half of the alpha helical membrane protein EmrD, rapid kinetics methods using FRET reporters were applied. EmrD was synthesized on ribosomes that were bound to translocons embedded in nanodiscs so that the nascent membrane protein was co-translationally inserted into the phospholipid bilayer. In order to monitor this process in real time, the nascent protein and, where appropriate, the translocon were labeled with fluorophores (Figure 26). The FRET donor Bpy was attached to the N-terminus of EmrD to mark the position of TM1 or it was incorporated into the nascent chain at the end of TM2. The fluorophores Atto647N and Atto655 were employed as FRET acceptors and were positioned either on the translocon or on the N-terminus of EmrD. FRET is a non-radiative transmission of energy from the FRET donor to the FRET acceptor which is dependent on the distance r between the two fluorophores (Lakowicz, 2006). As the FRET efficiency increases with r^{-6} the closer the fluorescence reporters are to each other, the distance between two fluorophores can be estimated by determining the amount of acceptor fluorescence when only the donor is excited. By following the changes in the distance between different FRET pairs during translation, the co-translational movements of TM1 and TM2 can be monitored which allows description of the first steps in co-translation folding of EmrD.

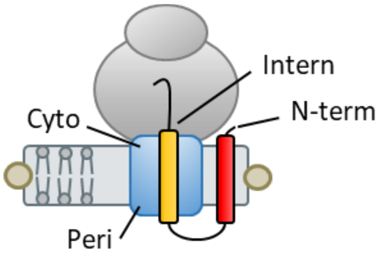

Figure 26. Schematic of labeling positions. The ribosome (gray) carries a nascent chain with multiple TMs (red and yellow) that have been inserted into a nanodisc comprising the translocon (blue), lipid bilayer (gray) and the scaffold protein (brown). Potential labeling positions for fluorophores are on the N-terminus (N-term), at the end of TM2 (intern) and on the cytoplasmic (cyto) or periplasmic (peri) side of the translocon.

2.3.1 Efficient translation of Bpy-labeled EmrD

To monitor approach and insertion of TM1 and TM2 into the translocon and the phospholipid bilayer, the translation of EmrD on the ribosome is established. We produced ribosome complexes carrying N-terminal EmrD nascent peptides ranging from 50 to 200 aa in length, which allows us to sample different stages of the insertion process (Figure 27A). Initiation complexes were formed with mRNAs of the respective length using Met-tRNA^{fMet} that carries a Bpy label on the amino group of methionine (Bpy-Met-tRNA^{fMet}). Translation was started by addition of elongation factors and purified aa-tRNA at conditions that were optimized for the nascent chain length of 135 aa and then used for all other constructs. N-terminally labeled peptide chains (EmrD(N-term)) were visualized by TRIS-Tricine-SDS-PAGE (Figure 27B). The upper band represents the full-length product while lower bands indicate accumulation of shorter, stalled nascent chain intermediates. The predominant product in most translation reactions is the respective full-length product, which demonstrates the efficiency of the translation assay and the homogeneity of the resulting RNC preparations. When translation was performed in the presence of radioactively labeled [^{14}C]Leu-tRNA^{Leu}, radioactive counting of purified RNCs revealed translation efficiencies between 40% and 75% relative to the IC amounts. To measure the rate of translation, aliquots were taken from the translation reaction at defined time points and the amount of full-length product was determined by quantification of TRIS-Tricine-SDS-PAGE (Figure 27C). Time courses show a delay of 10-40 s which represents the time necessary for the synthesis of the first full-length product followed by a single-exponential increase in the product amount. From this time dependence, the apparent rate of translation is calculated, which was 2-3 s^{-1}, with the highest rate for EmrD100 and EmrD135 peptides (Figure 27D). The low average translation rate of shorted constructs is most likely explained by the delaying effect of a translational pause, which was reported to result in accumulation of ribosomes at amino acid 48 (Mercier et al., 2020; Mohammad et al., 2016). With increasing number of amino acids that are added after the pause, the average translation rate increases, because the subsequent sequence is translated rapidly and without any pauses. The decrease in the apparent translation rate after 135 aa may suggest that an additional pause takes places between amino acids 135 and 175. Indeed, ribosome profiling data reveal a pause site at codon 137 of EmrD (Mohammad et al., 2016). Thus, the average translation rate is dependent on the relative position and the strength of translational pauses.

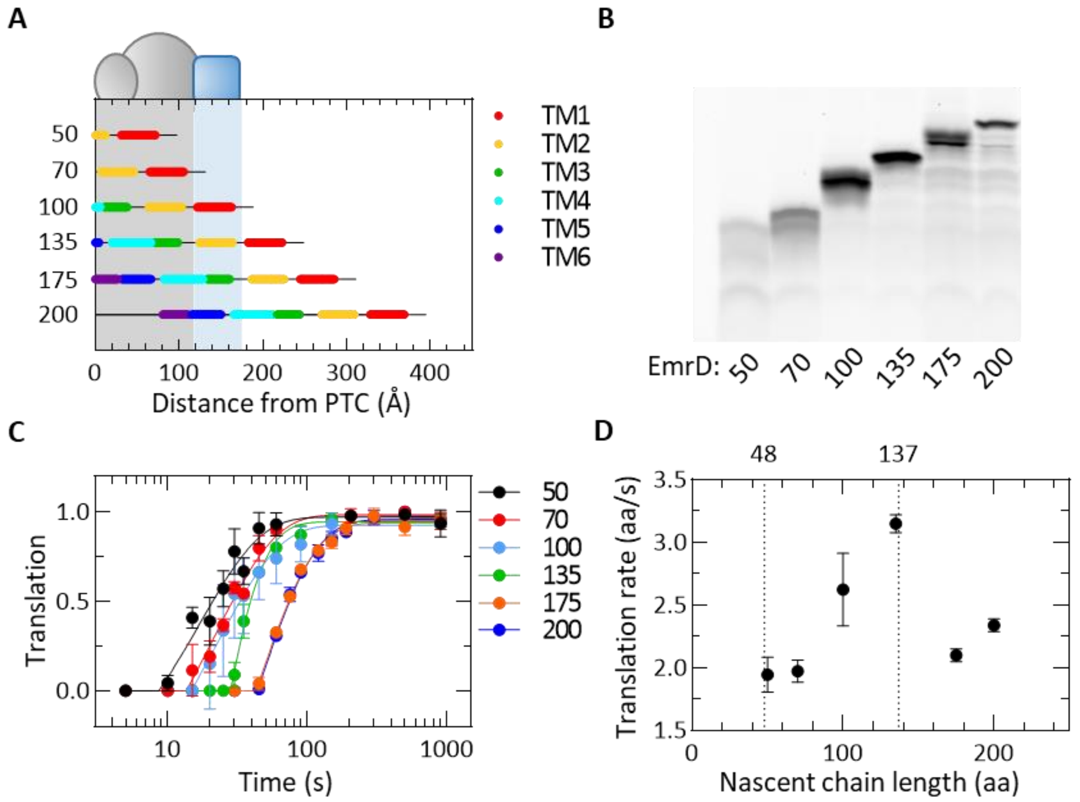

Figure 27. Translation of EmrD.

(**A**) Length of EmrD50-200 relative to the ribosome exit tunnel (gray), the translocon pore (blue) and the lipid bilayer (white).

(**B**) Translation products of EmrD(N-term)50-200 separated by TRIS-Tricine-SDS-PAGE and visualized by fluorescence.

(**C**) Translation time courses of EmrD(N-term)50-200. Data were averaged over three independent experiments and error bars indicate the standard deviations. Time courses were fitted with a delay-exponential function with one exponential term.

(**D**) Average translation rates. Translational pauses are indicated as dotted lines at 48 and 137 aa. Error margins represent standard errors determined from delay-exponential fitting.

2.3.2 Co-translational retention of N-terminus at translocon

To monitor the co-translational insertion of the N-terminal part of EmrD into the translocon and the lipid bilayer using real-time FRET changes, an acceptor fluorophore was added to one of two positions in SecY by labeling a single cysteine introduced by site-directed mutagenesis (Figure 28) (Draycheva et al., 2016; Mercier et al., 2021; Mercier et al., 2020). SecY(cyto) carries the fluorophore Atto647N (A647N) in position 179 which is on the cytoplasmic side of TM4 and in close proximity of the translocon pore. In the labeled mutant SecY(peri), the Atto647N is attached to the cysteine in position 298 which is located in a periplasmic loop adjacent to one of the helices forming the lateral gate, TM7 (Van den Berg et al., 2004).

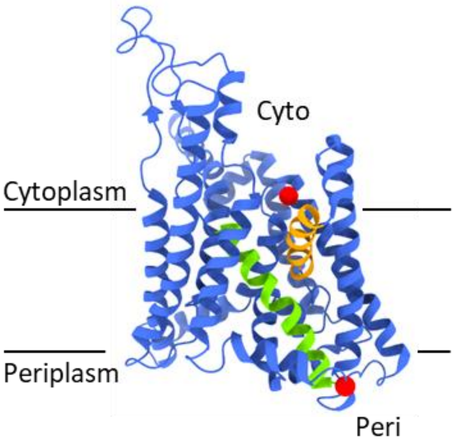

Figure 28. Positions of acceptor fluorophores A647N on SecY. Labeled amino acids in position 179 (cyto) and 298 (peri) are indicated as red spheres. TMs forming the lateral gate are highlighted in green and orange (PDB: 3J45).

To analyze the co-translational movement of TM1 relative to the cytoplasmic side of the translocon during translation, EmrD(N-term) was translated in the presence of SecY(cyto)EG nanodiscs (Figure 29A). Nanodiscs were added in a concentration that well exceeded the K_d of a ribosome-translocon complex of 10-20 nM to ensure efficient complex formation (Draycheva et al., 2016; Ge et al., 2014). When the ribosome is bound to a translocon, the growing nascent chain can directly insert into the translocon and the lipid bilayer. Using a stopped-flow apparatus, the start of translation was synchronized for all ribosomes and the fluorescence intensity of the acceptor was observed over time to monitor changes in FRET between donor and acceptor fluorophores (Mercier et al., 2020). As controls, fluorescence changes of donor only and acceptor only measurements were recorded that displayed no changes over time so that fluorescence changes in the presence of donor and acceptor arise due to FRET (Figure 30). The distance at which FRET is most sensitive is represented by the Förster radius and amounts to about 45 Å for Bpy and A647N assuming freely rotating dyes (Wu and Brand, 1994). Because this assumption is not true for the fluorescently labeled proteins used in this study and the parameter describing the rotational freedom is not readily accessible experimentally, we only report relative changes in the distance between donor and acceptor fluorophores (Kvietkauskas, 2021). FRET changes were recorded for lengths of EmrD ranging from 50 to 200 aa (Figures 29B-G) that all show a similar behavior: FRET appears after about 10 s and the subsequent FRET intensity increases in a two-phasic fashion, so that the time course can be fitted to a delay followed by a two-exponential function. When compared to the translation time courses, the fast phase occurs co-translationally while the slow phase is post-translational. Additionally, the amplitude of the slow phase is small compared to the maximal co-translational FRET change so that the post-translational phase was not considered further. When a total of 50 aa is translated, the FRET increase occurs at the same rate as translation, but the FRET efficiency is low indicating that the fluorophores are just about to come close enough to each other to undergo FRET. With EmrD70, however, the FRET change is comparable to the final FRET amplitude obtained with the longer constructs, and the FRET increase is somewhat faster than the synthesis of the 70 aa nascent chain. This suggests that the the N-terminus becomes positioned at the cytoplasmic label of the translocon at a length longer than 50 aa, but shorter than 70 aa. The largest FRET change is reached at EmrD100 which allows to estimate the average nascent chain length at which FRET increases. Based on the transition time of the fluorescence change (Figure 29H) and the average translation rate (Figure 27D), the FRET change occurs around 60 ± 7 aa. The time during which the 60 aa are translated is represented in the delay of 10 s before the start of the fluorescence change. The transition times of the co-translational FRET change are the same for all nascent chain lengths (Figure 29H) which indicates that the FRET increase occurs at the same nascent chain length independent of the total number of translated amino acids.

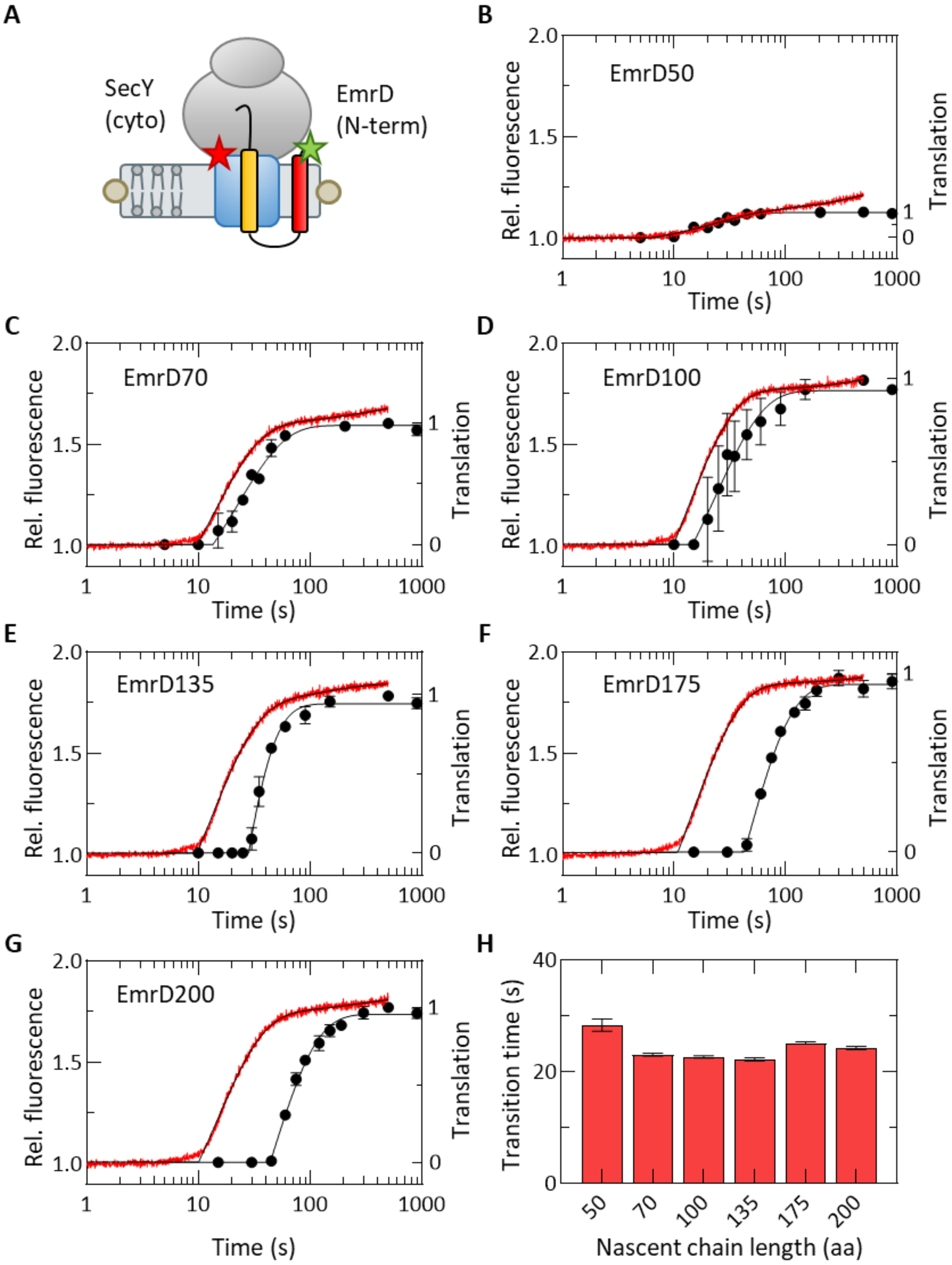

Figure 29. FRET between the N-terminus of the nascent chain and the cytoplasmic label on the translocon. The figure legend is continued on p. 49.

Figure 29. Continued from p. 48.

(**A**) Positioning of Bpy (green star) on the N-terminus of the nascent chain and A647N (red star) on the cytoplasmic side of the translocon.

(**B**)-(**G**) Co-translational FRET changes. Fluorescence changes of the FRET acceptor were monitored in a stopped-flow apparatus (left y-axis) and compared to the formation of full-length translation product (right y-axis) for EmrD50 (**B**), 70 (**C**), 100 (**D**), 135 (**E**), 175 (**F**) and 200 (**G**). Lines depict fitting with a delay-exponential function with one (translation) or two (fluorescence) exponential terms. Error bars represent the standard deviation of three independent experiments.

(**H**) Transition times obtained by delay-exponential fitting of co-translational fluorescence changes. Error bars indicate standard error of the fit.

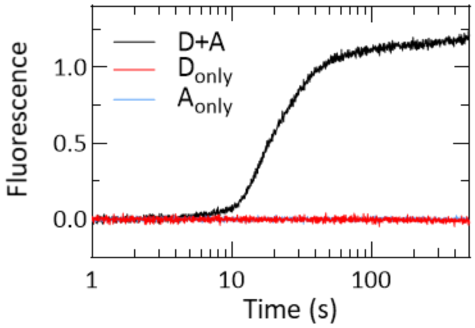

Figure 30. FRET controls. Fluorescence changes in the acceptor channel were recorded for EmrD200 translation in the presence of acceptor and donor fluorophores as well as with acceptor only and with donor only. Fluorescence change of the acceptor in the presence of the donor is due to FRET.

We also monitored the positioning of the EmrD N-terminus relative to the periplasmic side of the translocon using SecY(peri)EG (Figure 31). Similarly to the experiments with the label at the cytoplasmic side, FRET increased after a 10 s delay in a biphasic way with the fast co-translational phase followed by the slow post-translational phase. Again, the post-translational phase has a small amplitude compared to the maximal co-translational FRET change and it was not considered further. Also similar to the cytoplasmic FRET pair, the periplasmic FRET acceptor displays a fluorescence increase concomitantly with the appearance of EmrD50. The transition time of the co-translational phase is independent of the nascent chain length (Figure 31H) and comparable to the transition times obtained with the cytoplasmic acceptor label (Figure 29H). The average nascent chain length of the FRET increase was calculated for EmrD100 and amounts to 57 ± 7 aa which is the same as for the cytoplasmic label indicating that the N-terminus approaches the cytoplasmic label and does not move closer towards the periplasmic acceptor dye.

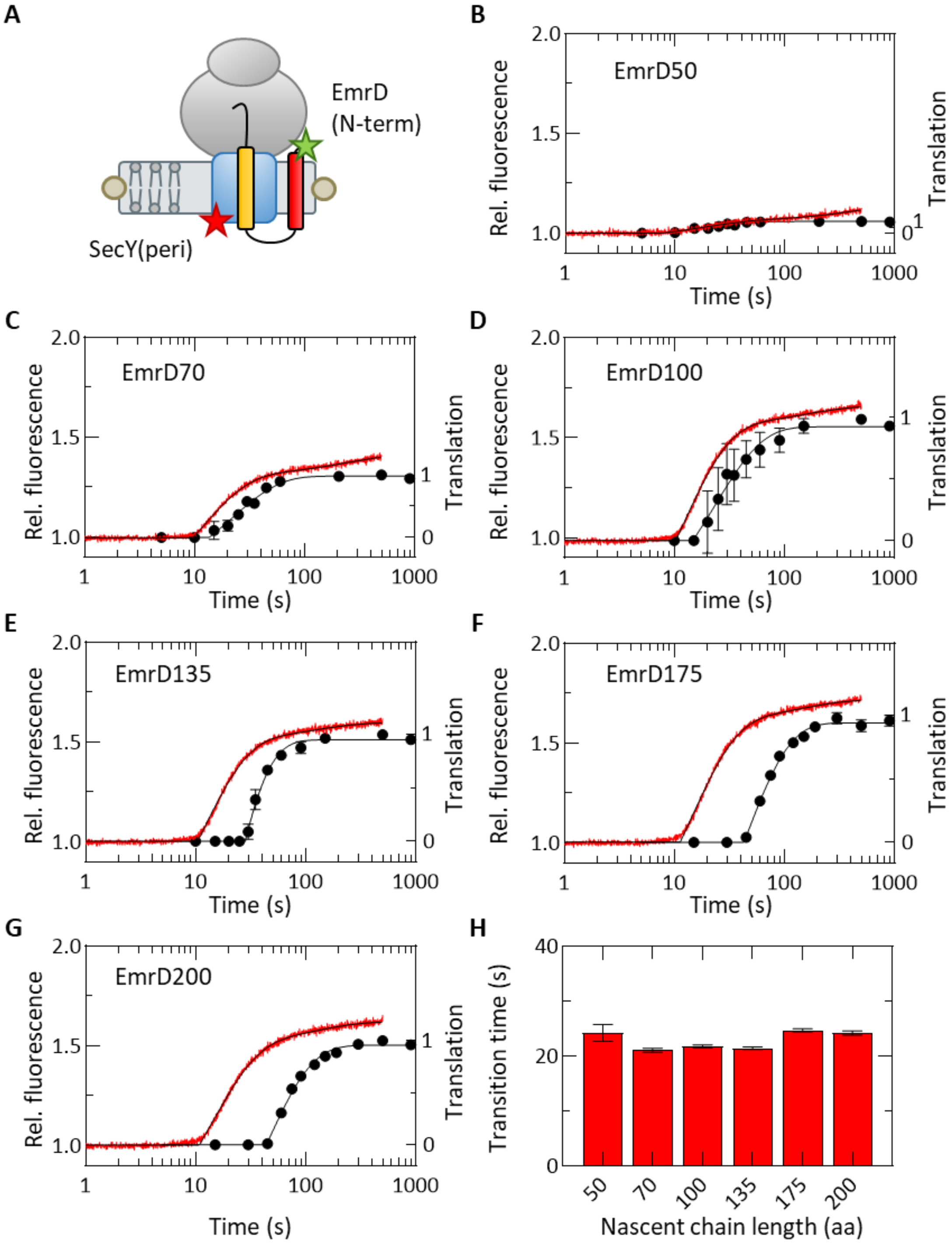

Figure 31. FRET between the EmrD N-terminus and the periplasmic label on the translocon. The legend is continued on p. 51.

Figure 31. Continued from p. 50.

(**A**) Positioning of Bpy (green star) on the N-terminus of the nascent chain and A647N (red star) on the periplasmic side of the translocon.

(**B**)-(**G**) Co-translational FRET changes. Fluorescence changes of the FRET acceptor were monitored in a stopped-flow apparatus (left y-axis) and compared to the translation time course (right y-axis) for EmrD50 (**B**), 70 (**C**), 100 (**D**), 135 (**E**), 175 (**F**) and 200 (**G**). Lines depict fitting with a delay-exponential function with one (translation) or two (fluorescence) exponential terms. Error bars represent the standard deviation of three independent experiments.

(**H**) Transition times obtained by delay-exponential fitting of co-translational fluorescence changes. Error bars indicate standard error of the fit.

To analyze the folding intermediates of EmrD during co-translational folding, the amplitudes of the fast phases of the fluorescence changes were compared (Figure 32A) which allows to determine the relative position of the N-terminus to the translocon. While the general trend of the final levels of fluorescence reached for different lengths of mRNA was similar for the two labeling positions on the translocon, the relative fluorescence for the periplasmic acceptor label is consistently lower than for the cytoplasmic. Therefore, the N-terminus remains on the cytosolic side of the membrane in agreement with the positive inside rule and previous studies (Mercier et al., 2020; von Heijne, 1992; Yin et al., 2006). The FRET efficiency between donor and acceptor fluorophores steadily increases from a length of 50 to 100 aa comparable to previous studies (Mercier et al., 2020). At 70 aa, the normalized amplitudes of the fluorescence change were significantly different (Figure 32B), indicating a larger distance of the N-terminus to the periplasmic label compared to the cytoplasmic one. Between 100 and 200 aa, the fluorescence remains roughly the same. This shows that during translation, the N-terminus of EmrD moves towards the translocon until it adopts a relatively stable position around a length of 100 aa. Afterwards, it undergoes only smaller conformational rearrangements but remains in close proximity to the translocon.

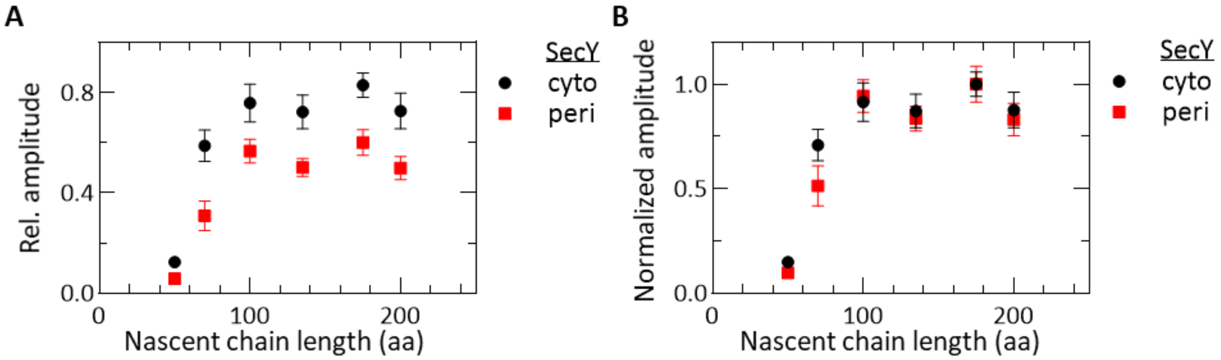

Figure 32. Fluorescence end levels.

(**A**) Amplitudes of the co-translational fluorescence change in Figures 29 and 31 were plotted for the different acceptor positions. Error bars represent the standard deviation of six technical replicates.

(**B**) Fluorescence amplitudes were normalized to the highest amplitude.

2.3.3 Efficient incorporation of an internal fluorophore after TM2

To monitor the positioning of TM2, a fluorophore needs to be incorporated into the nascent chain of EmrD around the end of TM2 via the unnatural amino acid εNH$_3$-Bpy-lysine (Bpy-Lys) (Mittelstaet et al., 2013). To ensure site-specific labeling of the nascent chain, mRNAs containing a single Lys codon were produced. For this purpose, the only lysine codon in EmrD until a length of 200 aa at position 2 was mutated to an arginine, and a single lysine codon was added near the end of TM2 in position 67 (EmrD(67K)), position 70 (EmrD(70K)), or by insertion between codons 71 and 72 (EmrD(71.5K)) (Figure 33A). The amino acids chosen to be mutated were not evolutionary conserved nor positively charged, to avoid influencing the folding pathway. To test whether the mutations by themselves influence translation, the translation rates of wild-type EmrD(N-term) and mutated EmrD(N-term/67K) were compared, which showed only minor differences (Figure 33B). Bpy-Lys was incorporated into the nascent chain co-translationally using Bpy-Lys-tRNA^{Lys} which was produced by reacting aminoacylated Lys-tRNA^{Lys} with Bpy succinimidyl ester at high pH (Holtkamp et al., 2015; Mittelstaet et al., 2013; Woolhead et al., 2004).

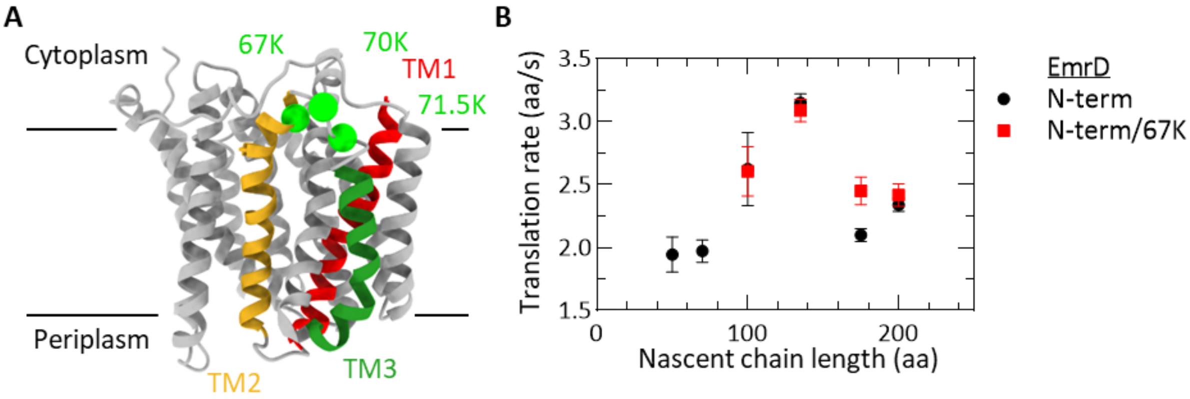

Figure 33. Incorporation of a fluorescence reporter at the internal position of the nascent chain.

(**A**) Structure of EmrD with engineered Lys residues used for fluorescence labeling indicated as spheres (green) in the loop between TM2 (yellow) and TM3 (green).

(**B**) Comparison of average translation rates of N-terminally labeled EmrD with and without Lys mutation. Error bars represent the standard error determined from delay-exponential fitting.

When fluorescence labeled Bpy-Lys-tRNA^{Lys} was added to the translation reaction instead of Lys-tRNA^{Lys}, the translation rate decreased (Figure 34A). Previous studies indicate that binding of EF-Tu to Bpy-Lys-tRNA^{Lys} is impeded compared to binding to its natural substrates (Mittelstaet et al., 2013), which prompted us to test higher concentrations of EF-Tu in the translation assay (Figures 34A, B). The concentration dependence reveals a maximum translation rate at 25 µM EF-Tu, which however does not reach the wild type translation rate. To optimize the translation conditions further, we varied the concentration of aa-tRNA (labeled and unlabeled tRNA alike) (Figure 34C) and Bpy-Lys-tRNA^{Lys} (Figure 34D). Titration of aa-tRNAs has a large effect on the translation rate which increases with aa-tRNA concentration. Concentrations of 130 µM aa-tRNA and 0.3 µM Bpy-Lys-tRNA^{Lys} were chosen because higher amounts of tRNA did not significantly change the translation rate. Concentrations of EF-G higher than 1 µM did also not alter the rate of translation so that a concentration of 2 µM was chosen (Figure 34E).

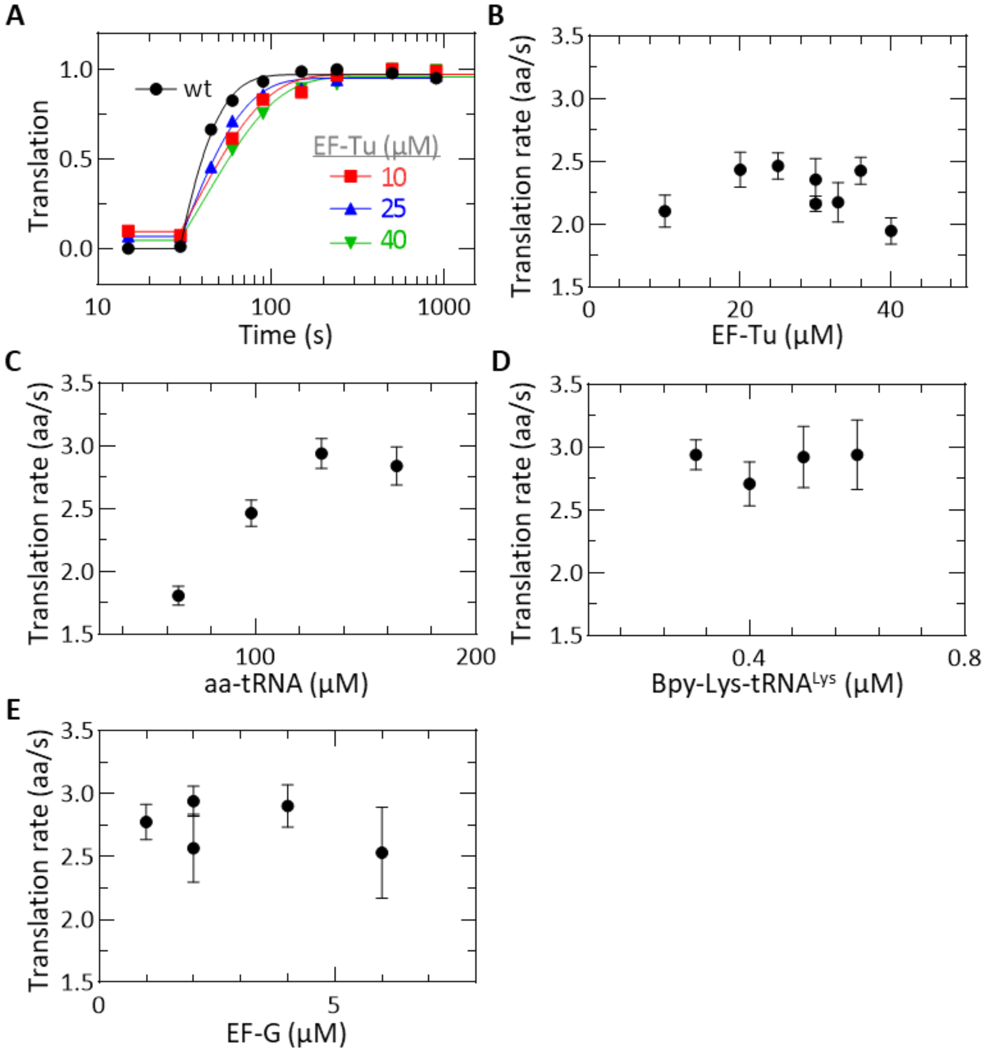

Figure 34. Optimization of Bpy-Lys incorporation.

(**A**) Translation time courses of EmrD(70K-Bpy)135 (25 nM) at different EF-Tu concentrations (10-40 µM). For comparison, a translation time course of EmrD(N-term)135 (25 nM) is shown (black symbols, 15 µM EF-Tu). Lines depict delay-exponential fits with one exponential term.

(**B**) EF-Tu titration. Average translation rates of EmrD(70K-Bpy)135 were determined in the presence of aa-tRNA (98 µM), Bpy-Lys-tRNA^{Lys} (0.3 µM), EF-G (2 µM) and increasing concentrations of EF-Tu. Error bars represent the standard error from delay-exponential fitting.

(**C**) aa-tRNA titration. Unlabeled aa-tRNA and Bpy-Lys-tRNA^{Lys} were titrated simultaneously in the presence of EF-Tu (25 µM) and EF-G (2 µM).

(**D**) Bpy-Lys-tRNA^{Lys} titration. Increasing amounts of Bpy-Lys-tRNA^{Lys} were added to a translation reaction containing EF-Tu (25 µM), aa-tRNA (130 µM) and EF-G (2 µM).

(**E**) EF-G titration. EF-G was titrated at optimized translation conditions: EF-Tu (25 µM), aa-tRNA (130 µM), Bpy-Lys-tRNA^{Lys} (0.3 µM).

To compare translation rate and efficiency of Bpy-Lys incorporation at different incorporation sites, translation time courses were recorded for the three different positions. As incorporation can potentially be more efficient after a glycine in the nascent chain (Thommen, 2015), the mRNA codon before the lysine codon in EmrD(67K) and EmrD(70K) was mutated to a glycine codon and EmrD(66G/67K-Bpy) and EmrD(69.5G/70K-Bpy) were synthesized to test for improved incorporation. In EmrD(71.5K-Bpy), a native glycine is in position 71 as defined by the wild type sequence. The intensity of the band representing the full-length product after 15 min of translation varies between the different constructs (Figure 35A). The three EmrD variants where a glycine is upstream of Bpy-Lys show the highest incorporation efficiencies of the fluorophore. EmrD(69.5G/70K-Bpy) and EmrD(71.5K-Bpy), however, display a slower rate of translation compared to the other internally labeled EmrD variants (Figure 35B), whereas EmrD(66G/67K-Bpy) shows the best incorporation efficiency and translational velocity. However, for EmrD(66G/67K-Bpy) constructs of different lengths, some translation rates were faster compared to EmrD(N-term) (Figure 35C). Because similar translation rates are necessary for direct comparison of fluorescence changes between different FRET pairs, EmrD(67K-Bpy) was chosen for further analysis. Here, translation including incorporation of the internal fluorophore showed the same rates as the synthesis of wild type EmrD(N-term) (Figure 35C). Given the chosen fluorophore position at amino acid 67, translation as well as FRET changes were analyzed starting at a final peptide length of 100 aa. Translation efficiencies determined by radioactive counting of Bpy-[^{14}C]Lys ranged between 90 and 100% and mainly the full-length product is visible on the gel (Figure 35D). Thus, translation of EmrD(67K-Bpy) which will be further referred to as EmrD(intern) will allow a direct comparison to EmrD(N-term).

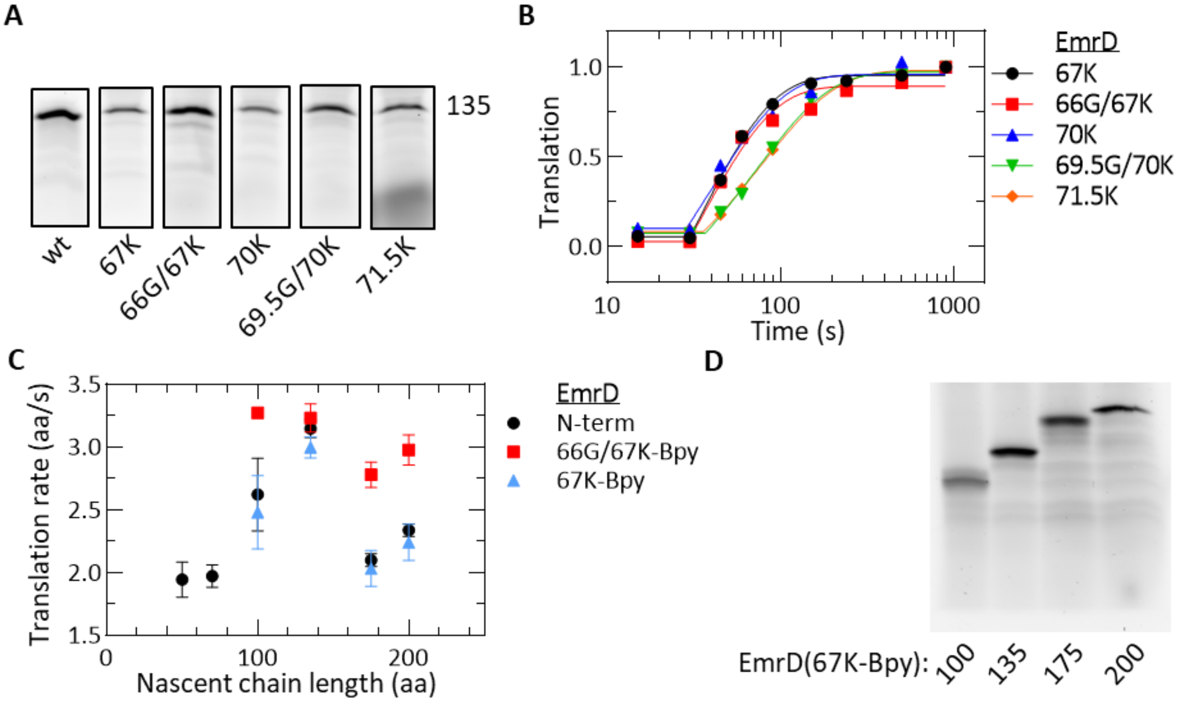

Figure 35. Comparison of Bpy-Lys incorporation sites.

(**A**) Translation products. Translation of EmrD(N-term)135 was carried out for 15 min and nascent chains were separated by TRIS-Tricine-SDS-PAGE. Analogously, co-translational incorporation of Bpy-Lys was carried out at an indicated Lys codon with or without a preceding Gly.

(**B**) Translation time courses. Translation reactions with Bpy-Lys incorporation at different positions were quenched at indicated time points and fitted to a delay-exponential function.

(**C**) Translation rates. Translation rates were recorded for different lengths of EmrD(66G/67K-Bpy) and EmrD(67K-Bpy) and compared to EmrD(N-term). Error bars show the standard error determined by delay-exponential fitting.

(**D**) Translation of EmrD(67K-Bpy)100-200 was carried out for 15 min and translation products were separated by TRIS-Tricine-SDS-PAGE. Lower bands appear at the incorporation site of Bpy-Lys at codon 67.

2.3.4 Dynamic rearrangements of TM2 during co-translational insertion

To follow the insertion of TM2 into the translocon and the lipid bilayer, we monitored FRET between EmrD(intern) and SecY(cyto) during translation of 100-200 codons (Figure 36A). As above, fluorescence changes arise due to FRET (Figure 37) and the fluorescence curves show a delay followed by a two-exponential FRET efficiency increase with a fast, co-translational phase and a slow, post-translational phase (Figures 36B-E). The co-translational FRET change of ErmD100 coincides with its translation rate (Figure 36B), which indicates that the fluorophores reach a distance suitable for FRET around this length, however, FRET efficiency is low. The 20 s long delay represents the time that is needed to translate the 66 aa until the incorporation site and roughly 30 additional amino acids to allow for FRET. In comparison, 50 aa after the fluorophore were necessary to detect FRET with EmrD(N-term). Given that the distance between FRET donor and acceptor must be similar to give the same FRET efficiency regardless where in the nascent chain the fluorophore is attached, a smaller number of amino acids after the incorporation site is needed to reach the minimal FRET distance of the cytoplasmic translocon label than at the N-terminal part of EmrD. The average nascent chain length at which the FRET increase occurs, as calculated for EmrD135, is 91 ± 3 aa which is only 30 aa later than for EmrD(N-term) even though there are 66 aa between the incorporation sites. As with the N-terminal label, the fluorescence change occurs roughly at the same time for all constructs (Figure 36F).

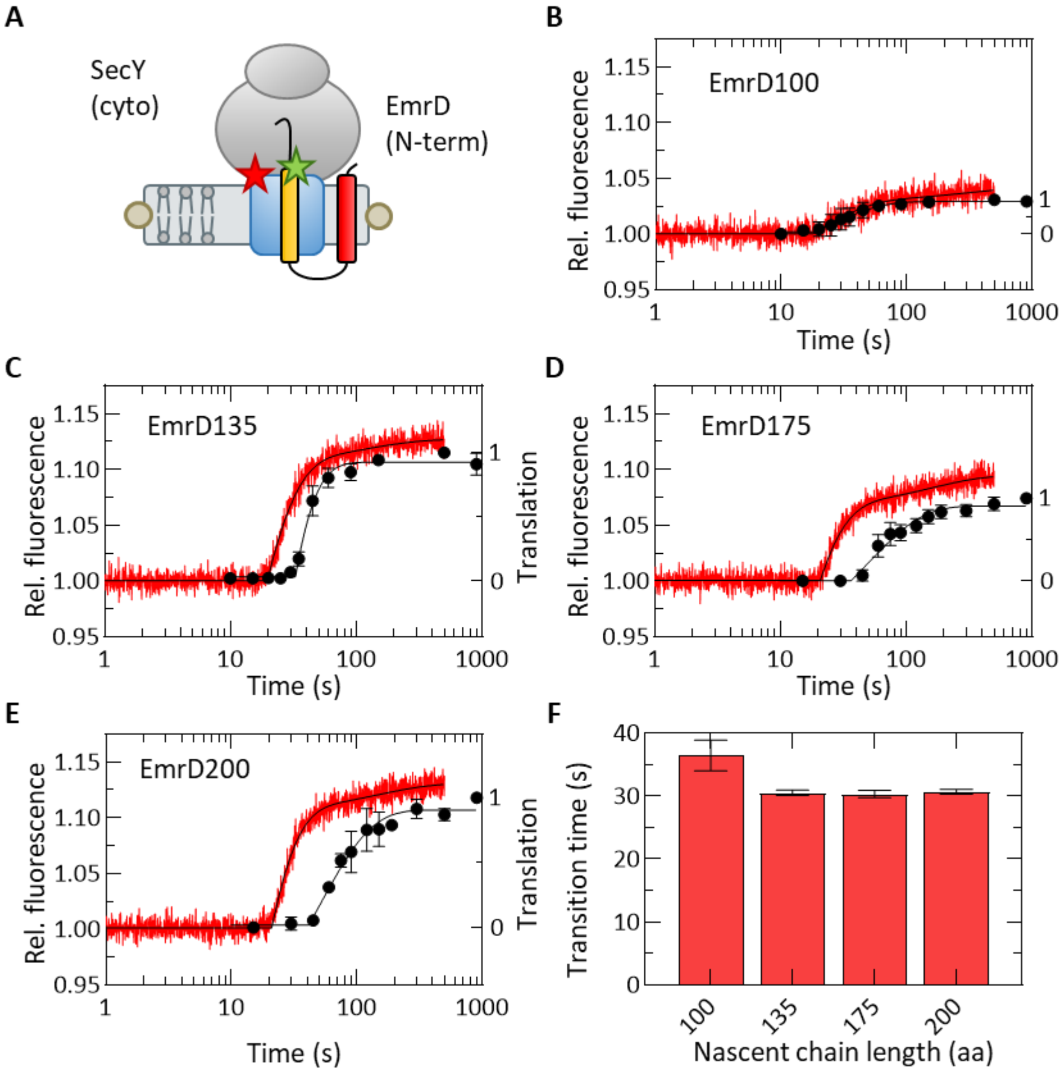

Figure 36. FRET between TM2 and the cytoplasmic label on the translocon.

(**A**) Positioning of Bpy (green star) at the C-terminus of TM2 in the nascent chain (yellow) and A647N (red star) on the cytoplasmic side of the translocon (blue).

(**B**)-(**E**) Co-translational FRET changes. Fluorescence changes of the FRET acceptor were monitored in a stopped-flow apparatus (left y-axis) and translation time courses are shown for comparison (right y-axis) for EmrD100 (**B**), 135 (**C**), 175 (**D**) and 200 (**E**). Lines depict fitting with a delay-exponential function with one (translation) or two (fluorescence) exponential terms. Error bars represent the standard deviation of three independent experiments.

(**F**) Transition times obtained by delay-exponential fitting of co-translational fluorescence changes. Error bars indicate the standard error of the fit.

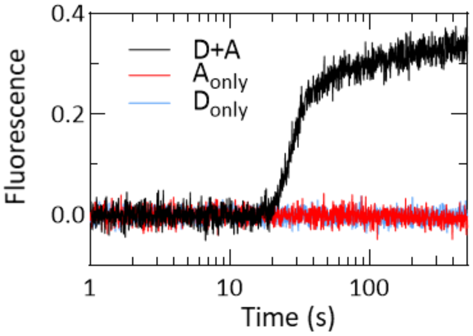

Figure 37. FRET controls. Acceptor fluorescence was recorded with EmrD200 in the presence of acceptor and donor fluorophores as well as with the acceptor alone and donor alone. Fluorescence change obtained with both donor and acceptor is due to FRET.

When the same experiments were carried out with EmrD(intern) and a label on the periplasmic side of the translocon, the kinetic signature was very similar. The delay is about 20 s and FRET appears at around 100 aa (Figure 38). The FRET increase occurs at the same time for all nascent chains independent of the final length (Figure 38F) which is at about 96 ± 4 aa and similar to the cytoplasmic label as calculated for EmrD135.

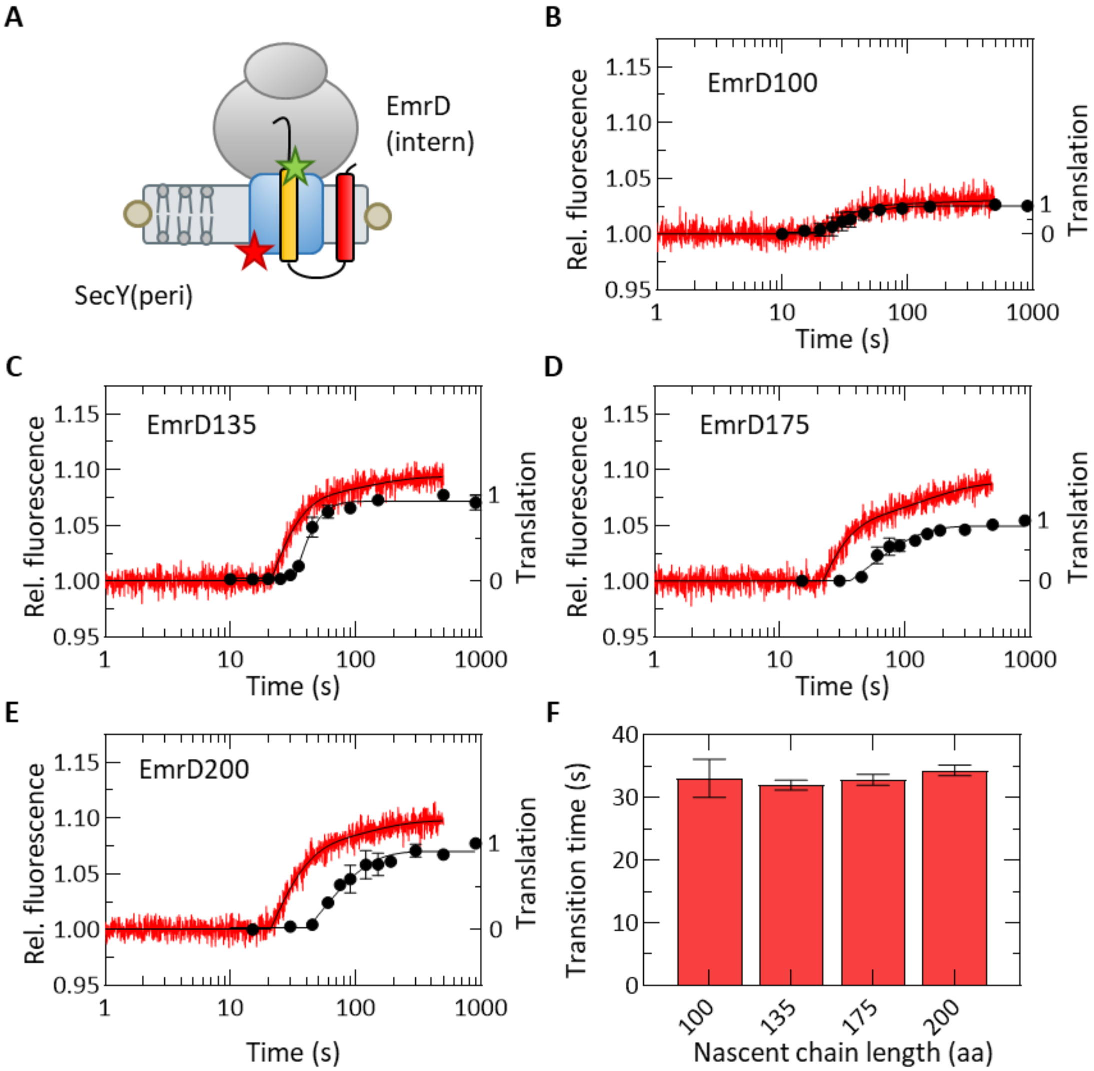

Figure 38. FRET between TM2 and periplasmic label on translocon.

(**A**) Location of Bpy (green star) on TM2 of the nascent chain (yellow) and A647N (red star) on the periplasmic side of the translocon (blue).

(**B**)-(**E**) Co-translational FRET changes. Fluorescence changes of the FRET acceptor were monitored in the stopped-flow apparatus (left y-axis) and translation time courses are shown for comparison (right y-axis) for EmrD100 (**B**), 135 (**C**), 175 (**D**) and 200 (**E**). Lines depict fitting with a delay-exponential function with one (translation) or two (fluorescence) exponential terms. Error bars represent the standard deviation of three independent experiments.

(**F**) Transition times obtained by delay-exponential fitting of co-translational fluorescence changes. Error bars indicate standard error of the fit.

To identify folding intermediates of TM2 relative to the translocon, the amplitudes of the co-translational phases were analyzed (Figure 39). For EmrD 100, FRET efficiency is low and decreased significantly when the chain length increases to 135 aa. Then, at 175 aa FRET efficiency decreases but it is high again at 200 aa. Because all constructs show high translation efficiencies and no correlation was observed between translation efficiency and fluorescence change, the measured FRET changes reflect authentic distance changes between the two fluorophores. This indicates that the cytoplasmic side of TM2 approaches the translocon, then moves away from it and finally comes close again. The FRET efficiency is consistently higher for the cytoplasmic label compared to the periplasmic label, which shows that the end of TM2 remains on the cytoplasmic side of the translocon. Compared to the behavior of TM1 (Figure 32), TM2 appears to change its position more and to be more dynamic but the changes are the same relative to the two labeling positions on the translocon (Figure 39B).

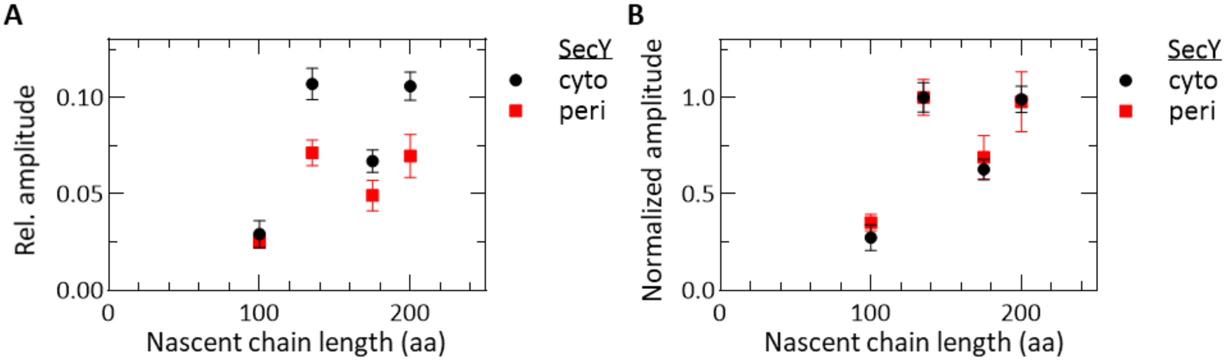

Figure 39. Fluorescence end levels.

(**A**) Amplitudes of the co-translational fluorescence change in Figures 36 and 38 were plotted for the different acceptor positions. Error bars represent the standard deviation of six technical replicates.

(**B**) Fluorescence amplitudes were normalized to the highest amplitude.

2.3.5 TM2 approaches TM1 upon emergence from the ribosome

To analyze the folding of EmrD, rather than translocon insertion, the distance between the N-terminus and TM2 was monitored by FRET. The donor fluorophore Bpy was positioned at the cytoplasmic side of TM2 as described above. Because labeling of Met-tRNA^{fMet} with A647N was unsuccessful, Atto655 (A655) was used as acceptor fluorophore and incorporated at the N-terminus via A655-Met-tRNA^{fMet}. To compare the Förster radii of the two FRET pairs, EmrD(N-term) was inserted into A647N or A655 labeled

SecY(179C)EG nanodiscs (Figure 40A). With both acceptors, the change of fluorescence occurs in two phases and the co-translational phase perfectly overlaps with transition times of 20.4 ± 0.2 s for A647N and 20.3 ± 0.3 s for A655. This indicates that the Förster radii for the two FRET pairs are similar and the rates of fluorescence changes are directly comparable. The post-translational phases, however, differ between the two acceptor dyes which might arise from different dye properties. Translation of double-labeled EmrD(double) with A655 on the N-terminus and Bpy at the end of TM2 can be quantified either by the donor or the acceptor fluorophore which results in the same translation kinetics (Figure 40B). Furthermore, the presence of an N-terminal fluorophore does not change the translation kinetics compared to EmrD(intern). The overall efficiency of Bpy-Lys incorporation as determined by radioactive counting remains high (>80%) and with this labeling strategy every donor fluorophore in the nascent chain will also contain an acceptor.

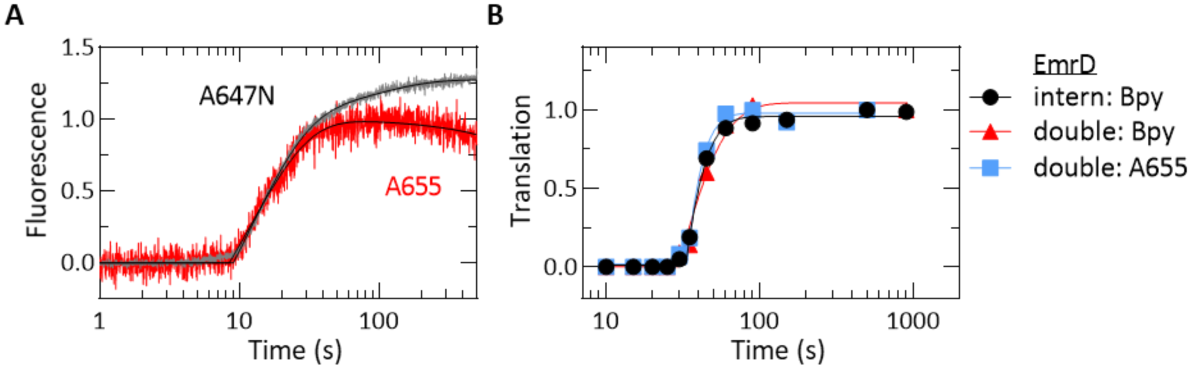

Figure 40. A655 as FRET acceptor.

(**A**) Co-translational insertion of EmrD(N-term)200 into nanodiscs containing SecY(179C) labeled with A647N or A655. Fluorescence changes were fitted to a delay-exponential equation with two exponential terms and normalized on the amplitude of the fast phase.

(**B**) Translation time courses of EmrD(intern)135 and EmrD(double)135. Formation of full-length product was quantified either by Bpy or A655 fluorescence as indicated.

Co-translational folding of EmrD(double) was analyzed by intramolecular FRET changes during the insertion of the nascent chain into nanodiscs containing wild type SecYEG (Figure 41A). Fluorescence controls revealed a small decrease in acceptor fluorescence as A655 moves through the peptide exit tunnel, however this cannot explain the fluorescence changes in the presence of donor and acceptor fluorophores which result from FRET (Figure 41B). To compensate for the acceptor changes, corrected data is analyzed where the acceptor only and donor only traces have been subtracted from the fluorescence curves (Figures 41C-F). In an extended conformation, the distance between the two fluorophores is too large for FRET and an increase of FRET efficiency occurs upon folding. As the fluorescence changes showed a single phase, the fluorescence intensity was fitted to a delay-exponential equation with one exponential term. FRET increases occur co-translationally which is shown by comparison to the translation time courses. The fluorescence increases at 110 ± 4 aa which was determined for EmrD135 and which occurs roughly at the same time independent of the final nascent chain length (Figure 41G). Compared to the FRET change between TM2 and the cytoplasmic label on the translocon at a nascent chain length of 96 aa, more amino acids have to be synthesized indicating that TM2 approaches the translocon before the N-terminus. The two fluorophores reach a high FRET state at 135 aa, FRET remains high at 175 aa and decreases at 200 aa which indicates conformational rearrangements of the nascent chain (Figure 41H).

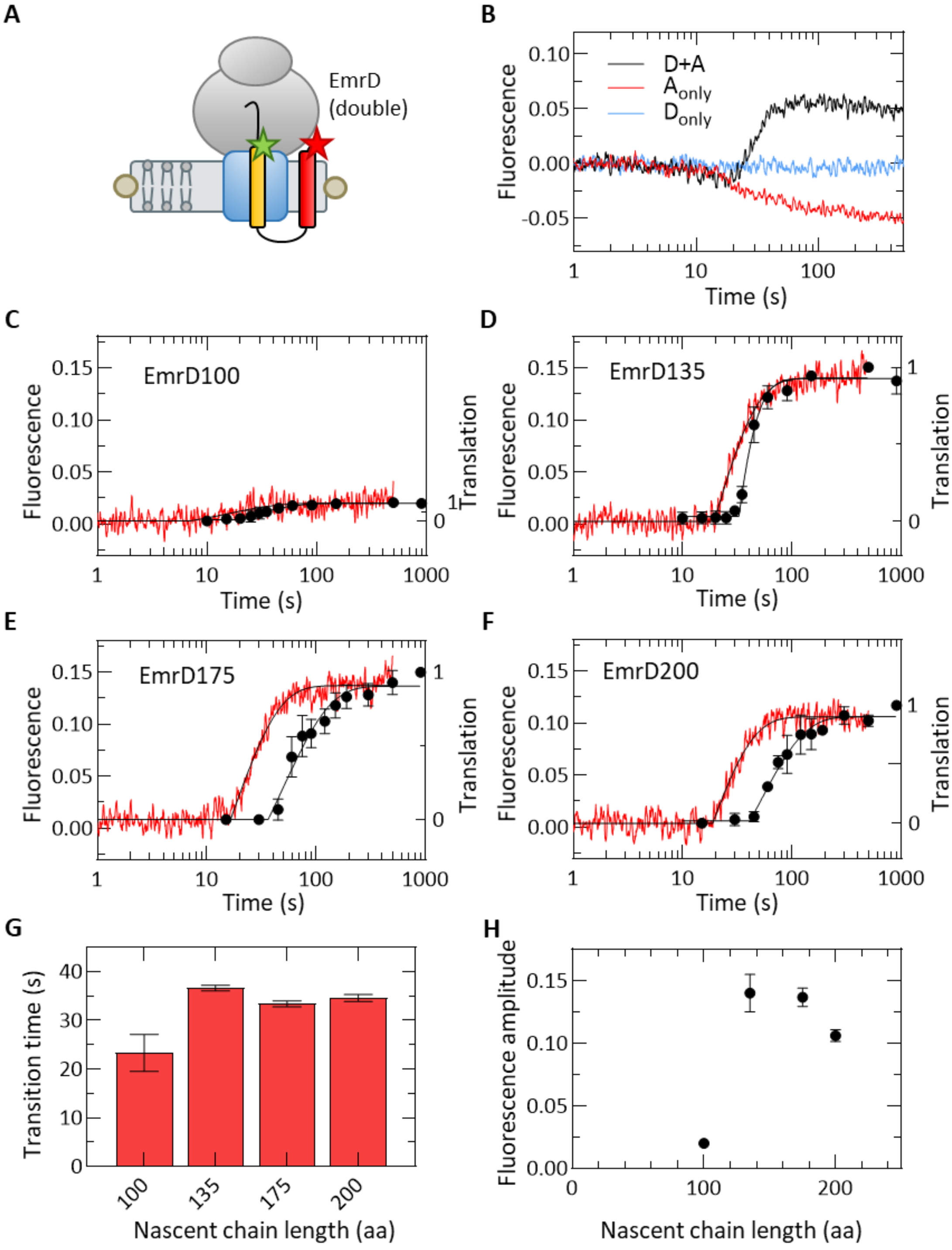

Figure 41. FRET between the N-terminus and TM2 of EmrD. The legend is continued on p. 65.

Figure 41. Continued from p. 64.

(**A**) Positioning of Bpy (green star) on TM2 (yellow) and A655 (red star) on the N-terminus of the nascent chain.

(**B**) FRET controls. Donor only and Acceptor only controls show small co-translational fluorescence changes which do not account for FRET observed with both labels.

(**C**)-(**F**) Co-translational FRET changes. Fluorescence changes of the FRET acceptor were corrected for changes in the acceptor and donor only controls and smoothed for clarity (left y-axis) and translation time courses are shown for comparison (right y-axis) for EmrD100 (**C**), 135 (**D**), 175 (**E**) and 200 (**F**). Lines show fitting to a delay-exponential function with one exponential term. Error bars represent the standard deviation of three independent experiments.

(**G**) Transition times obtained by delay-exponential fitting of fluorescence curves. Error margins indicate standard errors determined from delay-exponential fitting.

(**H**) Amplitudes of the fluorescence change in (**C**)-(**F**). Error bars indicate the standard deviation of six technical replicates.

To compare diverse fluorescence reporters for the different nascent chain lengths, the transition times of the co-translational phase were analyzed (Figure 42) as determined by delay-exponential fitting (Figures 29, 31, 36, 38 and 41). For all constructs, the N-terminal fluorophore requires less time to arrive at the translocon than the reporter in TM2 at position 67 which is expected, as translation of the peptide up to the incorporation site takes additional time. The position of the dye on the translocon (cytoplasmic vs. periplasmic side) has only a small effect on the timing of FRET. The signal change of the intramolecular FRET pair occurs later than docking at the translocon and thus, TM2 first approaches the cytoplasmic label on the translocon before it comes in close proximity to the N-terminus.

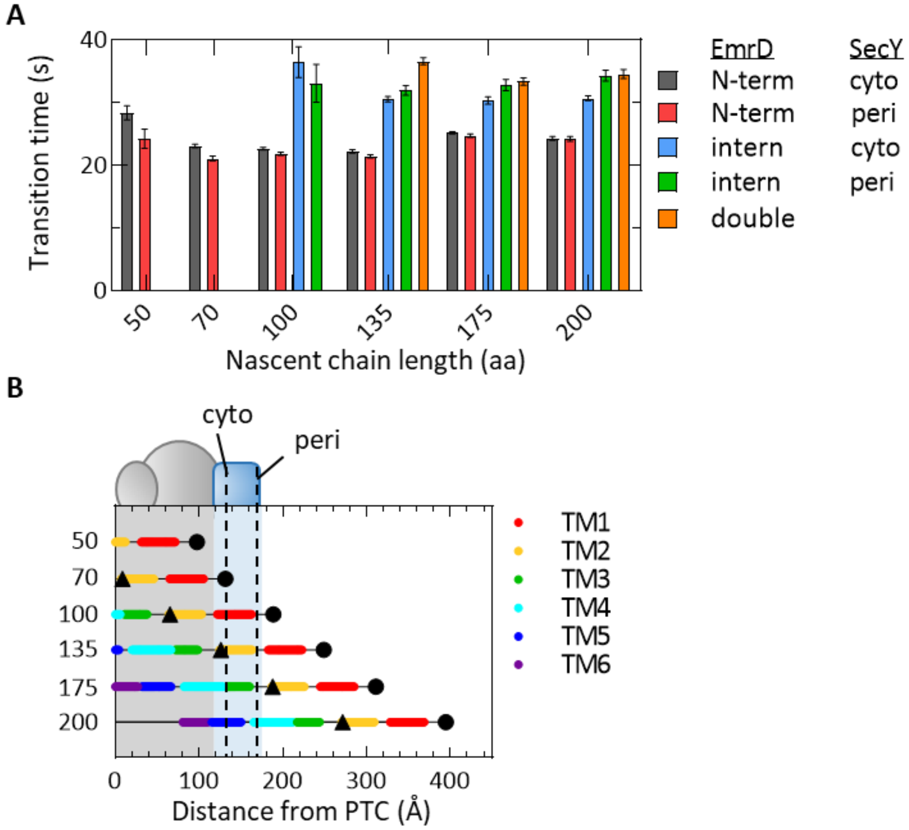

Figure 42. Comparison of the different FRET pairs.

(**A**) Comparison of transition times for different FRET pairs by EmrD length. Rates of co-translational fluorescence changes are shown with error bars representing the standard error determined by delay-exponential fitting.

(**B**) Fluorescence reporter positions depending on nascent chain length relative to the ribosome exit tunnel (gray), the translocon pore (blue) and the lipid bilayer (white). Fluorophores are positioned on the N-terminus (black circle), at the end of TM2 (black triangle) or on the translocon (dotted lines

3 Discussion

3.1 Deformylation in a cellular context

The kinetic analysis of PDF activity on RNCs has revealed a reversible reaction with predominantly fast steps for binding and dissociation and a slow rearrangement, which takes place after deformylation and limits the rate of PDF dissociation from nascent peptides (Figure 43). Previous work has indicated that PDF has a similar affinity to ribosomes and RNCs carrying a short, non-exposed nascent chain in the ribosomal exit tunnel (Sandikci et al., 2013). Using pre-steady-state association experiments, we show that even when the nascent chain is accessible for PDF, the initial binding kinetics is the same as with vacant ribosomes (Figure 19). Docking of the N-terminus into the active site of PDF is apparently rapid since it is not identified as an additional kinetic step, but it can be slowed or prevented by binding to SRP when the nascent chain carries an SRP-specific signal anchor sequence (Ranjan et al., 2017; Yang et al., 2019). The affinity of PDF for ribosomes and RNCs is in the range of 2 µM, so given cellular concentrations of ribosomes (20-45 µM depending on the growth rate (Rudorf and Lipowsky, 2015)) and PDF (2 µM (Ragusa et al., 1998)), the majority of the PDF molecules are expected to be bound to ribosomes. However, due to the large excess of ribosomes, only a small fraction can interact with PDF at a given time but fast association and dissociation allow PDF to rapidly scan ribosomes for formylated nascent chains. Based on the rate constants determined here, PDF binds one ribosome every 0.3-2 ms on average, depending on the ribosome concentration, and the average residence time is 15 ms, allowing each PDF molecule to sample about 60 ribosomes in one second. At this rate, it takes 0.2 to 1 s for the roughly 1,300 molecules of PDF to scan all 10,000-70,000 ribosomes in the cell (Bremer and Dennis, 2008; Ragusa et al., 1998). During this time, a nascent chain can be elongated by up to 20 aa. Since nascent chains suitable for deformylation are between 50 and 120 aa in length (Ranjan et al., 2017; Yang et al., 2019), scanning is fast enough to reach all accessible formylmethionines within the available time window. Although the area around the ribosomal tunnel exit also serves as a binding platform for other RPBs, PDF binding is not affected by either SRP or TF, indicating that scanning by PDF should proceed unabated *in vivo* in the presence of the other factors (Bornemann et al., 2008). MAP, which removes the initial methionine after deformylation, however, competes with PDF on the ribosome (Bhakta et al., 2019; Sandikci et al., 2013), which will prevent PDF from rebinding to nascent chains recruited to MAP and, therefore, enhance scanning of other ribosomes.

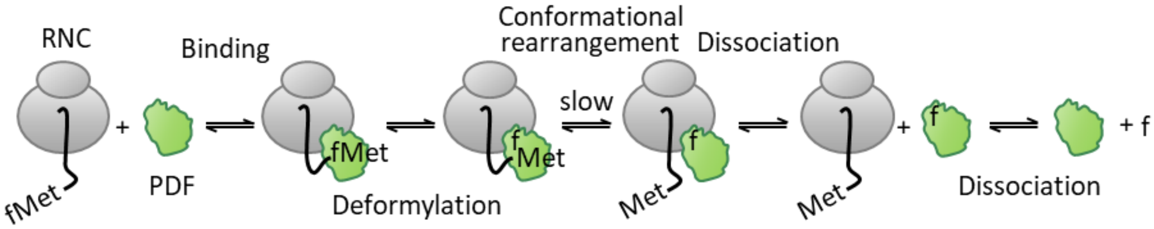

Figure 43. Mechanism of deformylation.

The reversible hydrolysis and existence of a slow rearrangement step after deformylation are, at first glance, surprising. However, previous studies with model peptides have shown that PDF can transfer the formyl group from one peptide to another (Becker et al., 1998), indicating that a deformylated peptide can indeed act as a substrate for PDF. Deformylation as such does not trigger immediate release of the nascent chain from PDF, probably due to the similarity between the formylated and deformylated nascent chain. This is consistent with structural work indicating that most of the interactions between the peptide and PDF involve the peptide backbone and the methionine side chain, all of which remain unchanged during deformylation (Becker et al., 1998). In addition, the presence of the formyl group is not monitored stringently by the enzyme, as substrates that are acetylated or carry a different N-terminal amino acid display a K_M value similar to fMet-peptides (Hu et al., 1999). Also, the reversibility of the deformylation reaction agrees with studies on model peptides showing that adding increasing amounts of deformylated peptide into the reaction decreased the initial velocity (Lazennec and Meinnel, 1997). Thus, the key features of the reaction mechanism are conserved between the model substrates and RNCs. The reason for rapid turnover with model substrates is that their affinity for PDF is low, promoting the dissociation of the complex, whereas with RNCs, PDF contacts with the ribosome favor retention of the nascent chain at the enzyme active site, resulting in a k_{cat} that is 50-fold lower compared to model peptides. The slow rearrangement likely involves release of the N-terminus from the active site of PDF, since this step is followed by rapid dissociation of PDF from the ribosome. Different lengths of the nascent chain as well as amino acid composition and secondary structure elements near the N-terminus can moderately influence the velocity of deformylation (Ranjan et al., 2017; Yang et al., 2019). This is consistent with our analysis indicating that different rates of deformylation among RNC substrates depend on the rate-limiting conformational rearrangement of the nascent chain which is reflected by the individual rate constants k_3 for each RNC substrate in the kinetic model.

Our co-translational deformylation experiments show that the N-terminus of a nascent protein can be deformylated as soon as it emerges from the tunnel exit of a translating ribosome, consistent with previous studies (Giglione et al., 2004; Giglione et al., 2015). This finding becomes important in the context of co-translational folding, in particular for small N-terminal domains that can fold within the ribosomal exit tunnel (Holtkamp et al., 2015; Nilsson et al., 2015). For these proteins, it is important that PDF acts early, before the N-terminus is buried within a folded domain (Koubek et al., 2021; Ranjan et al., 2017). Rapid deformylation followed by a slow rearrangement step may ensure that PDF holds the N-terminus of the nascent chain for handover to downstream enzymes in nascent-chain processing. Specifically, the reversible deformylation and subsequent slow conformational rearrangement are responsible for the delay in methionine removal by MAP, which was observed in a coupled PDF-MAP assay (Yang et al., 2019). Rapid PDF dissociation after the conformational rearrangement allows it to effectively vacate the primary binding site of MAP on the ribosome (Bhakta et al., 2019; Sandikci et al., 2013), and subsequent binding of MAP is fast (Yang et al., 2019), indicating that pre-organization of MAP or ‘priming’ at a secondary binding site on the ribosome is not required for efficient exchange of factors. Retention of the N-terminus by PDF may also prevent folding (or misfolding) of the nascent protein prior to recruitment of the ribosome-associated chaperone TF, which binds preferentially to longer nascent chains, about 100 aa in length (Oh et al., 2011). Therefore, PDF might help to bridge the gap between emergence of the nascent chain from the ribosome and chaperone binding. The slow rearrangement that follows deformylation may introduce a relatively long pause into any number of events in the life of a nascent protein, including processing and folding.

3.2 Specificity of PDF inhibitors

Here we show that fumimycin is a weak inhibitor of *Ec*PDF even though previous experiments revealed it to be a moderate inhibitor of *Sa*PDF (Kwon et al., 2007). The two PDFs belong to different classes of PDFs that show only small differences in their active sites but their peptide binding clefts are significantly different which could explain the differential inhibitory power of fumimycin (Baldwin et al., 2002; Giglione et al., 2004; Yoon et al., 2004). Comparison of crystal structures of another PDF inhibitor, actinonin, bound to *Ec*PDF or *Sa*PDF confirms that the metal binding hydroxamate moieties overlap very well while the pyrrolidine is positioned differently (Figure 44) (Clements et al., 2001; Yoon et al., 2004). Additionally, it has been shown that hydroxamate based inhibitors show a varying activity against different bacterial species (Apfel et al., 2000). Furthermore, our inhibition studies showed that a strong metal binding motif like hydroxamate does not necessarily lead to efficient PDF inhibition depending on the chemical structure of the inhibitor so that inhibition can be fine-tuned by modifications. Docking studies suggested that in fumimycin the catechol moiety acts as metal binding motif (Zaghouani et al., 2019) which increases the variety of potential structural motifs for PDF inhibition. A recent study, for example, characterized compounds with esters or hydrazides as metal binding sites that inhibit PDF from *Mycobacterium tuberculosis* while showing low cytotoxicity against macrophages (Gokhale and Telvekar, 2021). Therefore, PDF inhibitors have the potential to gain enough specificity to target infectious bacteria without inhibiting *Hs*PDF in mitochondria and to become a new class of antibiotics. In studies using a variety of different bacteria, however, resistance against PDF inhibitors was detected at high frequency (10^{-8} - 10^{-6}) (Apfel et al., 2001; Margolis et al., 2001; Margolis et al., 2000). Resistance was achieved by efflux of the drug, mutations in the peptide deformylase gene or inactivation of methionyl-tRNA transformylase, the latter being the most common (Margolis et al., 2001; Margolis et al., 2000; Sharma et al., 2009). Due to the reduced cell growth of the transformylase mutants, PDF inhibitors might still be effective and PDF a viable antibiotic target (Giglione and Meinnel, 2001).

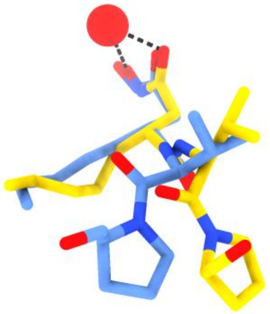

Figure 44. Actinonin bound to *Ec*PDF (blue, PDB: 1G2A) and *Sa*PDF (yellow, PDB: 1Q1Y). The interaction with the metal cofactor (red) is indicated.

Similar to the PDF inhibitor actinonin, fumimycin and its analogues are described as competitive inhibitors that bind to the active site of PDF and form a complex with the metal ion (Chen et al., 2000; Clements et al., 2001; Kwon et al., 2007). This indicates that binding of inhibitor-bound PDF to an RNC is still possible, but interaction of the formylated N-terminus with the active site of PDF is impaired. Due to the higher affinity of PDF towards RNCs compared to model peptides, higher concentrations of inhibitor or more tightly binding compounds are necessary to efficiently inhibit deformylation of RNCs.

3.3 Co-translational folding pathway of TMs 1-4 of EmrD

By combining the real-time fluorescence information gained from different FRET pairs, the initial steps of the co-translational folding of EmrD can be modeled in some detail (Figure 45). Here, we provide insights into the folding of the first four TMs following the folding pathway from short to long nascent chains and show how this relates to current models regarding TM insertion into the translocon and the lipid bilayer. At short nascent chain lengths, the N-terminus approaches the translocon reaching the minimal distance for FRET around a nascent chain length of 50 aa and moves closer towards the translocon at 70 aa (Figure 32). As the N-terminus remains on the cytoplasmic side of the membrane at all lengths, EmrD assumes an N-in topology and TM1 has to invert to be inserted correctly into the lipid bilayer. Previous experiments indicate that inversion occurs due to charge-charge interactions between positively charged amino acids at the N-terminus of the nascent chain and negative charges in the ribosomal peptide exit tunnel (Mercier et al., 2020). This inversion is established early on and appears to occur before a length of 50 aa when the N-terminus is buried deep inside the peptide exit tunnel. Even in the absence of the translocon or a membrane, formation of a helix-turn-helix in the ribosomal vestibule was observed by crosslinking of TMs which suggests that the ribosome triggers inversion (Tu et al., 2014). Our results indicate that the number of amino acids required to span the distance from the PTC to the point where FRET can be detected is larger for the N-terminal label compared to the label at TM2 (Figures 29 and 31). This supports an early inversion of the N-terminus inside the ribosome before FRET can be detected. Similarly, previous protease protection assays show that an N-out helix is protected faster by the translocon than an N-in TM (Mercier et al., 2020). In contrast, force profile analysis indicates that the same nascent chain length is required to insert N-in or N-out TMs with minor changes due to charged or hydrophobic residues upstream of the TM (Nicolaus et al., 2022; Nicolaus et al., 2021). However, most of the studied TMs with N-in topology were internal and inversion of these TMs might follow a different mechanism. In this case, three instead of two peptide chains need to be accommodated next to each other, which is more likely at the ribosome translocon interface (Mercier et al., 2022; Park et al., 2014). Even though TMs were shown to compact inside the exit tunnel (Bano-Polo et al., 2018; Robinson et al., 2012; Woolhead et al., 2004), short nascent chains of EmrD (<50 aa) were accessible to proteinase digestion (Mercier et al., 2020) when a fully compacted nascent chain is still buried within the ribosome (Figure 27A). Furthermore, the limited space in the exit tunnel, especially with a translocon bound, does not allow a folded helix to invert (Park et al., 2014). Therefore, TM1 may assume a partially extended conformation during its inversion where folded and unfolded states are in equilibrium (Agirrezabala et al., 2022; Liutkute et al., 2020b; Mercier et al., 2022).

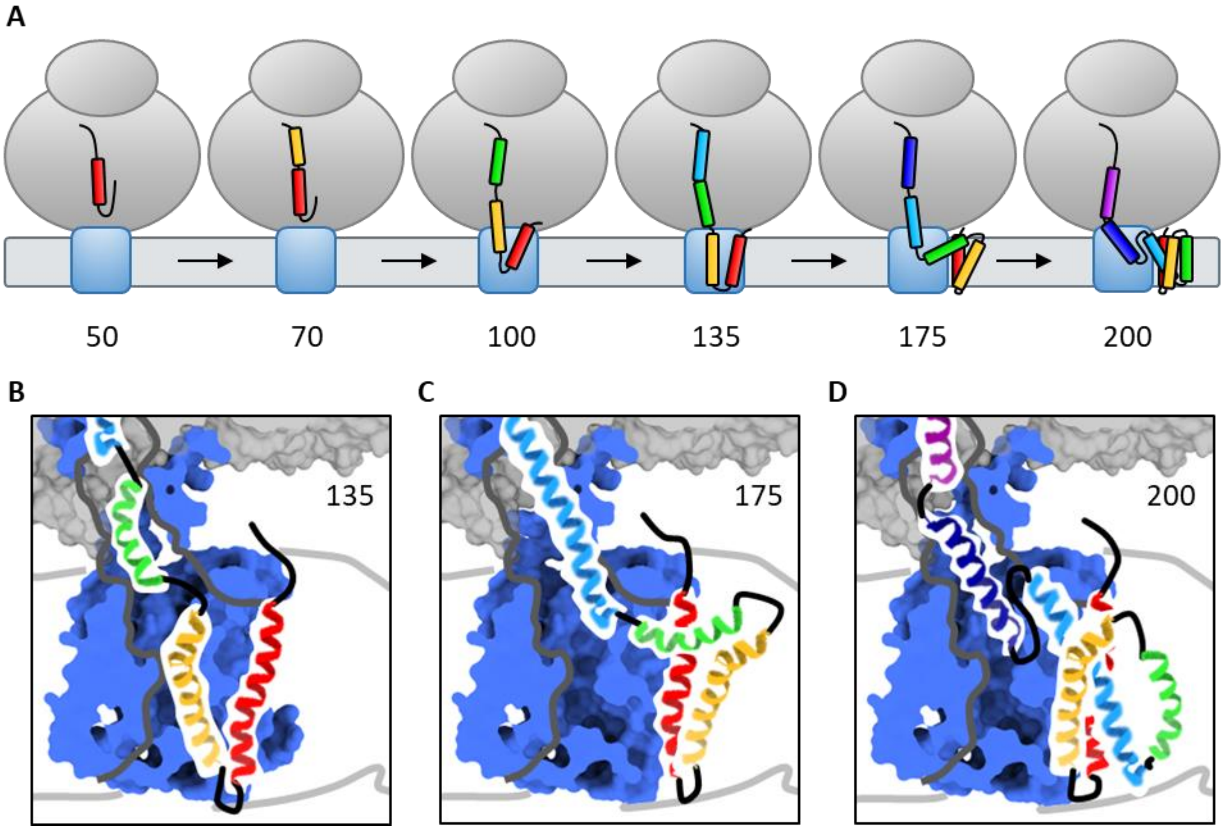

Figure 45. Co-translational folding intermediates of EmrD as derived from FRET experiments.

(**A**) Folding model. The ribosome (gray) is synthesizing a nascent chain of six TMs (red to purple) that are inserted into the membrane (gray) via the translocon (blue). TM positions in the amino acid sequence have been assigned according to the crystal structure (Figure 16, PDB: 2GFP); TM1: 9-36, TM2: 42-68, TM3: 76-94, TM4: 95-127, TM5: 132-155, TM6: 157-177.

(**B**)-(**D**) Structural model. Long nascent chain intermediates EmrD135 (**B**), EmrD175 (**C**) and EmrD200 (**D**) were modeled using experimentally determined structures (PDB: 4V6M, 2GFP). For clarity, only the area around the translocon is shown.

From 50 to 100 aa, the N-terminus moves closer towards the translocon and reaches a high FRET state when FRET-acceptors are positioned on either the cytoplasmic or periplasmic side of SecY (Figure 32). As the nascent protein is extended beyond 100 aa and the four N-terminal TMs are inserted into the membrane (Figures 27A and 45), no significant changes are observed relative to the translocon (Figure 32). Therefore, co-translational folding of at least these four helices of EmrD occurs close to the translocon either due to protein-protein interactions or interactions of positive charges in cytosolic loops with the ribosome (Bischoff et al., 2014; Hou et al., 2012; Sadlish et al., 2005). At 100 aa, the distance between

TM2 and either the translocon or the N-terminus is large indicating that the end of TM2 resides inside the ribosomal peptide exit tunnel (Figures 39 and 41).

This changes at 135 aa when the nascent chain is long enough for TM2 to fully insert into the translocon and FRET between TM2 and the translocon increases (Figures 39 and 45B). When two TMs have been inserted into the translocon and/or the membrane, co-translational formation of tertiary structural elements can begin. For the soluble protein HemK, co-translational folding studies revealed that individual folding events are faster than translation and can therefore occur at quasi-equilibrium conditions (Liutkute et al., 2020a; Mercier and Rodnina, 2018). Similarly, co-translational folding intermediates of EmrD may likely rapidly sample different conformations to find the thermodynamic optimum at each nascent chain length. The high FRET between the cytosolic side of TM2 and the N-terminus indicates that TM1 and TM2 are in close proximity and potentially form a helix-turn-helix motif (Figure 41). However, interactions between the cytoplasmic sides of TM1 and TM2 are not native because in the crystal structure TM4 resides between them and therefore contacts are most likely transient (Yin et al., 2006). On the other hand, the short loop of 4 aa between TM1 and TM2 keeps the periplasmic sides of the TMs close together (Tastan et al., 2009). The lateral gate of the translocon is highly dynamic and assumes a more open conformation in the presence of TMs allowing hydrophobic helices to partition into the lipid bilayer (Ge et al., 2014; Mercier et al., 2021). Some studies on eukaryotic translocons also show retention of TMs inside the translocon (Skach, 2009). Due to limited space inside the translocon pore, TM1 is expected to reside in the open lateral gate indicating that TM2 displaces TM1 towards the lipid bilayer (Frauenfeld et al., 2011; Park et al., 2014). This is further supported by our kinetic analysis showing that TM2 approaches the translocon slightly before it approaches the N-terminus (Figure 42).

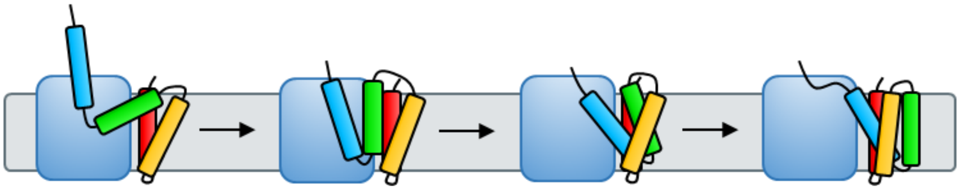

Figure 46. Folding of TMs 1-4. The model for the folding pathway of the first four TMs (red-blue) between 175 and 200 aa at the translocon (dark blue) is shown. The ribosome and subsequent TMs were omitted for clarity.

At a length of 175 aa, the N-terminus and TM2 remain in close proximity (Figure 41). The distance of TM2 to the translocon increases compared to 135 aa while the N-terminus stays close to the translocon (Figures 32 and 39). Therefore, TM1 remains roughly at the same location while at least the cytoplasmic side of TM2 rotates around it and away from the translocon. This movement potentially prepares TM1 and TM2 to split and allow TM3 and TM4 to move in between them at a later stage in folding (Figure 45C). When the nascent chain reaches a length of 200 aa, TM1 and TM2 assume similar positions relative to the translocon compared to 135 aa. Their cytosolic sides, however, are further apart, indicating that TM4 resides between them (Figure 45D), as shown in the crystal structure (Yin et al., 2006). On the basis of our experimental results and the crystal structure, we suggest a pathway connecting the folding intermediates at 175 and 200 aa and describe the passing of TM3 and TM4 in between TM1 and TM2 as the most probable way to reach the final fold (Figure 46). In analogy to TM1 and TM2 which are in close proximity during transition from the translocon to the lipid bilayer, TM3 and TM4 are expected to insert into the membrane simultaneously, directly passing over the periplasmic loop between TM1 and TM2 which is facilitated by the short length of TM3. Interestingly, a short TM3 appears to be an evolutionary conserved feature because a comparison of other proteins from the same MFS family (LacY, GlpT, SotB, YajR) reveals that, in general, every third helix is shorter than the two before (Figure 47A). When inner membrane proteins from other families like the major intrinsic protein family (AqpZ), general secretory pathway family (SecY), the ATP binding cassette superfamily (BtuC) or the resistance-nodulation-cell division superfamily (AcrB) were analyzed, no such trend was observed (Figure 47B). Therefore, a short TM3 might be connected to the conserved MFS folding pattern (Figure 47C) and indeed allow threading of TM3 through TM1 and TM2. For the four helices to fold into the correct stereoisomer, TM1 is required to bind to the outside of the translocon near the lateral gate helix TM2b and the translational pause in EmrD synthesis around 137 aa (Figure 27D) might allow TM1 to sample the translocon for the optimal binding site. Previous studies have shown that TMs can assume distinct locations on the translocon (Sadlish et al., 2005) so that identification of the binding site of TM1 on the translocon, for example via cross-linking studies, would provide more information on the folding pathway of TM1-4. Another folding mechanism would be possible that requires TM1 to bind on the other side of the lateral gate but this pathway is not applicable on the second, symmetric half of EmrD. The suggested threading of TM3 and TM4, however, can be repeated with TMs 7-10 and most likely also with other MFS members.

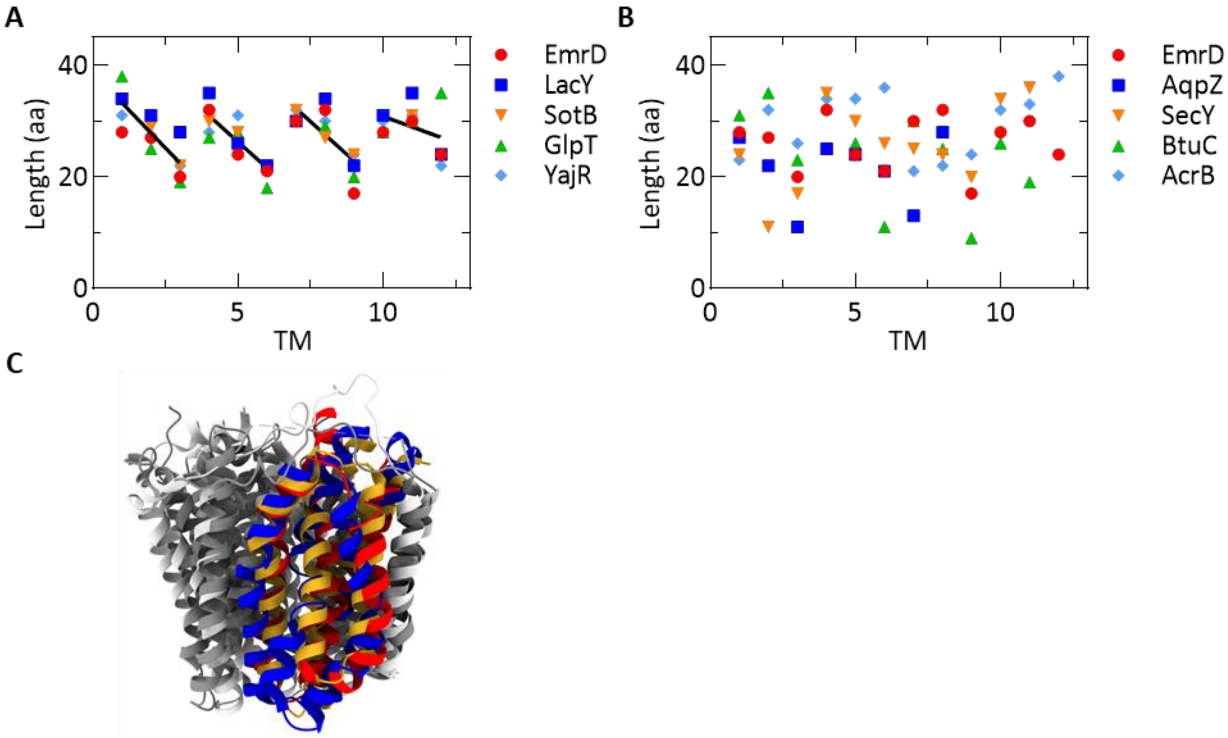

Figure 47. Comparison TM length and folding pattern.

(**A**) MFS superfamily. Different members of the MFS protein family were compared regarding their TM lengths.

(**B**) TM lengths were compared for members of a variety of different membrane protein families.

(**C**) Comparison of crystal structures. The structures of three MFS members EmrD (red), LacY (blue) and SotB (yellow) are overlaid and the first 4 TMs are colored.

Our results indicate that insertion of TM1 and 2 into the lipid bilayer occurs simultaneously as they are in close proximity after TM2 enters the translocon (Figure 45A). Additionally, inversion of TMs inside the ribosome will lead to an automatic pairing of helices at the translocon. These building blocks can also be observed in AFM-based protein extraction studies (Jefferson et al., 2018). As with the first two helices of EmrD that split after they have been inserted into the lipid bilayer, these helix pairs do not necessarily possess all native contacts obtained in the final fold. The limited space inside the translocon does not allow dimers to form completely inside the translocon pore so that TM2 dislocates TM1 towards the lipid bilayer. Therefore, TM1 integrates into the membrane slightly before TM2 potentially resulting in the sequential insertion of TMs observed in force profile analysis (Nicolaus et al., 2021). Insertion at the translocon has been suggested to proceed via the translocon-insertion or the sliding model (Cymer et al., 2015). As discussed above, our data support the inversion of the N-terminus inside the ribosome which points towards the translocon-insertion model but does not exclude that TM1 samples the lipid bilayer before engaging the translocon as suggested in the sliding model. With folded α-helices however, the short loop after TM1 hinders TM2 in sampling the membrane-water interface and the sliding model is only feasible for TMs with an N-in topology. As the exact position of the TM during insertion at the translocon has not yet been observed, either inside the translocon or in contact with the lipids, a combined model would be possible. Here, an N-in TM would invert inside the ribosome and directly engage the translocon but slide down the lateral gate while contacting the lipids which would account for the limited space inside the translocon. The classic three state model for membrane protein folding (Engelman et al., 2003) has to be further extended in the concept of co-translational folding. The individual states of TM insertion, folding and oligomerization or cofactor binding are still important milestones in the maturation of a membrane protein but they can all happen at the same time. Here we show that already during insertion, TMs like TM1 and TM2 of EmrD can interact with each other and form folding intermediates before the whole protein is synthesized, and other studies have demonstrated that even oligomerization can occur co-translationally (Lu et al., 2001).

3.4 Co-translational protein maturation

The actions of RPBs are highly coordinated in relation to the length of the nascent chain (Figure 48) and because folding, for example, can reduce the accessibility of the new protein for RPBs, it is important that RPBs act early on. PDF deformylates cytosolic proteins as soon as the N-terminus emerges from the exit tunnel and MAP can only act afterwards. The retention of the nascent chain by PDF during ongoing translation on one hand and chaperone binding or nascent-peptide folding as it moves away from the ribosome surface on the other hand define the time window for MAP to access the N-terminus co-translationally, which may explain the incomplete methionine removal in some proteins (Yang et al., 2019). At a length of 100 aa, TF stably engages the nascent chain (Oh et al., 2011), which leaves a sufficient time window for N-terminal processing of TF client proteins. Binding of SRP inhibits deformylation by PDF (Ranjan et al., 2017) but the extent of the inhibitory effect seems to depend on the distance between the signal sequence and the N-terminus (Ranjan et al., 2017; Yang et al., 2019). Even though PDF and SRP can bind the ribosome simultaneously (Bornemann et al., 2014), SRP has the advantage that it can sense a nascent chain that is still inside the ribosome (Bornemann et al., 2008; Denks et al., 2017; Mercier et al., 2017) and bind to a signal peptide before it can be deformylated (Ranjan et al., 2017). Bypassing the relatively slow process of deformylation leads to an efficient targeting of membrane proteins to the inner membrane because long nascent chains tend to remain in the cytosol until translation is finished even if they contain a signal peptide (Ariosa et al., 2015). After targeting to the membrane, the nascent inner-membrane protein is inserted into the translocon and then partitions into the lipid bilayer where N-termini that reach into the cytosol can potentially be deformylated post-translationally, by analogy with the deformylation of model peptides (Ranjan et al., 2017).

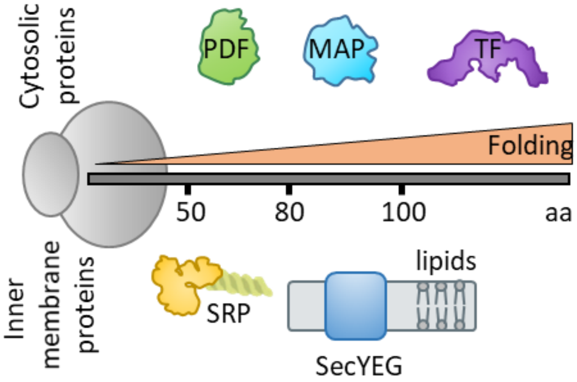

Figure 48. Co-translational protein maturation. Factors interacting with the nascent peptide chain (dark gray) at different lengths while the protein folds co-translationally. Cytosolic proteins interact with PDF (green), MAP (light blue) and TF (purple) whereas inner membrane proteins are targeted by SRP (yellow) to the SecYEG translocon (blue) and the lipid bilayer (light gray).

As the time window for RPB action and folding events is directly connected to the growth of the nascent chain, maturation of new proteins is governed by the rate of translation, which is as fast as 10-20 aa/s in *E. coli*. Because loop motions and diffusion inside a membrane occur much faster, translation is rate-limiting to protein folding (Henzler-Wildman and Kern, 2007; Liutkute et al., 2020b; Weiss et al., 2013). For this reason, it was suggested that translational pauses encoded in the mRNA evolved to slow down translation at specific moments to facilitate folding (Mercier et al., 2022; O'Brien et al., 2014; Samatova et al., 2020). In soluble proteins, for example, pause sites are found near domain junctions to help folding of the individual domains (Makhoul and Trifonov, 2002; Zhang et al., 2009). The pauses in EmrD at 48 and 137 aa could potentially mediate inversion or insertion of TMs into the membrane by giving the nascent chain more time to equilibrate and find the optimal position in its environment. Additionally, translational pauses might further facilitate interactions with RPBs increasing their time windows to act.

3.5 Conclusion and perspective

In summary, we analyzed two processes in the biogenesis of proteins. First, we developed the kinetic mechanism of deformylation of nascent chains on the ribosome. Binding and dissociation of PDF and RNCs occur rapidly and are mainly governed by interactions between the enzyme and the ribosome. This allows PDF to scan translating and non-translating ribosomes for suitable substrates quickly enough to sample the large excess of ribosomes in the cell. Scanning is stopped by rapid but reversible hydrolysis of a formylated nascent chain which can occur as soon as the N-terminus emerges from the peptide exit tunnel and becomes accessible to PDF. Then, a slow conformational rearrangement of the nascent chain that most likely facilitates the dissociation of the N-terminus from the active site of PDF delays rapid dissociation from the RNC. To confirm the nature of the rate-limiting step, the dynamics of the nascent chain when PDF is bound to an RNC may be probed by single molecule fluorescence methods. As slow deformylation limits the binding of the next processing enzyme, MAP, it will be interesting to test whether the addition of MAP to co-translational multiple-turnover deformylation experiments increases the rate of the conformational rearrangement. During co-translational experiments, the formyl group was removed as soon as the N-terminus becomes accessible while multiple-turnover deformylation was still slow. The natural compound fumimycin showed only a small inhibitory effect on *Ec*PDF which could not be improved by chemical modifications and is therefore not directly suitable as antibiotic drug candidate. Besides fumimycin, actinonin is another naturally occurring inhibitor which indicates that screening of libraries containing secondary metabolites might yield more PDF inhibitor candidates.

We also analyzed the initial steps in the folding pathway of the inner membrane protein EmrD. The N-terminus inverts early on and TM1 inserts into the translocon in an N-in conformation. Then, TM1 likely partitions into the lipid bilayer simultaneously with TM2 and the nascent chain remains close to the translocon which might assist further folding events. Here, single molecule FRET experiments would reveal the dynamics of the interactions between TM1 and TM2 as well as with the translocon. Based on our FRET measurements, we propose a folding mechanism for TM1-4 that involves threading of TM3 and TM4 in between the first two TMs which could be assessed by positioning the internal fluorophore on TM3, TM4 and the periplasmic loops. Additionally, crosslinking experiments to determine where TM1 and TM2 are contacting the translocon could provide insights to discriminate between alternative folding pathways based on the final stereomer reached in each mechanism. Furthermore, the role of the translational pause at 137 aa in the establishment of the correct positioning of TMs on the translocon could be probed by changing the codon context and analyzing the effect on FRET and cross-linking experiments. We found that TM lengths are conserved throughout the MFS superfamily that shares a characteristic folding pattern. It would be interesting to test whether other members of this family follow the same folding pathway as suggested here.

4 Materials and Methods

Figures were prepared using GraphPad Prism, UCSF ChimeraX, ChemDraw and Microsoft PowerPoint. Calculation of the Förster radius was performed using the FPbase FRET calculator.

4.1 Deformylation

4.1.1 PDF purification and labeling

PDF was expressed in BL21(DE3)pLysS (New England Biolabs) with a C-terminal His$_6$-tag from a pET24-derived vector (Bornemann et al., 2014). The enzyme was purified by Cobalt-Talon affinity chromatography followed by Q-Sepharose ion-exchange chromatography (Nguyen and Pei, 2008; Ranjan et al., 2017). Purified PDF was stored in buffer A (20 mM HEPES, pH 7.5, 70 mM NH_4Cl, 30 mM KCl, 7 mM $MgCl_2$, 0.2 mM $CoCl_2$, 1 mM TCEP, and 10 % (v/v) glycerol) at -80°C. To prepare fluorescence-labeled PDF, a fusion protein comprised of PDF, a five amino-acid linker (LEGSY) and a C-terminal Mxe GyrA intein containing a chitin binding domain was overexpressed from a pTXB1 plasmid in BL21(DE3)pLysS (New England Biolabs). The fusion protein was affinity-purified on chitin resin in buffer B (20 mM HEPES at pH 7.4, 250 mM NaCl, 5 mM $CoCl_2$) (according to Impact Kit, New England Biolabs) and intein cleavage was induced by 2-mercaptoethanesulfonic acid (200 mM) overnight in buffer B without $CoCl_2$. After eluting protein from the column in buffer C (5 mM BIS-TRIS at pH 6.5, 250 mM NaCl), Bodipy-FL (Bpy) labeled peptide (CSDSK-Bpy, 2 mM) was added in 25-fold excess. The C-terminally labeled PDF(C-term) was then purified by gel filtration using a Superdex75 column in buffer D (20 mM HEPES, pH 7.5, 70 mM NH_4Cl, 30 mM KCl, 7 mM $MgCl_2$, and 10 % (v/v) glycerol) and stored in buffer D with $CoCl_2$ (0.2 mM) at -80°C.

4.1.2 RNC preparation

RNCs were prepared using a reconstituted *in vitro* translation system from *E. coli* as described (Bornemann et al., 2008). Ribosomes from *E. coli* MRE600; initiation factors IF1, IF2 and IF3; elongation factors EF-Tu, EF-Ts and EF-G; and initiator fMet-tRNA^{fMet} were prepared according to standard protocols (Cunha et al., 2013; Milon et al., 2007; Wieden et al., 2002). Total *E. coli* tRNA (Roche), was aminoacylated with a mixture of 19 amino acids plus [^{14}C]Leu (Holtkamp et al., 2015). mRNAs were prepared by *in vitro* transcription and purified by anion exchange chromatography (HiTrapQ HP, Cytiva) (Mercier et al., 2020). ICs were prepared from 70S ribosomes (1 µM), initiation factors (1.5 µM), f[^{35}S]Met-tRNA^{fMet} or f[^{3}H]Met-tRNA^{fMet} (2.5 µM), and mRNA (15 µM) at 37°C for 1 h in buffer E (50 mM TRIS, pH 7.5, 70 mM NH_4Cl, 30 mM KCl, 7 mM $MgCl_2$). Elongation was carried out in the presence of IC (0.125 µM), elongation factors (EF-Tu:

15 µM; EF-Ts: 0.02 µM; EF-G: 1 µM) and total aminoacyl-tRNA (100 µM) at 37°C for 1 h in buffer F (50 mM TRIS, pH 7.5, 70 mM NH_4Cl, 30 mM KCl, 3.5 mM $MgCl_2$, 8 mM putrescine and 0.5 mM spermidine). After completion of translation, RNCs were purified by sucrose gradient centrifugation (Bornemann et al., 2008) and stored in buffer A. RNC concentrations were determined by radioactive counting of [^{35}S] and/or [^{14}C]Leu in the nascent chain.

4.1.3 Colorimetric deformylation assay

Deformylation of the model peptide fML-pNA (Bachem, 25-1500 µM) by PDF (0.01 µM) was monitored in buffer A at 37°C (Wei and Pei, 1997). For detection, *Aeromonas* aminopeptidase (0.8 U/ml) was included to digest the deformylated ML-pNA and formation of pNA product was detected by 405 nm absorbance in a UV/Vis spectrometer (Lambda Bio+, Perkin Elmer) at 5 s time intervals.

To test potential PDF inhibitors, deformylation was carried out at a fixed concentration of fML-pNA (180 µM) in buffer A with 0.4 % DMSO. Fumimycin and its analogues were added at the reported IC_{50} value for *Sa*PDF (4 µM).

4.1.4 RNC deformylation assay

RNC deformylation was performed as described (Ranjan et al., 2017). In brief, purified ^{35}S-labeled RNCs were mixed with PDF in buffer A and incubated at 37°C. The reaction was quenched by rapid boiling followed by digestion with proteinase K (Sigma-Aldrich, 20 mg/ml) at 37°C overnight. The resulting amino acids were separated by thin-layer chromatography (TLC silica gel 60, Merck) with 3:1:1 butanol:acetic acid:water mobile phase, and a phosphorous imaging screen (imaging plate BAS-IP MS 2040, Fujifilm) was used for detection (Typhoon FLA 7000, GE Healthcare and Amersham Typhoon, Cytiva). The amounts of formylated and deformylated species were quantified by densitometry and the fraction of deformylated product was calculated. Oxidized Met and fMet, which were present in small amounts, were not included in the quantification. As reported earlier (Ranjan et al., 2017), formylated RNC substrates carrying a nascent chain with lysine in the second position were less sensitive to proteinase K digestion, resulting in formylated dipeptides that were included in the quantification. The samples of multiple-turnover time courses for DnaK75-RNC were quenched with 33% formic acid as described below for single-turnover experiments; the two quenching methods gave identical results.

To determine the multiple-turnover kinetics of deformylation, an excess of RNC was deformylated by catalytic amounts of PDF (Figure 17B). The initial velocity, V_0, was determined by linear fitting of the initial time points of deformylation time courses. After normalizing the initial velocity to the PDF concentration [PDF] and plotting it against the RNC concentration [RNC] (Figure 17C), the Michaelis-Menten equation was used for fitting.

For testing the reversibility of the reaction, TolB75-RNC (50 nM) was reacted with PDF (1 µM) for 10 min. Then, sodium formate (0.5-2 M) was added to the mixture and the reaction was continued for 30 min. Workup and analysis were performed as described above. As controls, additions of buffer A, sodium acetate (1 M), actinonin (2 mM) and actinonin together with sodium formate (2 mM and up to 2M, respectively) were tested.

4.1.5 Single-turnover deformylation kinetics

Pre-steady-state deformylation kinetics was measured using a quench-flow apparatus (KinTek) at either 37°C or 10°C. ^{35}S-labeled RNCs (10 nM) were reacted with saturating concentrations of PDF (25 µM) in buffer A and quenched with 33% formic acid. Samples were dried under vacuum at 45°C, the resulting pellets were washed by resuspension in cold 75% acetone (-20°C) and centrifuged at 13.2 x g for 15 min at 4°C. After removing the supernatant, pellets were dried under vacuum at 45°C and dissolved in buffer G (20 mM HEPES, pH 7.5, 70 mM NH_4CL, 30 mM KCl, 7 mM $MgCl_2$, 10 mM $CaCl_2$, 2 mM TCEP) with 33 mg/ml proteinase K. Digestion was carried out overnight and Met and fMet were separated on TLC and quantified as above.

Rates measured under single-turnover conditions are, in principle, dependent on a number of elemental rate constants in Figure 22. At these PDF concentrations, binding is not rate-limiting and rate constants k_1 and k_{-1} do not contribute. Because the single-turnover reaction is faster than the multiple-turnover reaction by three orders of magnitude (k_{app} = 50 s^{-1} vs. k_{cat} = 0.05 s^{-1}), steps after hydrolysis are too slow to contribute to the observed rate constant, k_{app}. Based on this simplifying assumption, k_{app} for single-turnover deformylation then reduces to Equation 1:

$$\mathrm{k_{app}} = \mathrm{k_2} + \mathrm{k_{-2}} \tag{1}$$

The end level of the reaction observed in the quench-flow experiments is obtained after the second step has reached equilibrium, but prior to any contribution by step three. This allows elemental rate constants k_2 and k_{-2} to be calculated from Equation 2:

$$\frac{[\mathrm{P}]}{[\mathrm{S}]_0} = \frac{\mathrm{k_2}}{\mathrm{k_2}+\mathrm{k_{-2}}} \tag{2}$$

where [P] and $[S]_0$ are the product concentration and initial substrate concentration, respectively.

4.1.6 PDF binding assay

Labeled PDF(C-term) was mixed with TolB75-RNC or 70S ribosomes in buffer A in a stopped-flow apparatus (SX-20MV, Applied Photophysics) at 10°C. Fluorescence was monitored using an excitation wavelength of 470 nm (SX LED 470, Applied Photophysics) and a long-pass emission filter (Schott KV550). To improve the signal-to noise ratio, 6 to 9 traces were averaged for each experiment. For dissociation experiments, RNCs or ribosomes were mixed with PDF(C-term) and incubated for 2 min to allow complex formation and deformylation prior to the experiment. Dissociation was then monitored in the stopped-flow apparatus upon rapid mixing with an equal volume of PDF solution (15 µM, after mixing) or buffer A; final concentrations of PDF(C-term) and ribosomes/RNCs after mixing were 300 nM and 420 nM, respectively. To determine the K_d for PDF and ribosomes, PDF(C-term) was mixed with increasing amounts of ribosomes and the fluorescence anisotropy was measured (FluoroMax-4, Horiba). The data were corrected for light scattering by ribosomes (ribosome-only control) and fitted to a hyperbolic function.

To determine the rate constants k_1 and k_{-1}, the time courses of binding and dissociation at different ribosome concentrations were fitted globally using KinTek Explorer software (Johnson et al., 2009a, b). The data set used for fitting was comprised of the PDF-70S binding titration and controls reflecting the extent of light scattering by ribosomes at various concentrations. The fitted rate constants describing the interaction of PDF with 70S ribosomes or RNCs at 10°C were extrapolated to 37°C as described (Equation 3 (Rudorf et al., 2014)).

$$\frac{k_i(37°\mathrm{C})}{k_{\mathrm{TolB75}}(37°\mathrm{C})} = \left(\frac{k_i(10°\mathrm{C})}{k_{\mathrm{TolB75}}(10°\mathrm{C})}\right)^{\frac{283.15\ \mathrm{K}}{310.15\ \mathrm{K}}} \qquad (3)$$

The rates of single-turnover deformylation of TolB75-RNC at 37°C and 10°C, k_{TolB75} (37°C) and k_{TolB75} (10°C) were used as references to scale other rate constants (Table 2).

4.1.7 Global fitting

Global fitting of multiple- and single-turnover experiments of TolB75-, DnaK75-, RNaseH75- and proOmpA75-RNCs was performed using KinTek Explorer software (Figure 23) to the minimal model of deformylation (Figure 22). Rate constants k_1, k_{-1}, k_2, k_{-2}, k_4, k_{-4} were fixed to values determined by individual experiments. k_5 and k_{-5} were the same for all substrates; k_5 was fixed to a rate of 200 s^{-1}. Even though formate is added to the reaction to keep the pH constant, the active species is expected to be formic acid.

The concentration of active compound was fitted during global analysis to be 0.4 µM and 2.2 µM. Standard errors were determined by linear regression following the simulation of the rate constants (Table 3).

4.1.8 Co-translational deformylation assay

A reconstituted *in vitro* translation system was used to study PDF-catalyzed co-translational deformylation. ICs were formed in buffer E with 70S ribosomes, mRNA as indicated and f[^{35}S]Met-tRNA^{fMet} for 1 h at 37 °C and purified by sucrose gradient centrifugation (Mercier et al., 2020). To start the reaction, purified ICs (50 nM) were mixed with the translation machinery and PDF (2 µM) in buffer F with CoCl2 (0.2 mM) and TCEP (1 mM). Translation was carried out in the presence of EF-Tu (15 µM), EF-G (1 µM), EF-Ts (100 nM), total aa-tRNA (100 µM) containing [^{14}C]Leu-tRNA^{Leu}, GTP (1 mM, Jena Biosciences), phosphoenolpyruvate (3 mM, Roche) and pyruvate kinase (10 µg/ml, Roche). The reaction was quenched by rapid heating, and the extent of deformylation was determined as described above. The cellular concentration of PDF was calculated from the number of PDF molecules per cell (1300) and a cell volume of 10^{-15} l (Ragusa et al., 1998).

Time courses of co-translational deformylation (Figure 24C) were fitted by exponential functions taking into account a 40 s delay prior to the slow phase using the method reported previously (Mercier et al., 2020). Delays of 35 s or 45 s yielded the same rates, indicating the robustness of the fitted values. Apparent rates were compared using a one-way ANOVA (GraphPad Prism), which indicated a significantly lower rate for TolB50 than TolB75 and TolB100 ($p = 0.013$ and 0.0001, respectively), but no significant difference for TolB75 and TolB100 ($p = 0.20$).

4.1.9 Translation time courses

To monitor the progress of translation, translation products were analyzed as described previously (Mercier et al., 2020). ICs were formed with f[^{35}S]Met-tRNA^{fMet} or Bpy-[^{3}H]Met-tRNA^{fMet} as described above. Translation was carried out from purified initiation complex at the same conditions as in the co-translational deformylation assay. The translation reaction was stopped with ammonia (2%) at specific time points and the peptide was released from the RNC by incubating at 37°C. Afterwards, samples were concentrated by evaporation and separated by TRIS-Tricine-SDS-PAGE. Peptides were detected using either radioactive or fluorescence detection (Typhoon FLA 7000, GE Healthcare and Amersham Typhoon, Cytiva). The relative amount of full-length product was determined by densitometry and traces were fitted to a delay followed by a one-exponential increase (Equation 4). y_0 is the starting fluorescence, x_0 the delay time, A the amplitude of the fluorescence increase and τ the transition time. From the delay, the transition time and the nascent chain length N, the translation rate was calculated (Equation 5, GraphPad Prism).

$$f(x) = \begin{cases} y_0, & x < x_0 \\ y_0 + A - A \cdot \exp(-\frac{1}{\tau} \cdot (x - x_0)), & x \geq x_0 \end{cases} \tag{4}$$

$$\text{Translation rate} = \frac{N}{x_0 + \tau} \tag{5}$$

4.2 Co-translational folding

4.2.1 SecYEG purification and labeling

SecYEG was expressed in *E. coli* Lemo21(DE3) cells (New England Biolabs) with an N-terminal His_6-tag on SecE from a pTRC99a plasmid and purified according to published protocols (Draycheva et al., 2016; Ge et al., 2014). Cell lysate was cleared for 20 min at 30,000 x*g* and cell membranes were collected for 120 min at 150,000 x*g*. To solubilize the protein, the membrane fraction was dissolved in buffer H (20 mM HEPES, pH 7.5, 1 M NaCl, 5 mM MgCl2, 20 mM imidazole, 1% n-dodecyl-β-D-maltoside (DDM), 10% glycerol). SecYEG was purified via nickel-affinity chromatography (HisTrap FF, Cytiva) followed by cation exchange chromatography (HiTrap SP HP, Cytiva) and stored in buffer D with DDM (0.03 %). SecY mutants SecY(T179C) and SecY(T298C) were previously prepared in the department by site directed mutagenesis from Cys-less SecYEG (Draycheva et al., 2016; Ge et al., 2014; Mercier et al., 2021). Purification was carried out as for the wild-type SecYEG complex but stored in buffer I (20 mM HEPES, 150 mM KCl, 10 % glycerol, 0.03 % DDM).

For fluorescence labeling of the translocon, purified SecY(179C)EG or SecY(298C)EG, was incubated with excess Atto647N-maleimide (Atto-Tec) for 2 h at room temperature (Draycheva et al., 2016; Ge et al., 2014). The reaction was quenched with DTT (5 mM) and labeled protein was purified by gel filtration chromatography (Sephadex G-25, GE Healthcare).

4.2.2 Nanodisc preparation

MSP1D1 was used as scaffold protein for nanodiscs and expressed in *E. coli* BL21(DE3). Purification was carried out by nickel-affinity chromatography (HisTrap FF, Cytiva) in the presence of Triton-X (1 %) as described previously (Draycheva et al., 2016). The purified protein was stored in buffer D with DDM (0.03 %).

For the assembly of nanodiscs (Draycheva et al., 2016; Ge et al., 2014), SecYEG (or labeled mutants) was incubated with MSP1D1 and *E. coli* total lipids (Avanti Polar Lipids) in a ratio of 1:2:30 for 1 h on ice in buffer D with DDM (0.5 %). Formation of nanodiscs was initiated by removing DDM with BioBeads SM-2 (BIO-RAD). Afterwards, nanodiscs were purified by size exclusion chromatography (Superdex 200 10/300 GrL, GE Healthcare) in buffer J (40 mM HEPES, pH 7.5, 140 mM NH_4Cl, 60 mM KCl, 14 mM $MgCl_2$) with glycerol (10 %) and stored in buffer D.

4.2.3 Bpy-Lys-tRNA^{Lys} purification

BOF-Lys-tRNA was purified following established protocols with a few changes (Crowley et al., 1993; Mittelstaet et al., 2013; Woolhead et al., 2004). First, tRNA^{Lys} was purified from *E. coli* total tRNA (Roche) by two rounds of hydrophobic-interaction chromatography (Sepharose 4B and Phenyl-Sepharose, GE Healthcare) followed by anion exchange chromatography (DEAE Toyopearl 650M, Tosoh Bioscience). Then, the tRNA was aminoacylated with [^{14}C]Lys using S100 extract (5 %) in buffer J with DTT (2 mM) and ATP (3 mM) for 30 min at 37 °C. Purification was performed by phenol extraction followed by reversed phase chromatography (LiChrospher WP300 RP18, Merck) in buffer K (20 mM NH_4OAc, 10 mM $MgCl_2$, 400 mM NaCl) with EtOH (5-15 %). Lys-tRNA^{Lys} (40 µM) was then labeled with Bpy-succinimidyl ester (4 mM) in buffer L (1 M K/PO_4, pH 7). To initiate the reaction, the ε-NH_2 of lysine was deprotonated by increasing the pH to 12 with KOH (47 µM) and the reaction was carried out for 25 s before quenching with AcOH (47 µM). Free dye was removed by repeated ethanol precipitation before Bpy-Lys-tRNA^{Lys} was purified by reversed-phase chromatography (LiChrospher WP300 RP18, Merck) in buffer K with 5-40 % EtOH and stored in H_2O.

For calculating the length of the nascent chain including compacted α-helices (Figure 27A), a height of 3.5 Å was assumed for extended amino acids while 1.5 Å were assumed for amino acids in a helical conformation. The length of the peptide exit tunnel is 118 Å and the translocon adds 57 Å (Frauenfeld et al., 2011).

4.2.4 Translation of EmrD with and without BOF-Lys incorporation

ICs were formed with f[^{3}H]Met-tRNA^{fMet}, Bpy-[^{3}H]Met-tRNA^{fMet} or A655-[^{3}H]Met-tRNA^{fMet} and purified as above. *In vitro* synthesis of N-terminally labeled EmrD variants was performed with purified IC (25 nM), EF-Tu (15 µM), EF-G (2 µM) and total aa-tRNA (40 µM) containing [^{14}C]Leu-tRNA^{Leu} (2.7 µM) in buffer F. For the incorporation of Bpy-Lys, site-directed mutagenesis was applied to mutate the lysine in position 2 of EmrD to arginine (CGC codon) and a single lysine codon (AAA) was inserted at amino acid position 67, 70 or 71.5. For translation, different concentrations of elongation factors and tRNA were tested. Optimized conditions are EF-Tu (25 µM), EF-G (2 µM), total aa-tRNA without Lys-tRNA^{Lys} (80 µM) and Bpy-Lys-tRNA^{Lys} (0.3 µM). Translation time courses were recorded as described above; after the release of the peptide, samples containing Bpy-Lys-tRNA^{Lys} were additionally treated with RNaseA (100 µg/mL) at 37°C for 30 min to remove remaining peptidyl-tRNA. Analysis of translation time courses was performed using Equations 4 and 5 as described above.

4.2.5 Co-translational folding assay

Co-translational folding was monitored by FRET measurements similar to published methods (Mercier et al., 2020). Translation in buffer F was started by rapidly mixing ICs with a solution of translation components and SecYEG nanodiscs (500 nM) at 37°C in a stopped-flow apparatus (SX-20MV, Applied Photophysics). Fluorophores were chosen as indicated. Donor excitation was performed at 470 nm (SX LED 470, Applied Photophysics) and acceptor fluorescence was detected using a long-pass filter RG645 and a red-sensitive photomultiplier tube (R2228, Applied Photophysics). 5-6 replicates were averaged for each experiment to reduce the signal-to-noise ratio. Fluorescence changes were fitted to a delay followed by a two-exponential increase (Equation 6, GraphPad Prism). The transition time of the fluorescence signal change is defined as in Equation 7.

$$f(x) = \begin{cases} y_0, \ x < x_0 \\ y_0 + A_1 - A_1 \cdot \exp(-\frac{1}{\tau_1} \cdot (x - x_0)) + A_2 - A_2 \cdot \exp(-\frac{1}{\tau_2} \cdot (x - x_0)), \ x \geq x_0 \end{cases} \tag{6}$$

$$\text{Transition time} = x_0 + \tau_1 \tag{7}$$

5 References

Adamian, L., and Liang, J. (2002). Interhelical hydrogen bonds and spatial motifs in membrane proteins: polar clamps and serine zippers. Proteins *47*, 209-218.

Agirrezabala, X., Samatova, E., Macher, M., Liutkute, M., Maiti, M., Gil-Carton, D., Novacek, J., Valle, M., and Rodnina, M.V. (2022). A switch from alpha-helical to beta-strand conformation during co-translational protein folding. EMBO J. *41*, e109175.

Akbar, S., Bhakta, S., and Sengupta, J. (2021). Structural insights into the interplay of protein biogenesis factors with the 70S ribosome. Structure *29*, 755-767 e754.

Apfel, C., Banner, D.W., Bur, D., Dietz, M., Hirata, T., Hubschwerlen, C., Locher, H., Page, M.G., Pirson, W., Rosse, G.*, et al.* (2000). Hydroxamic acid derivatives as potent peptide deformylase inhibitors and antibacterial agents. J. Med. Chem. *43*, 2324-2331.

Apfel, C.M., Locher, H., Evers, S., Takacs, B., Hubschwerlen, C., Pirson, W., Page, M.G., and Keck, W. (2001). Peptide deformylase as an antibacterial drug target: target validation and resistance development. Antimicrob. Agents Chemother. *45*, 1058-1064.

Ariosa, A., Lee, J.H., Wang, S., Saraogi, I., and Shan, S.O. (2015). Regulation by a chaperone improves substrate selectivity during cotranslational protein targeting. Proc. Natl. Acad. Sci. U. S. A. *112*, E3169-3178.

Baker, J., Wright, S.H., and Tama, F. (2012). Simulations of substrate transport in the multidrug transporter EmrD. Proteins *80*, 1620-1632.

Baldwin, E.T., Harris, M.S., Yem, A.W., Wolfe, C.L., Vosters, A.F., Curry, K.A., Murray, R.W., Bock, J.H., Marshall, V.P., Cialdella, J.I.*, et al.* (2002). Crystal structure of type II peptide deformylase from Staphylococcus aureus. J. Biol. Chem. *277*, 31163-31171.

Ball, L.A., and Kaesberg, P. (1973). Cleavage of the N-terminal formylmethionine residue from a bacteriophage coat protein in vitro. J. Mol. Biol. *79*, 531-537.

Bano-Polo, M., Baeza-Delgado, C., Tamborero, S., Hazel, A., Grau, B., Nilsson, I., Whitley, P., Gumbart, J.C., von Heijne, G., and Mingarro, I. (2018). Transmembrane but not soluble helices fold inside the ribosome tunnel. Nat. Commun. *9*, 5246.

Becker, A., Schlichting, I., Kabsch, W., Groche, D., Schultz, S., and Wagner, A.F. (1998). Iron center, substrate recognition and mechanism of peptide deformylase. Nat. Struct. Biol. *5*, 1053-1058.

Belardinelli, R., Sharma, H., Peske, F., Wintermeyer, W., and Rodnina, M.V. (2016). Translocation as continuous movement through the ribosome. RNA Biol. *13*, 1197-1203.

Berg, M.D., and Brandl, C.J. (2021). Transfer RNAs: diversity in form and function. RNA Biol. *18*, 316-339.

Beringer, M., and Rodnina, M.V. (2007). The ribosomal peptidyl transferase. Mol. Cell *26*, 311-321.

Bhakta, S., Akbar, S., and Sengupta, J. (2019). Cryo-EM Structures Reveal Relocalization of MetAP in the Presence of Other Protein Biogenesis Factors at the Ribosomal Tunnel Exit. J. Mol. Biol. *431*, 1426-1439.

Bienvenut, W.V., Giglione, C., and Meinnel, T. (2015). Proteome-wide analysis of the amino terminal status of Escherichia coli proteins at the steady-state and upon deformylation inhibition. Proteomics *15*, 2503-2518.

Bingel-Erlenmeyer, R., Kohler, R., Kramer, G., Sandikci, A., Antolic, S., Maier, T., Schaffitzel, C., Wiedmann, B., Bukau, B., and Ban, N. (2008). A peptide deformylase-ribosome complex reveals mechanism of nascent chain processing. Nature *452*, 108-111.

Bischoff, L., Wickles, S., Berninghausen, O., van der Sluis, E.O., and Beckmann, R. (2014). Visualization of a polytopic membrane protein during SecY-mediated membrane insertion. Nat. Commun. *5*, 4103.

Bitran, A., Jacobs, W.M., Zhai, X., and Shakhnovich, E. (2020). Cotranslational folding allows misfolding-prone proteins to circumvent deep kinetic traps. Proc. Natl. Acad. Sci. U. S. A. *117*, 1485-1495.

Bornemann, T., Holtkamp, W., and Wintermeyer, W. (2014). Interplay between trigger factor and other protein biogenesis factors on the ribosome. Nat. Commun. *5*, 4180.

Bornemann, T., Jockel, J., Rodnina, M.V., and Wintermeyer, W. (2008). Signal sequence-independent membrane targeting of ribosomes containing short nascent peptides within the exit tunnel. Nature Struct. Mol. Biol. *15*, 494-499.

Bremer, H., and Dennis, P.P. (2008). Modulation of Chemical Composition and Other Parameters of the Cell at Different Exponential Growth Rates. EcoSal Plus *3*.

Breyton, C., Haase, W., Rapoport, T.A., Kuhlbrandt, W., and Collinson, I. (2002). Three-dimensional structure of the bacterial protein-translocation complex SecYEG. Nature *418*, 662-665.

Buskiewicz, I., Deuerling, E., Gu, S.Q., Jockel, J., Rodnina, M.V., Bukau, B., and Wintermeyer, W. (2004). Trigger factor binds to ribosome-signal-recognition particle (SRP) complexes and is excluded by binding of the SRP receptor. Proc. Natl. Acad. Sci. U. S. A. *101*, 7902-7906.

Cao, G., Kuhn, A., and Dalbey, R.E. (1995). The translocation of negatively charged residues across the membrane is driven by the electrochemical potential: evidence for an electrophoresis-like membrane transfer mechanism. EMBO J. *14*, 866-875.

Carbone, C.E., Loveland, A.B., Gamper, H.B., Jr., Hou, Y.M., Demo, G., and Korostelev, A.A. (2021). Time-resolved cryo-EM visualizes ribosomal translocation with EF-G and GTP. Nat. Commun. *12*, 7236.

Cassaignau, A.M.E., Cabrita, L.D., and Christodoulou, J. (2020). How Does the Ribosome Fold the Proteome? Annu. Rev. Biochem. *89*, 389-415.

Chan, M.K., Gong, W., Rajagopalan, P.T., Hao, B., Tsai, C.M., and Pei, D. (1997). Crystal structure of the Escherichia coli peptide deformylase. Biochemistry *36*, 13904-13909.

Chen, D.Z., Patel, D.V., Hackbarth, C.J., Wang, W., Dreyer, G., Young, D.C., Margolis, P.S., Wu, C., Ni, Z.J., Trias, J.*, et al.* (2000). Actinonin, a naturally occurring antibacterial agent, is a potent deformylase inhibitor. Biochemistry *39*, 1256-1262.

Clements, J.M., Beckett, R.P., Brown, A., Catlin, G., Lobell, M., Palan, S., Thomas, W., Whittaker, M., Wood, S., Salama, S.*, et al.* (2001). Antibiotic activity and characterization of BB-3497, a novel peptide deformylase inhibitor. Antimicrob. Agents Chemother. *45*, 563-570.

Crowley, K.S., Reinhart, G.D., and Johnson, A.E. (1993). The signal sequence moves through a ribosomal tunnel into a noncytoplasmic aqueous environment at the ER membrane early in translocation. Cell *73*, 1101-1115.

Culver, G.M. (2001). Meanderings of the mRNA through the ribosome. Structure *9*, 751-758.

Cunha, C.E., Belardinelli, R., Peske, F., Holtkamp, W., Wintermeyer, W., and Rodnina, M.V. (2013). Dual use of GTP hydrolysis by elongation factor G on the ribosome. Translation (Austin) *1*, e24315.

Cymer, F., von Heijne, G., and White, S.H. (2015). Mechanisms of Integral Membrane Protein Insertion and Folding. J. Mol. Biol. *427*, 999-1022.

Dao Duc, K., Batra, S.S., Bhattacharya, N., Cate, J.H.D., and Song, Y.S. (2019). Differences in the path to exit the ribosome across the three domains of life. Nucleic Acids Res. *47*, 4198-4210.

Deckert, A., Cassaignau, A.M.E., Wang, X., Wlodarski, T., Chan, S.H.S., Waudby, C.A., Kirkpatrick, J.P., Vendruscolo, M., Cabrita, L.D., and Christodoulou, J. (2021). Common sequence motifs of nascent chains engage the ribosome surface and trigger factor. Proc. Natl. Acad. Sci. U. S. A. *118*.

Demeshkina, N., Jenner, L., Westhof, E., Yusupov, M., and Yusupova, G. (2013). New structural insights into the decoding mechanism: Translation infidelity via a G.U pair with Watson-Crick geometry. FEBS Lett. *587*, 1848-1857.

Denks, K., Sliwinski, N., Erichsen, V., Borodkina, B., Origi, A., and Koch, H.G. (2017). The signal recognition particle contacts uL23 and scans substrate translation inside the ribosomal tunnel. Nat. Microbiol. *2*, 16265.

Dowhan, W., Vitrac, H., and Bogdanov, M. (2019). Lipid-Assisted Membrane Protein Folding and Topogenesis. Protein J. *38*, 274-288.

Draycheva, A., Bornemann, T., Ryazanov, S., Lakomek, N.A., and Wintermeyer, W. (2016). The bacterial SRP receptor, FtsY, is activated on binding to the translocon. Mol. Microbiol. *102*, 152-167.

Draycheva, A., Lee, S., and Wintermeyer, W. (2018). Cotranslational protein targeting to the membrane: Nascent-chain transfer in a quaternary complex formed at the translocon. Sci. Rep. *8*, 9922.

Egea, P.F., and Stroud, R.M. (2010). Lateral opening of a translocon upon entry of protein suggests the mechanism of insertion into membranes. Proc. Natl. Acad. Sci. U. S. A. *107*, 17182-17187.

Eisner, G., Moser, M., Schafer, U., Beck, K., and Muller, M. (2006). Alternate recruitment of signal recognition particle and trigger factor to the signal sequence of a growing nascent polypeptide. J. Biol. Chem. *281*, 7172-7179.

Engelman, D.M., Chen, Y., Chin, C.N., Curran, A.R., Dixon, A.M., Dupuy, A.D., Lee, A.S., Lehnert, U., Matthews, E.E., Reshetnyak, Y.K*., et al.* (2003). Membrane protein folding: beyond the two stage model. FEBS Lett. *555*, 122-125.

Escobar-Alvarez, S., Gardner, J., Sheth, A., Manfredi, G., Yang, G., Ouerfelli, O., Heaney, M.L., and Scheinberg, D.A. (2010). Inhibition of human peptide deformylase disrupts mitochondrial function. Mol. Cell. Biol. *30*, 5099-5109.

Escobar-Alvarez, S., Goldgur, Y., Yang, G., Ouerfelli, O., Li, Y., and Scheinberg, D.A. (2009). Structure and activity of human mitochondrial peptide deformylase, a novel cancer target. J. Mol. Biol. *387*, 1211-1228.

Ferbitz, L., Maier, T., Patzelt, H., Bukau, B., Deuerling, E., and Ban, N. (2004). Trigger factor in complex with the ribosome forms a molecular cradle for nascent proteins. Nature *431*, 590-596.

Frauenfeld, J., Gumbart, J., Sluis, E.O., Funes, S., Gartmann, M., Beatrix, B., Mielke, T., Berninghausen, O., Becker, T., Schulten, K*., et al.* (2011). Cryo-EM structure of the ribosome-SecYE complex in the membrane environment. Nat. Struct. Mol. Biol. *18*, 614-621.

Frottin, F., Martinez, A., Peynot, P., Mitra, S., Holz, R.C., Giglione, C., and Meinnel, T. (2006). The proteomics of N-terminal methionine cleavage. Mol. Cell. Proteomics *5*, 2336-2349.

Gao, N., Zavialov, A.V., Li, W., Sengupta, J., Valle, M., Gursky, R.P., Ehrenberg, M., and Frank, J. (2005). Mechanism for the disassembly of the posttermination complex inferred from cryo-EM studies. Mol. Cell *18*, 663-674.

Ge, Y., Draycheva, A., Bornemann, T., Rodnina, M.V., and Wintermeyer, W. (2014). Lateral opening of the bacterial translocon on ribosome binding and signal peptide insertion. Nat. Commun. *5*, 5263.

Giglione, C., Boularot, A., and Meinnel, T. (2004). Protein N-terminal methionine excision. Cell Mol. Life Sci. *61*, 1455-1474.

Giglione, C., Fieulaine, S., and Meinnel, T. (2015). N-terminal protein modifications: Bringing back into play the ribosome. Biochimie *114*, 134-146.

Giglione, C., and Meinnel, T. (2001). Resistance to anti-peptide deformylase drugs. Expert Opin. Ther. Targets *5*, 415-418.

Giglione, C., Serero, A., Pierre, M., Boisson, B., and Meinnel, T. (2000). Identification of eukaryotic peptide deformylases reveals universality of N-terminal protein processing mechanisms. EMBO J. *19*, 5916-5929.

Gokhale, K.M., and Telvekar, V.N. (2021). Novel peptidomimetic peptide deformylase (PDF) inhibitors of Mycobacterium tuberculosis. Chem. Biol. Drug Des. *97*, 148-156.

Gratkowski, H., Lear, J.D., and DeGrado, W.F. (2001). Polar side chains drive the association of model transmembrane peptides. Proc. Natl. Acad. Sci. U. S. A. *98*, 880-885.

Gu, S.Q., Peske, F., Wieden, H.J., Rodnina, M.V., and Wintermeyer, W. (2003). The signal recognition particle binds to protein L23 at the peptide exit of the Escherichia coli ribosome. RNA *9*, 566-573.

Gualerzi, C.O., and Pon, C.L. (2015). Initiation of mRNA translation in bacteria: structural and dynamic aspects. Cell Mol. Life Sci. *72*, 4341-4367.

Guillon, J.M., Mechulam, Y., Schmitter, J.M., Blanquet, S., and Fayat, G. (1992). Disruption of the gene for Met-tRNA(fMet) formyltransferase severely impairs growth of Escherichia coli. J. Bacteriol. *174*, 4294-4301.

Guilloteau, J.P., Mathieu, M., Giglione, C., Blanc, V., Dupuy, A., Chevrier, M., Gil, P., Famechon, A., Meinnel, T., and Mikol, V. (2002). The crystal structures of four peptide deformylases bound to the antibiotic actinonin reveal two distinct types: a platform for the structure-based design of antibacterial agents. J. Mol. Biol. *320*, 951-962.

Guo, X.C., Ravi Rajagopalan, P.T., and Pei, D. (1999). A direct spectrophotometric assay for peptide deformylase. Anal. Biochem. *273*, 298-304.

Hainzl, T., Huang, S., Merilainen, G., Brannstrom, K., and Sauer-Eriksson, A.E. (2011). Structural basis of signal-sequence recognition by the signal recognition particle. Nat. Struct. Mol. Biol. *18*, 389-391.

Halic, M., Blau, M., Becker, T., Mielke, T., Pool, M.R., Wild, K., Sinning, I., and Beckmann, R. (2006). Following the signal sequence from ribosomal tunnel exit to signal recognition particle. Nature *444*, 507-511.

Henzler-Wildman, K., and Kern, D. (2007). Dynamic personalities of proteins. Nature *450*, 964-972.

Hizlan, D., Robson, A., Whitehouse, S., Gold, V.A., Vonck, J., Mills, D., Kuhlbrandt, W., and Collinson, I. (2012). Structure of the SecY complex unlocked by a preprotein mimic. Cell Rep. *1*, 21-28.

Holtkamp, W., Kokic, G., Jager, M., Mittelstaet, J., Komar, A.A., and Rodnina, M.V. (2015). Cotranslational protein folding on the ribosome monitored in real time. Science *350*, 1104-1107.

Holtkamp, W., Lee, S., Bornemann, T., Senyushkina, T., Rodnina, M.V., and Wintermeyer, W. (2012). Dynamic switch of the signal recognition particle from scanning to targeting. Nat. Struct. Mol. Biol. *19*, 1332-1337.

Hou, B., Lin, P.J., and Johnson, A.E. (2012). Membrane protein TM segments are retained at the translocon during integration until the nascent chain cues FRET-detected release into bulk lipid. Mol. Cell *48*, 398-408.

References

Housman, D., Gillespie, D., and Lodish, H.F. (1972). Removal of formyl-methionine residue from nascent bacteriophage f2 protein. J. Mol. Biol. *65*, 163-166.

Hu, Y.J., Wei, Y., Zhou, Y., Rajagopalan, P.T., and Pei, D. (1999). Determination of substrate specificity for peptide deformylase through the screening of a combinatorial peptide library. Biochemistry *38*, 643-650.

Jain, R., Hao, B., Liu, R.P., and Chan, M.K. (2005). Structures of E. coli peptide deformylase bound to formate: insight into the preference for Fe2+ over Zn2+ as the active site metal. J. Am. Chem. Soc. *127*, 4558-4559.

Jefferson, R.E., Min, D., Corin, K., Wang, J.Y., and Bowie, J.U. (2018). Applications of Single-Molecule Methods to Membrane Protein Folding Studies. J. Mol. Biol. *430*, 424-437.

Johnson, K.A., Simpson, Z.B., and Blom, T. (2009a). FitSpace explorer: an algorithm to evaluate multidimensional parameter space in fitting kinetic data. Anal. Biochem. *387*, 30-41.

Johnson, K.A., Simpson, Z.B., and Blom, T. (2009b). Global kinetic explorer: a new computer program for dynamic simulation and fitting of kinetic data. Anal. Biochem. *387*, 20-29.

Jomaa, A., Boehringer, D., Leibundgut, M., and Ban, N. (2016). Structures of the E. coli translating ribosome with SRP and its receptor and with the translocon. Nat. Commun. *7*, 10471.

Jomaa, A., Fu, Y.H., Boehringer, D., Leibundgut, M., Shan, S.O., and Ban, N. (2017). Structure of the quaternary complex between SRP, SR, and translocon bound to the translating ribosome. Nat. Commun. *8*, 15470.

Kaiser, C.M., Goldman, D.H., Chodera, J.D., Tinoco, I., Jr., and Bustamante, C. (2011). The ribosome modulates nascent protein folding. Science *334*, 1723-1727.

Kim, S.J., and Skach, W.R. (2012). Two-step insertion at the SecY translocon. Nat. Struct. Mol. Biol. *19*, 975-977.

Kohanski, M.A., Dwyer, D.J., and Collins, J.J. (2010). How antibiotics kill bacteria: from targets to networks. Nature Reviews Microbiology *8*, 423-435.

Koubek, J., Schmitt, J., Galmozzi, C.V., and Kramer, G. (2021). Mechanisms of Cotranslational Protein Maturation in Bacteria. Front. Mol. Biosci. *8*, 689755.

Kramer, G., Boehringer, D., Ban, N., and Bukau, B. (2009). The ribosome as a platform for co-translational processing, folding and targeting of newly synthesized proteins. Nat. Struct. Mol. Biol. *16*, 589-597.

Kramer, G., Rauch, T., Rist, W., Vorderwulbecke, S., Patzelt, H., Schulze-Specking, A., Ban, N., Deuerling, E., and Bukau, B. (2002). L23 protein functions as a chaperone docking site on the ribosome. Nature *419*, 171-174.

Kristensen, O., and Gajhede, M. (2003). Chaperone binding at the ribosomal exit tunnel. Structure *11*, 1547-1556.

Kudva, R., Tian, P., Pardo-Avila, F., Carroni, M., Best, R.B., Bernstein, H.D., and von Heijne, G. (2018). The shape of the bacterial ribosome exit tunnel affects cotranslational protein folding. Elife *7*.

Kuhn, A., Koch, H.G., and Dalbey, R.E. (2017). Targeting and Insertion of Membrane Proteins. EcoSal Plus *7*.

Kvietkauskas, J. (2021). Transmembrane protein partitioning from the SecYEG translocon to the lipid bilayer. In Physical Biochemistry, MPI for multidisciplinary sciences (Georg August University Göttingen).

Kwon, Y.J., Sohn, M.J., Zheng, C.J., and Kim, W.G. (2007). Fumimycin: a peptide deformylase inhibitor with an unusual skeleton produced by Aspergillus fumisynnematus. Org. Lett. *9*, 2449-2451.

Lakowicz, J.R. (2006). Principles of Fluorescence Spectroscopy, Third Edition edn (Baltimore, USA: Springer).

Laursen, B.S., Sorensen, H.P., Mortensen, K.K., and Sperling-Petersen, H.U. (2005). Initiation of protein synthesis in bacteria. Microbiol. Mol. Biol. Rev. *69*, 101-123.

Law, C.J., Maloney, P.C., and Wang, D.N. (2008). Ins and outs of major facilitator superfamily antiporters. Annu. Rev. Microbiol. *62*, 289-305.

Lazennec, C., and Meinnel, T. (1997). Formate dehydrogenase-coupled spectrophotometric assay of peptide deformylase. Anal. Biochem. *244*, 180-182.

Lee, M.D., Antczak, C., Li, Y.M., Sirotnak, F.M., Bornmann, W.G., and Scheinberg, D.A. (2003). A new human peptide deformylase inhibitable by actinonin. Biochemical and Biophysical Research Communications *312*, 309-315.

References

Lee, M.D., She, Y., Soskis, M.J., Borella, C.P., Gardner, J.R., Hayes, P.A., Dy, B.M., Heaney, M.L., Philips, M.R., Bornmann, W.G.*, et al.* (2004). Human mitochondrial peptide deformylase, a new anticancer target of actinonin-based antibiotics. J. Clin. Invest. *114*, 1107-1116.

Lill, R., Crooke, E., Guthrie, B., and Wickner, W. (1988). The "trigger factor cycle" includes ribosomes, presecretory proteins, and the plasma membrane. Cell *54*, 1013-1018.

Liutkute, M., Maiti, M., Samatova, E., Enderlein, J., and Rodnina, M.V. (2020a). Gradual compaction of the nascent peptide during cotranslational folding on the ribosome. Elife *9*.

Liutkute, M., Samatova, E., and Rodnina, M.V. (2020b). Cotranslational Folding of Proteins on the Ribosome. Biomolecules *10*.

Lu, J., Robinson, J.M., Edwards, D., and Deutsch, C. (2001). T1-T1 interactions occur in ER membranes while nascent Kv peptides are still attached to ribosomes. Biochemistry *40*, 10934-10946.

Makhoul, C.H., and Trifonov, E.N. (2002). Distribution of rare triplets along mRNA and their relation to protein folding. J. Biomol. Struct. Dyn. *20*, 413-420.

Margolis, P., Hackbarth, C., Lopez, S., Maniar, M., Wang, W., Yuan, Z., White, R., and Trias, J. (2001). Resistance of Streptococcus pneumoniae to deformylase inhibitors is due to mutations in defB. Antimicrob. Agents Chemother. *45*, 2432-2435.

Margolis, P.S., Hackbarth, C.J., Young, D.C., Wang, W., Chen, D., Yuan, Z., White, R., and Trias, J. (2000). Peptide deformylase in Staphylococcus aureus: resistance to inhibition is mediated by mutations in the formyltransferase gene. Antimicrob. Agents Chemother. *44*, 1825-1831.

Martoglio, B., Hofmann, M.W., Brunner, J., and Dobberstein, B. (1995). The protein-conducting channel in the membrane of the endoplasmic reticulum is open laterally toward the lipid bilayer. Cell *81*, 207-214.

Marx, D.C., and Fleming, K.G. (2021). Local Bilayer Hydrophobicity Modulates Membrane Protein Stability. J. Am. Chem. Soc. *143*, 764-772.

Mazel, D., Pochet, S., and Marliere, P. (1994). Genetic characterization of polypeptide deformylase, a distinctive enzyme of eubacterial translation. EMBO J. *13*, 914-923.

Meinnel, T., and Blanquet, S. (1995). Enzymatic properties of Escherichia coli peptide deformylase. J. Bacteriol. *177*, 1883-1887.

Meinnel, T., Lazennec, C., and Blanquet, S. (1995). Mapping of the active site zinc ligands of peptide deformylase. J. Mol. Biol. *254*, 175-183.

Meinnel, T., Lazennec, C., Villoing, S., and Blanquet, S. (1997). Structure-function relationships within the peptide deformylase family. Evidence for a conserved architecture of the active site involving three conserved motifs and a metal ion. J. Mol. Biol. *267*, 749-761.

Melnikov, S., Ben-Shem, A., Garreau de Loubresse, N., Jenner, L., Yusupova, G., and Yusupov, M. (2012). One core, two shells: bacterial and eukaryotic ribosomes. Nat. Struct. Mol. Biol. *19*, 560-567.

Mercier, E., Holtkamp, W., Rodnina, M.V., and Wintermeyer, W. (2017). Signal recognition particle binds to translating ribosomes before emergence of a signal anchor sequence. Nucleic Acids Res. *45*, 11858-11866.

Mercier, E., and Rodnina, M.V. (2018). Co-Translational Folding Trajectory of the HemK Helical Domain. Biochemistry *57*, 3460-3464.

Mercier, E., Wang, X., Bogeholz, L.A.K., Wintermeyer, W., and Rodnina, M.V. (2022). Cotranslational Biogenesis of Membrane Proteins in Bacteria. Front. Mol. Biosci. *9*, 871121.

Mercier, E., Wang, X.L., Maiti, M., Wintermeyer, W., and Rodnina, M.V. (2021). Lateral gate dynamics of the bacterial translocon during cotranslational membrane protein insertion. Proc. Natl. Acad. Sci. U. S. A. *118*.

Mercier, E., Wintermeyer, W., and Rodnina, M.V. (2020). Co-translational insertion and topogenesis of bacterial membrane proteins monitored in real time. EMBO J. *39*, e104054.

Milon, P., Konevega, A.L., Peske, F., Fabbretti, A., Gualerzi, C.O., and Rodnina, M.V. (2007). Transient kinetics, fluorescence, and FRET in studies of initiation of translation in bacteria. Methods Enzymol. *430*, 1-30.

Milon, P., Maracci, C., Filonava, L., Gualerzi, C.O., and Rodnina, M.V. (2012). Real-time assembly landscape of bacterial 30S translation initiation complex. Nat. Struct. Mol. Biol. *19*, 609-615.

Milon, P., and Rodnina, M.V. (2012). Kinetic control of translation initiation in bacteria. Crit. Rev. Biochem. Mol. Biol. *47*, 334-348.

Mittelstaet, J., Konevega, A.L., and Rodnina, M.V. (2013). A kinetic safety gate controlling the delivery of unnatural amino acids to the ribosome. J. Am. Chem. Soc. *135*, 17031-17038.

References

Mohammad, F., Woolstenhulme, C.J., Green, R., and Buskirk, A.R. (2016). Clarifying the Translational Pausing Landscape in Bacteria by Ribosome Profiling. Cell Rep. *14*, 686-694.

Naroditskaya, V., Schlosser, M.J., Fang, N.Y., and Lewis, K. (1993). An E. coli gene emrD is involved in adaptation to low energy shock. Biochem. Biophys. Res. Commun. *196*, 803-809.

Nguyen, K.T., Hu, X., Colton, C., Chakrabarti, R., Zhu, M.X., and Pei, D. (2003). Characterization of a human peptide deformylase: implications for antibacterial drug design. Biochemistry *42*, 9952-9958.

Nguyen, K.T., and Pei, D. (2008). High-throughput screening of peptide deformylase inhibitors. Methods Mol. Med. *142*, 117-130.

Nicolaus, F., Ibrahimi, F., den Besten, A., and von Heijne, G. (2022). Upstream charged and hydrophobic residues impact the timing of membrane insertion of transmembrane helices. FEBS Lett. *596*, 1004-1012.

Nicolaus, F., Metola, A., Mermans, D., Liljenstrom, A., Krc, A., Abdullahi, S.M., Zimmer, M., Miller Iii, T.F., and von Heijne, G. (2021). Residue-by-residue analysis of cotranslational membrane protein integration in vivo. Elife *10*.

Nikaido, H. (2009). Multidrug resistance in bacteria. Annu. Rev. Biochem. *78*, 119-146.

Nilsson, O.B., Hedman, R., Marino, J., Wickles, S., Bischoff, L., Johansson, M., Muller-Lucks, A., Trovato, F., Puglisi, J.D., O'Brien, E.P.*, et al.* (2015). Cotranslational Protein Folding inside the Ribosome Exit Tunnel. Cell Rep. *12*, 1533-1540.

Nilsson, O.B., Nickson, A.A., Hollins, J.J., Wickles, S., Steward, A., Beckmann, R., von Heijne, G., and Clarke, J. (2017). Cotranslational folding of spectrin domains via partially structured states. Nat. Struct. Mol. Biol. *24*, 221-225.

Nishino, K., and Yamaguchi, A. (2001). Analysis of a complete library of putative drug transporter genes in Escherichia coli. J. Bacteriol. *183*, 5803-5812.

Noriega, T.R., Tsai, A., Elvekrog, M.M., Petrov, A., Neher, S.B., Chen, J., Bradshaw, N., Puglisi, J.D., and Walter, P. (2014). Signal recognition particle-ribosome binding is sensitive to nascent chain length. J. Biol. Chem. *289*, 19294-19305.

O'Brien, E.P., Vendruscolo, M., and Dobson, C.M. (2014). Kinetic modelling indicates that fast-translating codons can coordinate cotranslational protein folding by avoiding misfolded intermediates. Nat. Commun. *5*.

Oh, E., Becker, A.H., Sandikci, A., Huber, D., Chaba, R., Gloge, F., Nichols, R.J., Typas, A., Gross, C.A., Kramer, G.*, et al.* (2011). Selective ribosome profiling reveals the cotranslational chaperone action of trigger factor *in vivo*. Cell *147*, 1295-1308.

Oswald, J., Njenga, R., Natriashvili, A., Sarmah, P., and Koch, H.G. (2021). The Dynamic SecYEG Translocon. Front. Mol. Biosci. *8*, 664241.

Pao, S.S., Paulsen, I.T., and Saier, M.H., Jr. (1998). Major facilitator superfamily. Microbiol. Mol. Biol. Rev. *62*, 1-34.

Park, E., Menetret, J.F., Gumbart, J.C., Ludtke, S.J., Li, W., Whynot, A., Rapoport, T.A., and Akey, C.W. (2014). Structure of the SecY channel during initiation of protein translocation. Nature *506*, 102-106.

Paulsen, I.T., Brown, M.H., and Skurray, R.A. (1996). Proton-dependent multidrug efflux systems. Microbiol. Rev. *60*, 575-608.

Pei, D. (2001). Peptide deformylase: a target for novel antibiotics? Expert Opin. Ther. Targets *5*, 23-40.

Peske, F., Rodnina, M.V., and Wintermeyer, W. (2005). Sequence of steps in ribosome recycling as defined by kinetic analysis. Mol. Cell *18*, 403-412.

Petrychenko, V., Peng, B.Z., de, A.P.S.A.C., Peske, F., Rodnina, M.V., and Fischer, N. (2021). Structural mechanism of GTPase-powered ribosome-tRNA movement. Nat. Commun. *12*, 5933.

Piatkov, K.I., Vu, T.T., Hwang, C.S., and Varshavsky, A. (2015). Formyl-methionine as a degradation signal at the N-termini of bacterial proteins. Microb. Cell *2*, 376-393.

Pool, M.R. (2005). Signal recognition particles in chloroplasts, bacteria, yeast and mammals (review). Mol. Membr. Biol. *22*, 3-15.

Putman, M., van Veen, H.W., and Konings, W.N. (2000). Molecular properties of bacterial multidrug transporters. Microbiol. Mol. Biol. Rev. *64*, 672-693.

Ragusa, S., Blanquet, S., and Meinnel, T. (1998). Control of peptide deformylase activity by metal cations. J. Mol. Biol. *280*, 515-523.

Ragusa, S., Mouchet, P., Lazennec, C., Dive, V., and Meinnel, T. (1999). Substrate recognition and selectivity of peptide deformylase. Similarities and differences with metzincins and thermolysin. J. Mol. Biol. *289*, 1445-1457.

Raine, A., Lovmar, M., Wikberg, J., and Ehrenberg, M. (2006). Trigger factor binding to ribosomes with nascent peptide chains of varying lengths and sequences. J. Biol. Chem. *281*, 28033-28038.

Rajagopalan, P.T., Datta, A., and Pei, D. (1997a). Purification, characterization, and inhibition of peptide deformylase from Escherichia coli. Biochemistry *36*, 13910-13918.

Rajagopalan, P.T.R., Grimme, S., and Pei, D.H. (2000). Characterization of cobalt(II)-substituted peptide deformylase: Function of the metal ion and the catalytic residue Glu-133. Biochemistry *39*, 779-790.

Rajagopalan, P.T.R., Yu, X.C., and Pei, D.H. (1997b). Peptide deformylase: A new type of mononuclear iron protein. J. Am. Chem. Soc. *119*, 12418-12419.

Randhawa, H., Chikara, S., Gehring, D., Yildirim, T., Menon, J., and Reindl, K.M. (2013). Overexpression of peptide deformylase in breast, colon, and lung cancers. BMC Cancer *13*, 321.

Ranjan, A., Mercier, E., Bhatt, A., and Wintermeyer, W. (2017). Signal recognition particle prevents N-terminal processing of bacterial membrane proteins. Nat. Commun. *8*, 15562.

Robinson, P.J., Findlay, J.E., and Woolhead, C.A. (2012). Compaction of a prokaryotic signal-anchor transmembrane domain begins within the ribosome tunnel and is stabilized by SRP during targeting. J. Mol. Biol. *423*, 600-612.

Rodnina, M.V. (2018). Translation in Prokaryotes. Cold Spring Harb. Perspect. Biol. *10*.

Rodnina, M.V., Fischer, N., Maracci, C., and Stark, H. (2017). Ribosome dynamics during decoding. Philos. Trans. R. Soc. Lond. B Biol. Sci. *372*.

Rudorf, S., and Lipowsky, R. (2015). Protein synthesis in *E. coli*: Dependence of codon-specific elongation on tRNA concentration and codon usage. PLoS One *10*, e0134994.

Rudorf, S., Thommen, M., Rodnina, M.V., and Lipowsky, R. (2014). Deducing the kinetics of protein synthesis in vivo from the transition rates measured *in vitro*. PLoS Comput. Biol. *10*, e1003909.

Sadlish, H., Pitonzo, D., Johnson, A.E., and Skach, W.R. (2005). Sequential triage of transmembrane segments by Sec61alpha during biogenesis of a native multispanning membrane protein. Nat. Struct. Mol. Biol. *12*, 870-878.

Samatova, E., Daberger, J., Liutkute, M., and Rodnina, M.V. (2020). Translational Control by Ribosome Pausing in Bacteria: How a Non-uniform Pace of Translation Affects Protein Production and Folding. Front. Microbiol. *11*, 619430.

Sandikci, A., Gloge, F., Martinez, M., Mayer, M.P., Wade, R., Bukau, B., and Kramer, G. (2013). Dynamic enzyme docking to the ribosome coordinates N-terminal processing with polypeptide folding. Nat. Struct. Mol. Biol. *20*, 843-850.

Saraogi, I., Akopian, D., and Shan, S.O. (2014). Regulation of cargo recognition, commitment, and unloading drives cotranslational protein targeting. J. Cell Biol. *205*, 693-706.

Saraogi, I., and Shan, S.O. (2014). Co-translational protein targeting to the bacterial membrane. Biochim. Biophys. Acta *1843*, 1433-1441.

Schaffitzel, C., Oswald, M., Berger, I., Ishikawa, T., Abrahams, J.P., Koerten, H.K., Koning, R.I., and Ban, N. (2006). Structure of the E. coli signal recognition particle bound to a translating ribosome. Nature *444*, 503-506.

Schibich, D., Gloge, F., Pohner, I., Bjorkholm, P., Wade, R.C., von Heijne, G., Bukau, B., and Kramer, G. (2016). Global profiling of SRP interaction with nascent polypeptides. Nature *536*, 219-223.

Schmitt, E., Guillon, J.M., Meinnel, T., Mechulam, Y., Dardel, F., and Blanquet, S. (1996). Molecular recognition governing the initiation of translation in Escherichia coli. A review. Biochimie *78*, 543-554.

Schmitt, E., Panvert, M., Blanquet, S., and Mechulam, Y. (1998). Crystal structure of methionyl-tRNAfMet transformylase complexed with the initiator formyl-methionyl-tRNAfMet. EMBO J. *17*, 6819-6826.

Senes, A., Engel, D.E., and DeGrado, W.F. (2004). Folding of helical membrane proteins: the role of polar, GxxxG-like and proline motifs. Curr. Opin. Struct. Biol. *14*, 465-479.

Serero, A., Giglione, C., Sardini, A., Martinez-Sanz, J., and Meinnel, T. (2003). An unusual peptide deformylase features in the human mitochondrial N-terminal methionine excision pathway. J. Biol. Chem. *278*, 52953-52963.

Sharma, A., Khuller, G.K., and Sharma, S. (2009). Peptide deformylase--a promising therapeutic target for tuberculosis and antibacterial drug discovery. Expert Opin. Ther. Targets *13*, 753-765.

Sheth, A., Escobar-Alvarez, S., Gardner, J., Ran, L., Heaney, M.L., and Scheinberg, D.A. (2014). Inhibition of human mitochondrial peptide deformylase causes apoptosis in c-myc-overexpressing hematopoietic cancers. Cell Death. Dis. *5*, e1152.

Sievers, A., Beringer, M., Rodnina, M.V., and Wolfenden, R. (2004). The ribosome as an entropy trap. Proc. Natl. Acad. Sci. U. S. A. *101*, 7897-7901.

Skach, W.R. (2009). Cellular mechanisms of membrane protein folding. Nat. Struct. Mol. Biol. *16*, 606-612.

Solbiati, J.O., Ciaccio, M., Farias, R.N., Gonzalez-Pastor, J.E., Moreno, F., and Salomon, R.A. (1999). Sequence analysis of the four plasmid genes required to produce the circular peptide antibiotic microcin J25. J. Bacteriol. *181*, 2659-2662.

Steinberg, R., Knupffer, L., Origi, A., Asti, R., and Koch, H.G. (2018). Co-translational protein targeting in bacteria. FEMS Microbiol. Lett. *365*.

Tastan, O., Klein-Seetharaman, J., and Meirovitch, H. (2009). The effect of loops on the structural organization of alpha-helical membrane proteins. Biophys. J. *96*, 2299-2312.

Thommen, M. (2015). Ribosome processivity and cotranslational protein folding. In Physical Biochemistry (Georg-August-Universität Göttingen).

Tobias, J.W., Shrader, T.E., Rocap, G., and Varshavsky, A. (1991). The N-end rule in bacteria. Science *254*, 1374-1377.

Tu, L., Khanna, P., and Deutsch, C. (2014). Transmembrane segments form tertiary hairpins in the folding vestibule of the ribosome. J. Mol. Biol. *426*, 185-198.

Ullers, R.S., Houben, E.N., Brunner, J., Oudega, B., Harms, N., and Luirink, J. (2006). Sequence-specific interactions of nascent Escherichia coli polypeptides with trigger factor and signal recognition particle. J. Biol. Chem. *281*, 13999-14005.

Van Aller, G.S., Nandigama, R., Petit, C.M., DeWolf, W.E., Jr., Quinn, C.J., Aubart, K.M., Zalacain, M., Christensen, S.B., Copeland, R.A., and Lai, Z. (2005). Mechanism of time-dependent inhibition of polypeptide deformylase by actinonin. Biochemistry *44*, 253-260.

Van den Berg, B., Clemons, W.M., Jr., Collinson, I., Modis, Y., Hartmann, E., Harrison, S.C., and Rapoport, T.A. (2004). X-ray structure of a protein-conducting channel. Nature *427*, 36-44.

Ventola, C.L. (2015). The antibiotic resistance crisis: part 1: causes and threats. P T *40*, 277-283.

von Heijne, G. (1989). Control of topology and mode of assembly of a polytopic membrane protein by positively charged residues. Nature *341*, 456-458.

von Heijne, G. (1992). Membrane protein structure prediction. Hydrophobicity analysis and the positive-inside rule. J. Mol. Biol. *225*, 487-494.

Walker, J.E., Carroll, J., Altman, M.C., and Fearnley, I.M. (2009). Chapter 6 Mass spectrometric characterization of the thirteen subunits of bovine respiratory complexes that are encoded in mitochondrial DNA. Methods Enzymol. *456*, 111-131.

Waudby, C.A., Dobson, C.M., and Christodoulou, J. (2019). Nature and Regulation of Protein Folding on the Ribosome. Trends Biochem. Sci. *44*, 914-926.

Wei, Y., and Pei, D. (1997). Continuous spectrophotometric assay of peptide deformylase. Anal. Biochem. *250*, 29-34.

Weiss, K., Neef, A., Van, Q., Kramer, S., Gregor, I., and Enderlein, J. (2013). Quantifying the diffusion of membrane proteins and peptides in black lipid membranes with 2-focus fluorescence correlation spectroscopy. Biophys. J. *105*, 455-462.

Wieden, H.J., Gromadski, K., Rodnin, D., and Rodnina, M.V. (2002). Mechanism of elongation factor (EF)-Ts-catalyzed nucleotide exchange in EF-Tu. Contribution of contacts at the guanine base. J. Biol. Chem. *277*, 6032-6036.

Woolhead, C.A., McCormick, P.J., and Johnson, A.E. (2004). Nascent membrane and secretory proteins differ in FRET-detected folding far inside the ribosome and in their exposure to ribosomal proteins. Cell *116*, 725-736.

Wu, P., and Brand, L. (1994). Resonance energy transfer: methods and applications. Anal. Biochem. *218*, 1-13.

Xiao, C., and Zhang, Y. (2007). Catalytic mechanism and metal specificity of bacterial peptide deformylase: a density functional theory QM/MM study. J. Phys. Chem. B *111*, 6229-6235.

Xiao, Q., Zhang, F., Nacev, B.A., Liu, J.O., and Pei, D. (2010). Protein N-terminal processing: substrate specificity of Escherichia coli and human methionine aminopeptidases. Biochemistry *49*, 5588-5599.

Yang, C.I., Hsieh, H.H., and Shan, S.O. (2019). Timing and specificity of cotranslational nascent protein modification in bacteria. Proc. Natl. Acad. Sci. USA *116*, 23050-23060.

Yin, Y., He, X., Szewczyk, P., Nguyen, T., and Chang, G. (2006). Structure of the multidrug transporter EmrD from Escherichia coli. Science *312*, 741-744.

Yoon, H.J., Kim, H.L., Lee, S.K., Kim, H.W., Kim, H.W., Lee, J.Y., Mikami, B., and Suh, S.W. (2004). Crystal structure of peptide deformylase from Staphylococcus aureus in complex with actinonin, a naturally occurring antibacterial agent. Proteins *57*, 639-642.

Youngman, E.M., McDonald, M.E., and Green, R. (2008). Peptide release on the ribosome: mechanism and implications for translational control. Annu. Rev. Microbiol. *62*, 353-373.

Zaghouani, M., Bögeholz, L.A.K., Mercier, E., Wintermeyer, W., and Roche, S.P. (2019). Total synthesis of (+/-)-fumimycin and analogues for biological evaluation as peptide deformylase inhibitors. Tetrahedron *75*, 3216-3230.

Zhang, G., Hubalewska, M., and Ignatova, Z. (2009). Transient ribosomal attenuation coordinates protein synthesis and co-translational folding. Nat. Struct. Mol. Biol. *16*, 274-280.

Zhang, X., Rashid, R., Wang, K., and Shan, S.O. (2010). Sequential checkpoints govern substrate selection during cotranslational protein targeting. Science *328*, 757-760.

Zhou, F.X., Merianos, H.J., Brunger, A.T., and Engelman, D.M. (2001). Polar residues drive association of polyleucine transmembrane helices. Proc. Natl. Acad. Sci. U. S. A. *98*, 2250-2255.

Zimmer, J., Nam, Y., and Rapoport, T.A. (2008). Structure of a complex of the ATPase SecA and the protein-translocation channel. Nature *455*, 936-943.

6 Appendix

6.1 List of figures

6.2 List of tables

Acknowledgements

I would like to thank Marina Rodnina for giving me the opportunity to work on this exciting topic for my PhD thesis and for all the support, motivation and inspiration during the last years. I would also like to thank the members of my thesis advisory committee Kai Tittmann, Alexander Stein and Blanche Schwappach for their helpful suggestions and challenging questions which helped to improve my studies. Furthermore, I thank Wolfgang Wintermeyer, Alex Faesen and Hauke Hillen for joining my examination board and the GGNB office for clarifying all organizational questions.

Thanks a lot to Wolfgang Wintermeyer and Evan Mercier who welcomed me to the lab as a rotation student and did a great job in supervision so that I was excited to continue for my PhD. I am very thankful for your support that you were always available to discuss science, answer questions and help me to navigate arising problems. Special thanks go out to Evan for being an awesome daily supervisor, lunch partner and lab colleague and for at least tasting all the cakes and baked goods that I prepared over time.

Most of my experiments would not have been possible without technical support and nanodiscs from Anna and Franzi, ribosomes from Sandra, tRNA from Olaf and many other things prepared and maintained by Michael, Tessa, Nessa, Manuela, Theo, Tanja and Puyan. Many thanks go to Dimitra for keeping a great overview and help with all kinds of organizational issues and to Mario for the computer support.

I would like to thank my downstairs lab mates Jan and Xiaolin for all the non-smoking smoker breaks, sharing even the smallest piece of bubble wrap and tasting chocolates and cookies together. Thanks Anna for the great time I had sitting next to you and for coordinating schedules during the fun times of the Covid-19 pandemic. Lunch time would have been boring without our group and important discussions about movies, zucchinis and burgers. Evan, Xiaolin, Olaf, Justas, Shreya, Nicola, Michael, Franzi and Sandra, thanks for sharing your culture with me. Thanks to the rest of the lab who were always helpful and fun to chat with: Moritz (we should have a board game evening again), Sung-Hui (best dinners), Betty (beware of Pfefferminz-Lindor), Vitalii, Natalie, Panos, Kärt, Prajwal, Mani, Sakshi, Frank, Katya, Ingo, Nilanjan, Vaishali, Céline, Natalia and Carolina.

I want to thank all my friends outside the lab that made my time in Göttingen so awesome: Franco for gorda times, bike trips, holidays and many board game evenings. Kristin for long-distance support and being the best travel buddy. Linda, Sarah, Sarah and Ronja for keeping me sane during lockdown with Online-escape rooms and snow hikes and for very successful pandemic games. Alex for being a great motivator during volleyball and bouldering. Carolina and Ruben for fun nights and training my Spanish. Sabrina, Georg, Karl and Uwe for fun Doppelkopf evenings at Gartenlaube. Thomas for the French lunches. Steffen for introducing me into the Göttingen student life. Everyone at volleyball and happy hour. And last but not least, my family for all their support.